

AN ABSTRACT OF THE THESIS OF

ELHAM ASLANI for the degree of

Master of Science in

Chemical Engineering presented

on December 7, 2005.

Title: Geometric and Wall Pressure Characterization of Patient Abdominal Aortic Aneurysm.

Abstract approved:

Redacted for Privacy

Robert A. Peattie

In this study, we have characterized a series of patient Abdominal Aortic Aneurysms (AAAs) based on their geometric parameters, wall pressure distributions and ages. Abdominal aortic aneurysms (AAAs) are localized aortic dilations that have been estimated to occur in 5 to 7 percent of the U.S. population over age 60. At present, surgical repair is recommended when lesion maximum diameter exceeds 5 cm, regardless of other geometric properties. However, in addition to maximum diameter, many other geometric features, including length, curvature, tortuosity, thrombus distribution and lumenal index can also affect wall stress and thereby alter rupture risk.

To evaluate these features, computational models of a series of 35 actual patient AAAs were constructed and analyzed from abdominal CT series, using specific software (*MIMICS*, Materialise Inc.; *CFD-GEOM*, CFD Research Corp.; *AutoCAD*, Autodesk Inc.) to read and segment the CT scans. AAA geometric

parameters were then directly measured from the models. In addition to flow rate, wall pressure is strongly affected by aneurysm geometry. Since wall pressure is the physical source of wall stress, pressure distributions were evaluated in a set of patient-based, flow-through AAA phantoms at a series of steady flow rates producing Reynolds numbers of 500 to 3000. Although in general wall pressure was nearly constant or declined slightly along the length of the bulge, cases were observed in which the pressure rose by 10-15% at the bulge exit.

Maximum bulge diameter was found to vary from 4 to 7 cm, with a mean of 5.66 cm. 83 percent of the patients presented measurable thrombus, with a mean thrombus volume of 61.07 cm^3 . AAAs with measurable thrombi presented larger bulge diameters ($p = 0.022$) but smaller lumen diameters ($p = 0.042$) and horizontal curvatures ($p = 0.008$) than patients without thrombus. In addition, thrombosed patients were found to have bulge shapes more nearly similar to their corresponding spheres than cylinders ($p < 0.0001$). Geometric parameters were also evaluated and compared between different age groups. Maximum outer diameter, vertical curvature and thrombus volume is dependent on the age of the AAA patients. In this study, patients with age over 80 had substantially larger $V_{\text{thrombus}} / V_{\text{AAA}}$ ratio than patients with age between 65 to 70 years old ($p = 0.02$). The correlation between geometric parameters and their effect on wall pressure distribution are also discussed.

© Copyright by Elham Aslani
December 7, 2005
All Rights Reserved

Geometric and Wall Pressure Characterization of Patient Abdominal
Aortic Aneurysm

by
Elham Aslani

A THESIS

submitted to

Oregon State University

in partial fulfillment of
the requirements for the
degree of

Master of Science

Presented December 7, 2005
Commencement June 2006

Master of Science thesis of Elham Aslani
presented on December 7, 2005.

APPROVED:

Redacted for Privacy

Major Professor, representing Chemical Engineering

Redacted for Privacy

Head of the Department of Chemical Engineering

Redacted for Privacy


Dean of the Graduate School

I understand that my thesis will become part of the permanent collection of Oregon State University libraries. My signature below authorizes release of my thesis to any reader upon request.

Redacted for Privacy

Elham Aslani, Author

ACKNOWLEDGMENTS

I would like to thank many individuals who made this project possible: Sincere appreciation to my advisor, Dr. Robert Peattie, who gave me the opportunity to participate in this exciting work and supported me every step of the way through this project.

Thanks to Dr. Joseph McGuire, my additional review committee member for his time and willingness to listen. Dr. Michael M. Schimerlik for reviewing my thesis and offering me words of encouragement. Dr. Michael J. Hallisey and Anne Lundgren were diligent in producing CT scans from the presenting patient population of Hartford Hospital (Hartford, CT). Materialise Inc. for their support of this project.

I wish also to thank all the reviewers of this thesis for their comments. Special thanks to Azam Afzali, my mother, for helping me through countless tedious hours data entering.

Finally, I wish to thank all the professors and staffs in the Chemical Engineering department for a enjoyable two years at Oregon State University.

TABLE OF CONTENTS

	<u>Page</u>
1. Introduction.....	1
1.1 Problem Statement.....	1
1.2 Basis for Work.....	1
1.3 Summary of Previous Research.....	2
1.4 Scope.....	3
2. Background.....	4
2.1 Clinical Review.....	4
2.1.1 Burden of Suffering.....	6
2.1.2 Structure and Function of Normal Aorta.....	7
2.1.3 Classification and Definition of Aneurysms.....	12
2.1.4 Thrombosis and Its Formation Risk Factors.....	17
2.1.5 Age, Gender, Race and Etiology of Aneurysms.....	18
2.1.6 Clinical Treatment of Aneurysms.....	21
2.1.7 Previous Clinical Studies.....	24
2.2 Biomechanics.....	26
2.2.1 Experimental Simplifications and Assumptions.....	26
2.2.2 Dynamic Similarity.....	28
2.2.3 Previous Engineering Studies.....	29
2.2.4 Specific Goals of This Study	32
3. Methods.....	34
3.1 Geometric Parameters Measurement.....	34
3.1.1 Description of Abdominal CT scans.....	34
3.1.2 Importing CT scans into MIMICS Software.....	34
3.1.3 Region Growing and Mask development.....	37
3.1.4 Smoothing factors.....	38
3.1.5 Creating 3D Models of AAAs.....	41
3.1.6 Geometric Parameters Measured by MIMICS.....	44
3.1.7 Geometric Parameters Measured by CFD-Geom.....	48
3.1.8 Curvature Measurement by AutoCAD.....	51
3.1.9 Statistical Analysis.....	53
3.2 Pressure Measurement.....	54

TABLE OF CONTENTS (Continued)

	<u>Page</u>
3.2.1 Flow Loop Configuration.....	54
3.2.2 Transducer Calibration.....	56
3.2.3 Flow rate Measurement and Reynolds Number.....	56
 4. Results.....	 58
4.1 Geometric Parameters	58
4.1.1 AAA Geometric Parameters	58
4.1.2 Bulge Surface Similarity.....	67
4.1.3 Age and AAA Geometric Parameters.....	72
4.2 Pressure Measurement.....	78
4.2.1 Calibration Curves.....	78
4.2.2 Pressure Distribution Measurements.....	81
 5. Discussion.....	 85
5.1 Geometric Parameters.....	85
5.1.1 AAA Geometric Parameters Analysis Based on Thrombus Existence.....	 85
5.1.2 AAA Geometric Parameters Analysis.....	90
5.1.3 Bulge Surface Similarity Evaluation.....	103
5.2 Age Specific Analysis.....	110
5.2.1 Age and Geometric Parameters.....	110
5.2.2 Group Age Analysis.....	113
5.3 Pressure Measurements.....	117
5.3.1 Pressure Distributions.....	117
5.3.2 Pressure and Geometric Parameters.....	120
5.4 Comparison with Previous Studies.....	121
5.5 Clinical Significance.....	123

TABLE OF CONTENTS (Continued)

	<u>Page</u>
6. Conclusion.....	124
6.1 Summary of Most Important Findings.....	124
6.2 Future Directions.....	126
Bibliography.....	127
Appendices.....	132

LIST OF FIGURES

<u>Figure</u>	<u>Page</u>
Figure 2.1 The healthy thoracic aorta, heart and other great vessels.....	5
Figure 2.2 Schematic drawing of the aortic diameter during a life time.....	5
Figure 2.3 Prevalence of abdominal aortic aneurysm over time.....	7
Figure 2.4 Diagram of a muscular artery.....	9
Figure 2.5 Cross section of small arteries.....	10
Figure 2.6 Transverse section showing part of a large elastic artery.....	10
Figure 2.7 Pathologic types of aortic aneurysms.....	13
Figure 2.8 Diagram depicting the usual mechanism that causes a dissecting aneurysm.....	13
Figure 2.9 Aorta in a 66-year-old man with both saccular and fusiform aneurysms.....	16
Figure 2.10 Gross appearance of a saccular aneurysm of the infrarenal abdominal aorta.....	17
Figure 2.11 the frequency in men increases rapidly at age greater than 55, reaches a peak prevalence of 5.9% at 80 to 85 years, and then decreases....	19
Figure 2.12 Transfemoral intraluminal graft implantation for abdominal aortic aneurysm.....	22
Figure 2.13 Transfemoral intraluminal graft implantation for abdominal aortic aneurysm: Step in the deployment of proximal and distal stents	23
Figure 3.1 The Import Project Wizard.....	35
Figure 3.2. The Change Orientation window.....	36
Fig 3.3 Patient CT image as displayed in MIMICS.....	37
Fig 3.4 Patient CT image after applying growing region function.....	38

LIST OF FIGURES (Continued)

<u>Figure</u>	<u>Page</u>
Figure 3.5 The Smoothing process.....	40
Figure 3.6 3D Generation Parameters of the smoothest model which was constructed from AAA of patient 1.....	40
Figure 3.7 Top and Bottom slices representation of bulge for patient 5.....	41
Figure 3.8 3-D reconstruction of one representative aneurysm with thrombus	43
Figure 3.9 Maximum bulge diameter of model 28 was measured using point-to-point measurement tool.....	44
Figure 3.10 Lumenal Index calculation.....	46
Figure 3.11 The bulge similarity.....	47
Figure 3.12 Polyline representation of the 3D model.....	48
Figure 3.13 Tortuosity calculations through CFD-GEOM.....	49
Figure 3.14 (a) A New reconstructed three slices mask. (b) The Auto-CAD representation of AAA. The bulge slices could not be realized individually..	52
Figure 3.15 For each AAA, the vertical curvature was evaluated in 5 planes rotated through 7.5 degrees around the y-axis.....	53
Figure 3.16 Location of the pressure taps within an aneurysm phantom.....	54
Figure 3.17 Flow loop used to deliver steady flow through the phantoms....	55
Figure 4.1 3-D representatives of models 1, 2, 3 and 4 AAA patients.....	59
Figure 4.2 Model 1, 2, 3 and 4 of AAA patients in their polyline (.igs) Formats.....	60
Figure 4.3 Transverse cross- section of models 1 to 12 at their maximum diameter levels.....	61
Figure 4.4 The Calibration curve of transducer 1 of the model 7.....	79

LIST OF FIGURES (Continued)

<u>Figure</u>	<u>Page</u>
Figure 4.5 The Calibration curve of transducer 1 of the model 8.....	80
Figure 4.6 The Calibration curve of transducer 1 of the model 11.....	81
Figure 4.7 Pressure plots of P_1 , P_3 and P_5 of model 7 for all Reynolds numbers were shown.....	82
Figure 4.8 Pressure plots of P_1 , P_3 and P_5 of model 8 for all Reynolds numbers were shown.....	83
Figure 4.9 Pressure plots of P_1 , P_3 and P_5 of model 11 for all Reynolds numbers were shown.....	84
Figure 5.1 Six of 35 AAA models without measurable thrombus.....	85
Figure 5.2 Maximal luminal diameter of the AAAs for 35 patients.....	87
Figure 5.3 Maximal outer diameter of the AAAs for 35 patients.....	88
Figure 5.4 Horizontal curvature, of the 35 AAA patients.....	89
Figure 5.5 Plot of AAA volume versus diameter, along with the best-fit line computed by least squares regression.....	91
Figure 5.6 Bulge volume versus tortuosity was plotted along with the best-fit line computed by least squares regression.....	92
Figure 5.7 Plot of the bulge volume versus length along with the best-fit line computed by least squares regression.....	93
Figure 5.8 Plot of the bulge volume versus vertical curvature along with the best-fit line computed by least squares regression.....	94
Figure 5.9 Plot of the bulge volume versus diameter ratio (D/d) along with the best-fit line computed by least squares regression was shown.....	95
Figure 5.10 A scatter graph of tortuosity versus diameter along with the best-fit line was computed and plotted by least squares regression.....	96

LIST OF FIGURES (Continued)

<u>Figure</u>	<u>Page</u>
Figure 5.11 A scatter plot of the horizontal curvature versus tortuosity along with the best-fit line.....	97
Figure 5.12 Vertical curvature versus angular deviation was plotted along with the best-fit line computed by least squares regression.....	98
Figure 5.13 Luminal index versus D/d was plotted along with the best-fit line computed by least squares regression for 28 patients with measurable thrombus.....	99
Figure 5.14 Plot of the volume ratio versus luminal index	100
Figure 5.15 Plot of the thrombus volume versus angular deviation.....	101
Figure 5.16 The best-fit line which was computed through least squares regression was displayed for scatter plot of thrombus volume versus D/d....	102
Figure 5.17 A scatter plot of thrombus volume versus non-dilated diameter of the lumen was shown along with the best-fit line computed by least squares regression.....	103
Figure 5.18 It concluded that bulge shape of patients with thrombus is significantly more similar to a sphere than cylinder ($p < 0.0001$).....	105
Figure 5.19 A plot of bulge surface area versus tortuosity. These two parameters are not functionally dependent ($r = 0.001 < 0.1$).....	106
Figure 5.20 A plot of bulge surface area versus D/d. These two parameters are functionally dependent ($r = 0.368 > 0.1$).....	107
Figure 5.21 There is a significant dependency between bulge surface area and thrombus volume.....	108
Figure 5.22 The high regression value of this scatter plot shows a functional dependency between S_b/S_c and thrombus volume.....	109

LIST OF FIGURES (Continued)

<u>Figure</u>	<u>Page</u>
Figure 5.23 The low regression value of this plot shows no significant correlation between thrombus volume and S_b/S_s	109
Figure 5.24 A scatter plot of diameter versus age of 28 patients (23 thrombosed patients, 5 non-thrombosed patients) were shown.....	110
Figure 5.25 Plot of tortuosity versus age.....	111
Figure 5.26 Vertical curvature versus age plot was displayed in this figure...	112
Figure 5.27 Correlation between thrombus volume and age for 23 patients was plotted as a scatter graph along with the best-fit line computed by least squares regression.....	113
Figure 5.28 Maximal diameter evaluation.....	115
Figure 5.29 Bulge Length.....	115
Figure 5.30 Ratio of thrombus volume to AAA volume.....	116
Figure 5.31 Luminal index group 1 is significantly different from group 4...	116
Figure 5.32 Tortuosity: between all group ages.....	117
Figure 5.33 As one example of the mechanical information provided by these measurements, the pressure distribution in each model at $Re = 500$ was presented.....	118
Figure 5.34 Computational models of three flow-through phantoms.....	121

LIST OF TABLES

<u>Table</u>	<u>Page</u>
Table 2.1 Growth rate of Abdominal Aortic Aneurysms.....	25
Table 3.1 Definition of Top and Bottom slices based on their coordinates and diameters.....	42
Table 3.2 Diameter evaluation of Model 28.....	45
Table 4.1 Measured surface areas of lumen and bulge (lumen+ thrombus) of each AAA patient at its maximum bulge diameter level.....	62
Table 4.2 AAA Geometric Parameters of 35 patient-based models.....	65
Table 4.3 The bulge similarity table.....	68
Table 4.4 Age group 1: this group contains 9 of 28 AAA patients.....	73
Table 4.5 Age group 2: this group contains 5 of 28 AAA patients.....	74
Table 4.6 Age group 4: this group contains 6 of 28 AAA patients.....	76
Table 4.7 Age group 4: this group contains 8 of 28 AAA patients.....	77
Table 4.8 Calibration table of model 7.....	78
Table 4.9 Calibration table of model 8.....	79
Table 4.10 Calibration table of model 11.....	80
Table 4.11 Correction factors of model 7.....	82
Table 4.12 Absolute wall pressure distributions, in mmHg of, model 7, corrected for transducer height.....	82
Table 4.13 Correction factors of model 8.....	83
Table 4.14 Absolute wall pressure distributions, in mmHg of, model 8, corrected for transducer height.....	83
Table 4.15 Correction factors of model 11.....	84

LIST OF TABLES (Continued)

<u>Table</u>	<u>Page</u>
Table 4.16 Absolute wall pressure distributions, in mmHg of, model 11, corrected for transducer height.....	84
Table 5.1 Mean and standard deviation of AAA geometric parameters for patients without measurable thrombus (N= 6).....	86
Table 5.2 Mean and standard deviation of AAA geometric parameters for patients with measurable thrombus (N= 29).....	86
Table 5.3 To find the significant differences between patients with measurable thrombi and those without, p-values for each geometric parameter was calculated using ANOVA test.....	87
Table 5.4 Bulge surface similarities were also analyzed based on measurable thrombus deposits (29 thrombosed patients, 6 non-thrombosed patients)....	104
Table 5.5 Pressure differences for three phantoms (models 8, 11 and 7) at various Reynolds numbers.....	118

LIST OF APPENDICES

<u>APPENDIX</u>	<u>Page</u>
APPENDIX A: 3D REPRESENTATION OF 35 AAA PATIENTS.....	132
APPENDIX B: POLYLINE AND CENTERPOINT PATH OF 35 AAA PATIENTS.....	137
APPENDIX C: AXIAL CROSS-SECTIONS OF AAA BULGES AT THEIR MAXIMUM DIAMETER LEVELS.....	142
APPENDIX D: CALIBRATION PLOTS.....	145
APPENDIX E: TABLES OF INITIAL PRESSURES	152
APPENDIX F: PLOTS STEADY FLOW ABSOLUTE PRESSURES.....	155

CHAPTER 1: INTRODUCTION

1.1 PROBLEM STATEMENT

In this study a series of 35 patient aneurysms have been characterized based on their geometric parameters, wall pressure distributions and ages.

To evaluate geometric parameters, computational models of a series of real patient AAAs were constructed from abdominal CT series using specific software (*MIMICS*, Materialise Inc). Maximum bulge diameter, lesion diameter, length, volume, thrombus volume if present, AAA horizontal and vertical curvatures and tortuosity were measured and compared.

As one example of the information that can be obtained once satisfactory AAA computational images have been created, three models that had been previously cast into flow-through phantoms were used for measuring wall pressure distribution. These phantoms were incorporated into an existing flow loop simulating steady aortic conditions with a Reynolds number in the range of 500 to 3000, and wall pressure was evaluated quantitatively in them.

1.2 BASIS FOR WORK

Based on biomechanical concepts, aneurysm rupture may be thought of as a material failure. Therefore biomechanical analysis of rupture risk should be based on consideration of the state of stress within the lesion wall. Such internal stresses develop in the wall as a result of blood flow through the vessel, since flowing blood exerts both normal and shear forces on the wall inner surface and these forces are transmitted into the wall interior. Therefore, the magnitude and distribution of wall stresses are determined in part by luminal flow properties, as well as by bulge shape and diameter and wall material properties. In the current

project, as part of a study of AAA wall stress development, geometric features and wall pressure distribution have been quantitatively evaluated in a series of models derived directly from CT imaging of aneurysmal patients. The goal of this research is to develop biomechanically accurate criteria for AAA rupture risk assessment. This information will provide physicians with a quantitatively valid basis for determining the need for invasive surgical treatment of specific AAAs.

1.3 SUMMARY OF PREVIOUS RESEARCH

Since the work of Szilagyi *et al* 40 years ago, maximum AAA diameter has been the most commonly used factor to predict the risk of rupture [1]. In general, patients with AAA transverse diameters (Tr) or anteroposterior diameter (AP) ≥ 5.0 cm in women and 5.5 cm in men should undergo surgical repair. However, aneurysms ≤ 5 cm in maximal diameter cover 10% to 24% of ruptured aneurysms in some series [2-4]. Other indices of rupture risk have been investigated in an effort to improve on the limitations of the diameter of AAA as the only factor in assessing the risk of rupture. Since aneurysm rupture occurs when local wall stress exceeds the tensile strength of the aortic wall at a particular site, many investigators have focused on the role of peak aortic wall stress in relationship to rupture risk of AAA. Filinger *et al* concluded that peak aortic wall stress was superior to diameter in predicting rupture of AAA [5, 6].

Finite element analysis, a mathematical technique for determination of wall stress, was initially applied to two-dimensional models of AAAs. This method has undergone significant evolution to include theoretic three-dimensional shapes and, more recently, to the actual AAA shape obtained from CT images [5, 6, 7-11].

Finally, several groups have attempted to evaluate AAA wall internal stress magnitude and its dependence on bulge shape and diameter [9, 12, 13]. Although

these analyses represent an important first step towards a qualified depiction of the wall stress state, for initial purposes they simplified boundary conditions at the fluid-wall interface, neglecting shear effects and assuming pressure to be a single constant. However, flow patterns within the AAA can strongly influence the magnitude and distribution of all components of the flow-induced forces on the bulge wall, necessitating the use of more complex boundary conditions for accurate stress analysis.

1.4 SCOPE

The present study is focused on evaluating geometric parameters and wall pressure distributions in three-dimensional models. The geometric parameters describe the bulge geometric characteristics. The wall pressure distribution is limited to steady flow in rigid phantoms. However, all the measurements are based on a series of three dimensional models of real patient AAAs providing a comprehensive array of sizes that match *in vivo* aneurysms. Results are shown for Reynolds numbers (based on inlet tube diameter and average flow rate) which range from $Re = 500$ to 3000 , closely matching the range of typical *in vivo* Reynolds numbers. The following information is presented for all 35 models: 1) 3-D reconstruction of the aneurysms with thrombus when present 2) Measured geometric parameters of each AAA. The following information is presented only for three models at $Re = 500$ to 3000 : 1) Plot of pressure versus Reynolds number 2) Plot of pressure versus transducers positions.

CHAPTER 2: BACKGROUND

2.1 CLINICAL REVIEW

Aortic aneurysms (from the Greek *aneurysma*, meaning “dilation”) have been recognized since antiquity, the French physician Fernel described in 1554 an aneurysm as a dilatation of an artery full of spiritous blood [14, 15].

In terms of the original definition, an aneurysm is an irreversible, local, progressive dilation of an artery to at least 1.5 times its normal diameter. The normal abdominal aorta (infrarenal) has a diameter of about $2.0 \text{ cm} \pm 0.51 \text{ cm}$ [16]. It is generally smaller in younger persons and in women. An abdominal aorta that exceeds at least 3.0 cm by computed tomography (CT) or ultrasonography (U/S) can be considered an aneurysm, but AAAs have been noted to be as large as 10.0 to 15.0 cm [17].

The aorta has different portions which could be the sites of aneurysms. The thoracic portion of the aorta is a continuation of the aortic arch as it descends through the thoracic cavity to the diaphragm. The abdominal portion of the aorta is the segment of the aorta between the diaphragm and the level of the fourth lumbar vertebra, where it divides into right and left common iliac arteries [18] (Fig 2.1). Early in this century, the thoracic aorta was thought to be the site of aneurysmal dilatations ten times more often than the abdominal segment. Understanding of this ratio remained unchanged some 30 years later, but was revised to three to one shortly thereafter. The ratio was reversed in the following decade and since 1949 twice as many aneurysms have been found in the abdominal as in the thoracic aorta [14].

Before the occurrence of a disease is analyzed, diagnostic criteria must be established. This is usually not difficult in a clinical situations dealing with fairly large aneurysms; however, a problem arises in studies where the prevalence is unknown. This is true for aneurysms detected both at autopsy and with ultrasonography or computed tomography. One problem is to decide when a normal aorta becomes aneurysmal (Fig. 2.2) [26].

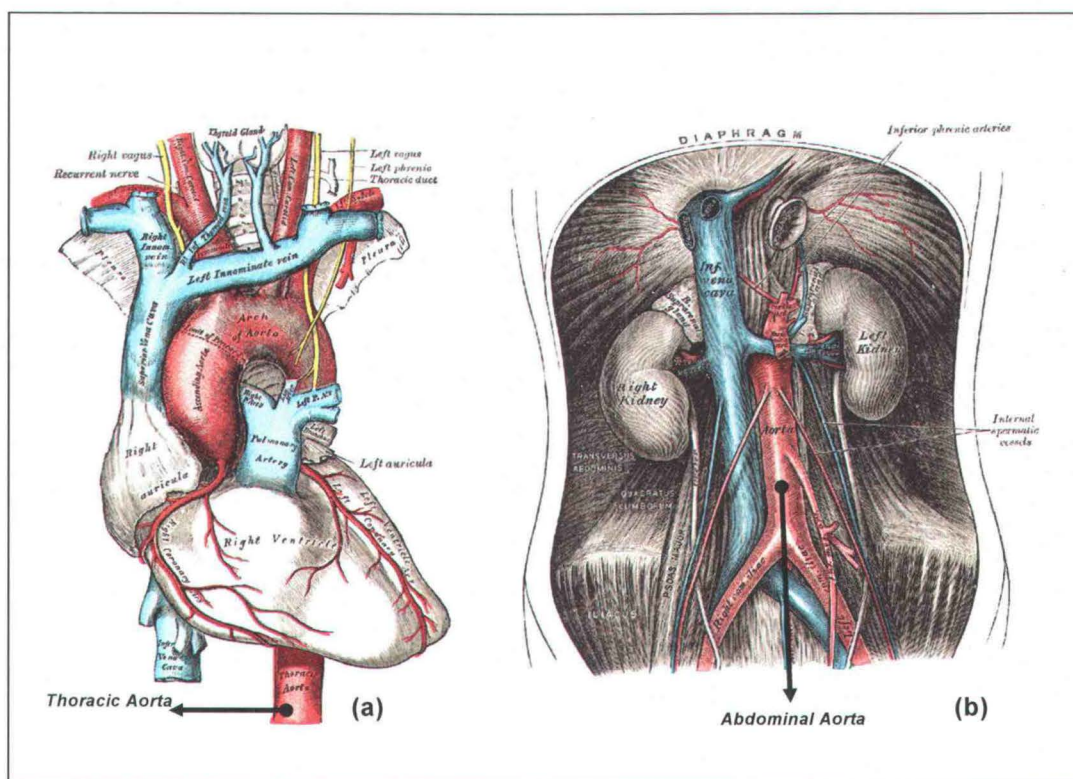


Figure 2.1 (a) The healthy thoracic aorta, heart and other great vessels. The thoracic portion of the aorta is a continuation of the aortic arch as it descends through the thoracic cavity to the diaphragm. (b) The healthy abdominal aorta and its branches (red). It is the segment of the aorta between the diaphragm and the level of the fourth lumbar vertebra, where it divides into right and left common iliac arteries. (Modified from Gray's anatomy, 1918)

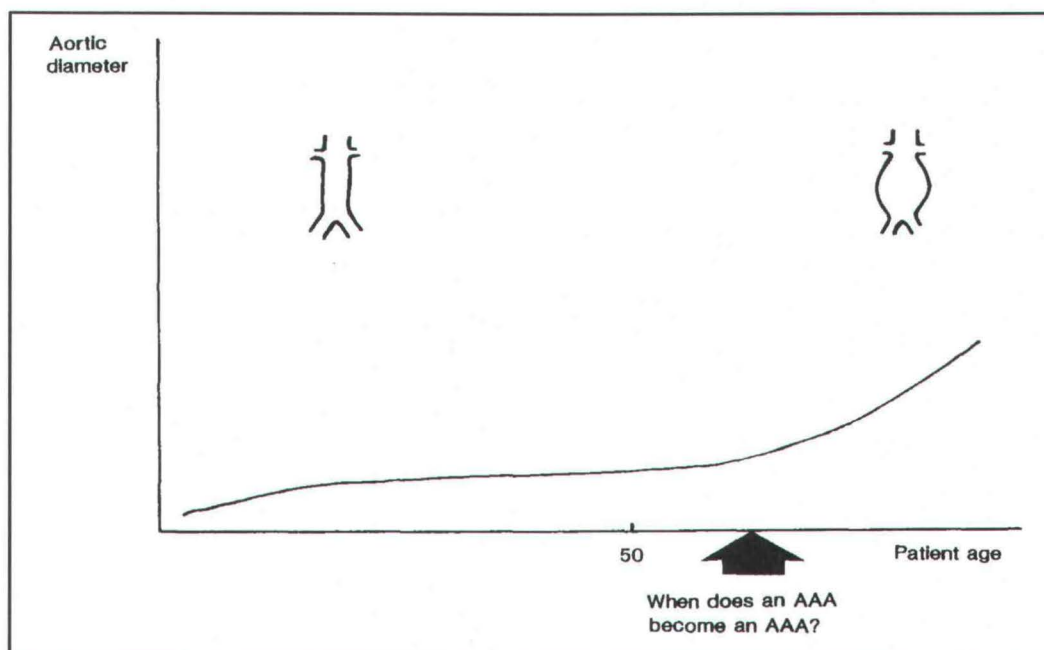


Figure 2.2 Schematic drawing of the aortic diameter during a life time. One problem is to decide when a normal aorta becomes aneurysmal. (Reprinted from Yao, 1994)

Aneurysm may cause complications by impinging upon and even eroding nearby blood vessels, organs, or bones; however, the major complication associated with aneurysms is a focal loss of elastic tissue in the aneurysmal aorta that decreases the aorta's ability to withstand expansile forces and rupture. The natural history of untreated AAAs comes from two studies, one shortly before the first AAA repair in the early of 1950s, and one about a decade later [19]. The main finding was that the 5-year survival of untreated AAA is about 20%-30%, compared to an expected 80% 5-year survival of an age-adjusted group without AAA [15].

2.1.1 Burden of Suffering

In a study of Bergqvist [26] found abdominal aortic aneurysms in 983 men and 485 women, which gives prevalences of 4.3% among men and 2.1% among women. Thirty-five men and two women had previously been operated on electively. The AAA had ruptured in 136 men and 51 women (14% of all aneurysms). The frequency was age and sex standardized based on the number of autopsies in the year 1970. The annual age-standardized sex-specific rate for the period is shown in Figure 2.3.

The prevalence increase among men per year was 4.7% (95% confidence interval 3.6-5.9) and that among women, 3.0% (1.8-4.3). Among men, all age groups greater than 60 years contributed to the increase over the years, whereas among women the increase was seen mainly between 70 and 80 years of age.

According to the report of the U.S. preventive services task force [20], approximately 8,700 deaths from AAA were reported in the U.S. in 1990, but undiagnosed ruptured aneurysms are probably responsible for many other cases of sudden death in older people. Once rupture occurs, massive intraabdominal bleeding is usually fatal unless prompt surgery can be performed [20]. A review of six case-series including 703 cases of ruptured aneurysm estimated that only 18% of all patients with ruptured AAA reached a hospital and survived surgery. The large majority of deaths from AAA occur in older men and women; men over 60

and women over 70 accounted for 95% of all deaths from AAA in a recent report [20]. Approximately 0.8% of male deaths and 0.3% of female deaths among persons over 65 years of age in the U.S. were attributed to AAA in 1990 [20].

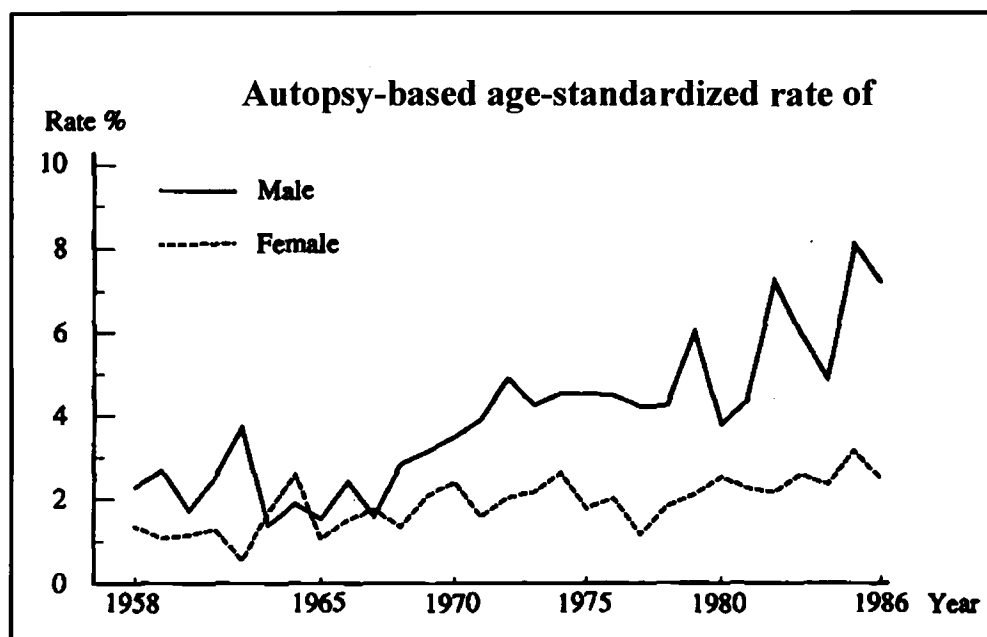


Figure 2.3 Prevalence of abdominal aortic aneurysm over time. Autopsy based age-standardized and sex-specific rates are shown: Among both men and women there was a significant increase over time. The annual increase among men was 4.7% (95% confidence interval 3.6-5.9) and that among women, 3.0% (1.8-4.3). Among men, all age groups greater than 60 years contributed to the increase over the years, whereas among women the increase was seen mainly between 70 and 80 years of age. (Reprinted from Yao, 1994)

2.1.2 Structure and Function of Normal Aorta

The aorta is the largest artery in the human body. It originates from the left ventricle of the heart and brings oxygenated blood to all parts of the body in the systemic circulation. It is the principal of a category of vessels known as large elastic arteries, which are characterized by relatively thin walls for their size containing an abundance of elastic tissue.

Arterial structure and function are closely linked and interdependent. They are organs designed to propel and distribute actively the blood from the heart to various tissues. Interestingly, they work continuously, being exposed always to high blood pressure and high oxygen tension. The energy required for their work is

derived from mural components of the arteries themselves. This fine synchronization has disadvantages, however, as the structural “reserve zone” between the needs for physiological demands and additional requirements is very narrow. The relation of tissue architecture to function is particularly evident in the structural similarities between arteries of comparable size and workload. Arteries change their structure throughout the prenatal and postnatal period. They grow in length and diameter throughout infancy and adolescence, acquiring their mature features in early adult life. The growth involves a constant process of remodeling and an increase in thickness, particularly in the inner wall (intima). The arterial growth in length may be explained readily as an adjustment required by the increasing length of the body. The increase in thickness and remodeling of the inner wall itself, however, is not entirely understood and remains somewhat controversial. Usually, three types of arteries are distinguished: (1) large or elastic, (2) medium size or muscular, and (3) small arteries and arterioles. The aorta is the principal vessel in the elastic arteries category. These arteries provide a relatively constant flow of blood in the arterial system by maintaining the pressure during diastole and supplying tension opposing the expansile force of the blood pressure during systole. They are so structured that these tensile forces are distributed evenly over the wall and are balanced by structural adaptations [14].

The basic structure of an arterial wall consists of three distinct layers (Fig. 2.4, 2.5, 2.6): 1) The *tunica intima* shows one layer of endothelial cells supported by a subendothelial layer of loose connective tissue containing occasional smooth muscle cells. In arteries, the intima is separated from the media by an *internal elastic lamina*, the most external component of the intima (Fig. 2.4 and 2.5). This lamina, composed of elastin, has gaps (fenestrae) that allow the diffusion of substances to nourish cells deep in the vessel wall. As a result of the absence of blood pressure and the contraction of the vessel at death, the tunica intima of the arteries generally has an undulated appearance in tissue sections. 2) The *tunica media* consists chiefly of concentric layers of helically arranged smooth muscle cells (Fig 2.4). Interposed among the smooth muscle cells are variable amounts of elastic fibers and lamellae, reticular fibers (collagen type III), proteoglycans, and

glycoproteins. Smooth muscle cells are the cellular source of this extracellular matrix. In arteries, the media has a thinner *external elastica lamina*, which separates it from the tunica adventitia. 3) The *tunica adventitia* consists principally of collagen type I and elastic fibers. The adventitial layer gradually becomes continuous with the connective tissue of the organ through which the vessel runs [21]. These tunics are poorly distinguished at birth and in early life but become more accentuated and diverse with growth and advancing age, particularly those concerning the intima [14]. Figure 2.4 is a histologic section of a human aortic wall (elastic wall) and muscular artery, in which the three concentric tunics are clearly visible. While this pattern is seen in all arteries ranging from the aorta down to the smallest arterioles, there are important variations in the amounts and types of cells and collagen, and the amount of elastin found in the various layers.

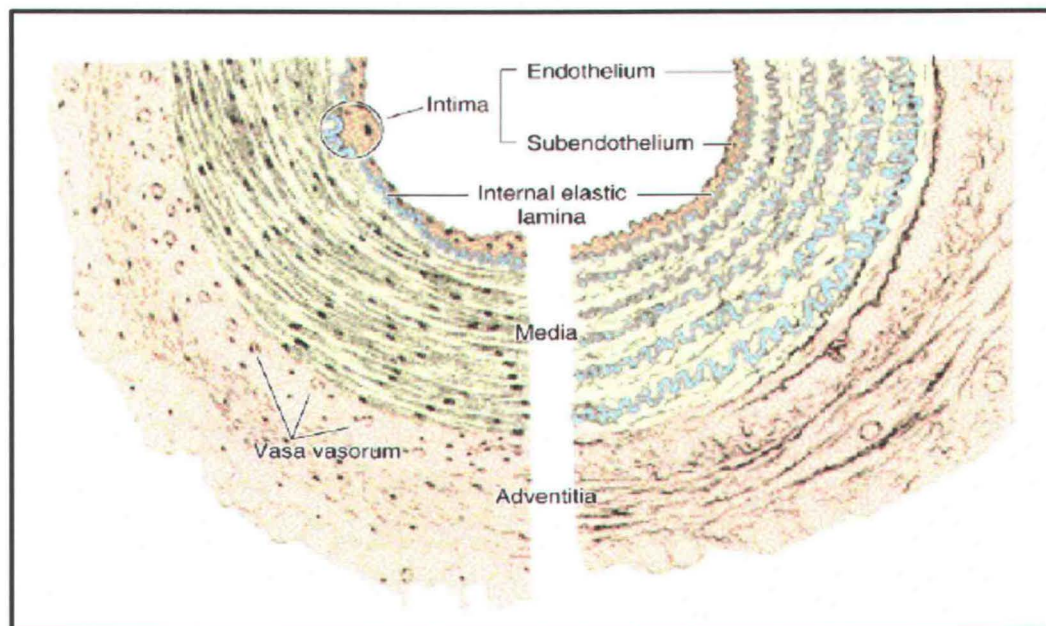


Figure 2.4 Diagram of a muscular artery prepared by staining (left) and an elastic artery stained by Weigert's method (right). The tunica media of a muscular artery contains predominantly smooth muscle, whereas the tunica media of an elastic artery is formed by layers of smooth muscle intercalated by elastic laminae. The adventitia and the outer part of the media have small blood vessels (vasa vasorum) and elastic and collagenous fibers. (Reprinted from Junqueira, 2003)

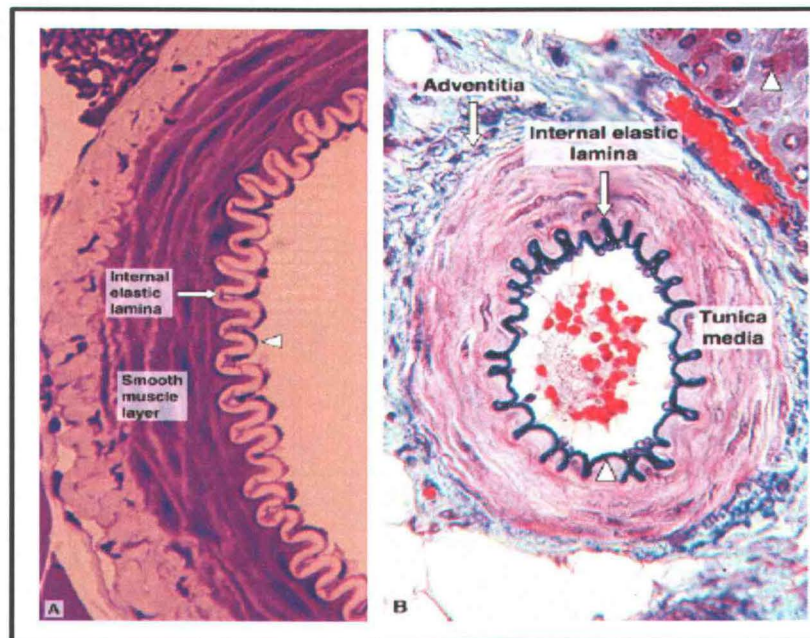


Figure 2.5 Cross section of small arteries. A: The elastic lamina is not stained and is seen as pallid lamina of scalloped appearance just below the endothelium (arrowhead). Medium magnification. B: A small artery with a distinctly stained internal elastic lamina (arrowhead). (Reprinted from Junqueira, 2003)

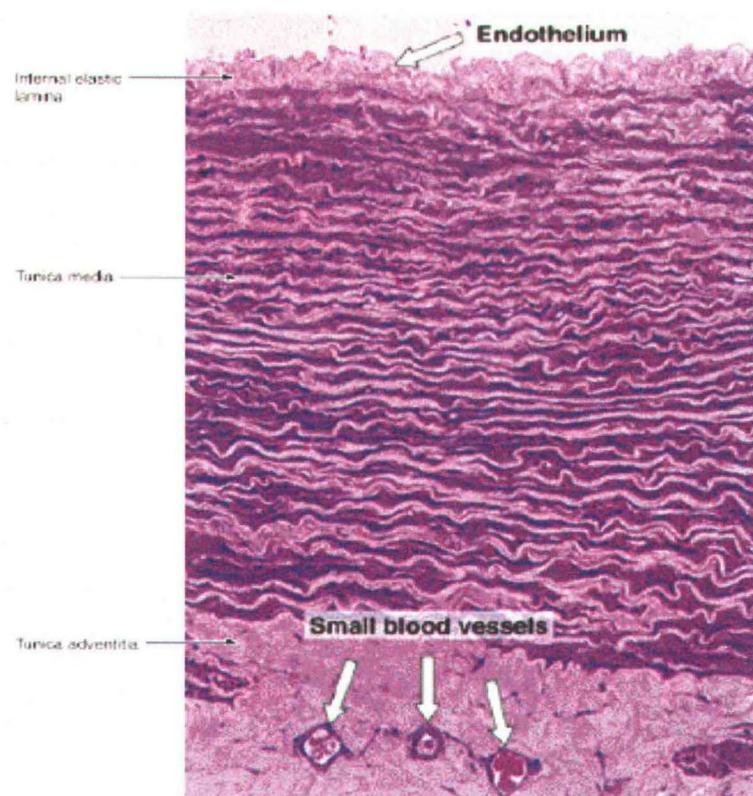


Figure 2.6 Transverse section showing part of a large elastic artery showing a well developed tunica media containing several elastic laminae. (Reprinted from Junqueira, 2003)

The tensile properties of these arteries are dependant on the structure of, elastic tissues [14]. It is to be expected that the functional structural unit of the principal layer, i.e., the media, includes both elastic tissue and smooth muscle cells. The impact of the cardiac pump and of the blood delivered with great force into the circulation is absorbed by the elastic properties of the arterial wall [14]. The actual stretching force in the wall is proportionate to the magnitude of blood pressure and the radius of the artery; therefore, it is much greater in the large than in the small arteries. In man, the tangential stretching force in the aortic wall is approximately one hundred times greater than that in the arterioles [14].

However, the arterial system is capable to a number of disorders, many of which progress slowly only to become apparent later in life. In particular, aneurysm formation depends on several factors. It used to be thought that *atherosclerosis* played a major role [15]. By definition, atherosclerosis is an arteriopathy whose one feature is hardening of the arteries. In particular, atherosclerotic lesions are distinct, well delineated, focal changes of the intima of large elastic and medium-size (muscular) distribution arteries [14]. However, today it is not widely believed that formation of aneurysms are exclusively caused by atherosclerosis. Therefore, the structural integrity of the aortic wall due to elastin and collagen has received significant attention. Elastin provides elastic recoil, and collagen gives a strong but inextensible "safety net" at high pressure. There is histologic evidence in aneurismal aortic tissue that demonstrates degeneration of the arterial wall [15, 17]. The media has become fragmented, and there are reduced numbers of elastin lamellae. A reduction in elastin from 12% in normal aortic tissue to 1% in aneurysmal aortic tissue has been noted and there is a reduction from about 35% (dry weight) to about 8%. Whatever the percentage, there is agreement that there is a focal loss of elastic tissue in the aneurysmal aorta that decreases the aorta's ability to withstand expansile forces. Additionally, defects in the production of collagen type III are associated with increased arterial fragility and aortic aneurysm [15, 17].

2.1.3 Classification and Definition of Aneurysms

Classification of aortic aneurysms is based on their location, type and pathology. According to pathological classification, there are three types of aneurysms: 1) A *true aneurysm* of aorta implies that the dilated segment is continuous with the aortic wall and it consists (at least initially) of all aortic mural components. Although in the course of aneurysmal progression the dilated segment loses its medial coat because of atrophy of smooth muscle cells and fragmentation and “disappearance” of elastic tissues, nevertheless, the dilated sac still consists of remnants of the aortic wall itself. 2) A *false aneurysm* (*pseudoaneurysm*) represents a (pulsating) hematoma which surrounds an aortic segment and is connected with the aortic lumen either through a partially served wall (*traumatic false aneurysm*) or through a dehiscence of a suture line of a prosthetic graft (*anastomotic false aneurysm*). The hematoma is contained to some extent and prevented from expanding rapidly by adjacent tissues, and eventually is surrounded by a “false sac.” This sac represents condensed fibrous connective tissues walling off the hematoma and originating from the surrounding area; none of the mural components of the aorta are present in the wall of this sac [14]. 3) A *dissecting aneurysm*, the histologic layers of the aortic wall are separated by blood entering through an intimal and medial tear (Fig. 2.8). Enlargement of the circumference of the aorta occurs as progressive extension of the false lumen proceeds proximally and distally in an intramural plane [22]. Figure 2.7 is an illustration of true, false and dissecting aneurysms.

The true abdominal aortic aneurysms are classified on the basis of their gross appearance because various forms of the aneurysms require different surgical interventions. As mentioned before, the shape and size as assessed on macroscopic examination is the basis on which aneurysms are classified [14, 23, 24]. There are three types of true aneurysm based on their gross features: 1) A *saccular aneurysm* is a sharply delineated dilatation affecting only a segment of the aortic circumference, and is spherical in shape (Fig. 2.9).

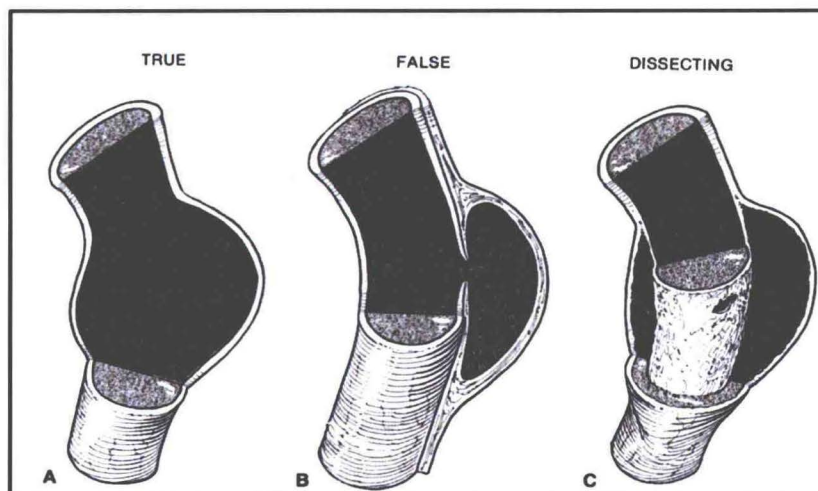


Figure 2.7 Pathologic types of aortic aneurysms. (A) A “true aneurysm has the element of the aortic wall, particularly the adventitia. (B) The pathogenesis of a “false” aneurysm is related to a traumatic, usually localized injury causing a surrounding hematoma. In recent years, a frequent cause for a false aneurysm has been disruption of vascular suture line. The aneurysm is confined by cicatricial reaction in local tissues and does not have the elements of the true aortic wall. (C) In a dissecting aneurysm, the histologic layers of the aortic wall are separated by blood entering through an intimal and medial tear. Enlargement of the circumference of the aorta occurs as progressive extension of the false lumen proceeds proximally and distally in an intramural plane (Fig. 2.8). (Reprinted from Cooley, 1986)

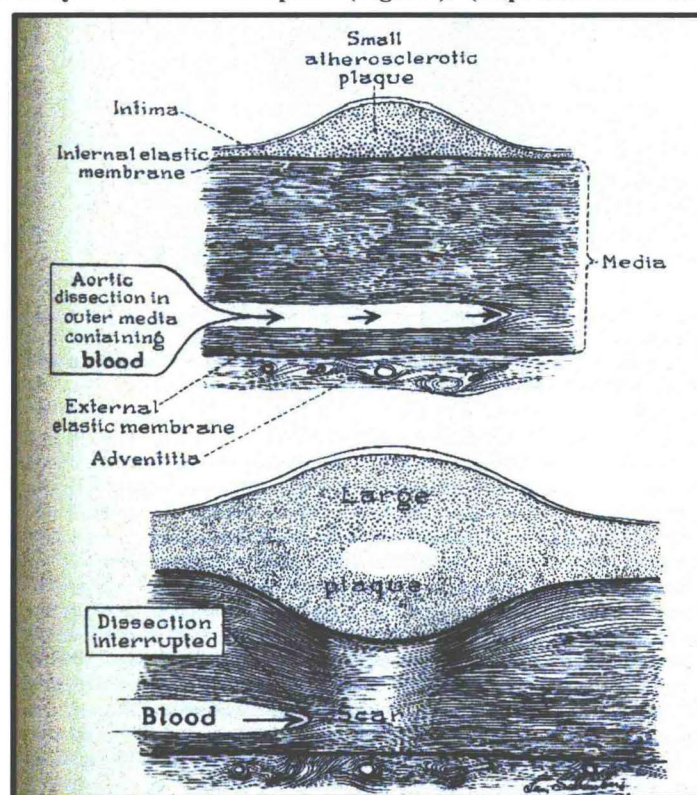


Figure 2.8 Diagram depicting the usual mechanism that causes a dissecting *aneurysm*. The histologic layers of the aortic wall are separated by blood entering though an intimal and medial tear. Enlargement of the circumference of the aorta occurs as progressive extension of the false lumen proceeds proximally and distally in an intramural plane. A large atherosclerotic plaque causes atrophy with scarring of the underlying media, and the medial scar interrupts the dissection. (Reprinted from Bergan, 1982)

Commonly, the aneurysmal sac communicates with the (main) arterial lumen by a narrow neck of small orifice, but at times the connection may be of a diameter similar to that of the aneurysm itself. Whereas usually, the diameter of these aneurysms ranges from 5 to 10cm, the sacs may be tiny, measuring only a few millimeters, or on occasion be huge and elongated, with the larger diameter being up to 15 cm. Regardless of their size these aneurysms almost always contain characteristically structured thrombi which may fill the sac completely. 2) A *fusiform aneurysm* is a dilatation involving the entire circumference of the aortic wall. Thus the overall diameter of the aorta at the level of the lesion is increased considerably. The segment of circumferentially dilated wall gradually merges with the adjacent proximal and distal aorta, resulting in a spindle-shaped aneurysm. Fusiform aneurysms may be slightly eccentric when one segment of the vascular circumference is more affected by the dilating process than other. The size and diameter of the aneurysms vary, and the length may measure 15 to 20 cm [14, 22].

The lumen of a fusiform aneurysm also becomes narrowed gradually in the distal and proximal direction from the maximal diameter at a plane passing through the center of the spindle. 3) A *cylindroid aneurysm* is defined best as a fusiform aneurysm that extends over a considerable length of the arterial wall, but “joins” the unaffected aorta at either one or both ends more abruptly or acutely than do the classical fusiform forms. The diameter of the long dilated segment of the aorta is uniformly increased [14].

In both fusiform and cylindroid aneurysms mural thrombi (see section 2.1.4 below), when present, resemble in their layered structure those of the saccular aneurysm. They do not fill and obliterate these aneurysms, unless the dilatations have existed for many years. In large aneurysms, especially those of a fusiform shape, mural thrombi may line the entire inner surface of the aorta thus narrowing the aneurysmal lumen to a diameter, often reduced to that of the normal (preexisting) aorta [14]. Figure 2.9 illustrates the difference between fusiform and sacciform aneurysms in a 66-year old man with AAA.

All aneurysmal form may affect the abdominal aorta, but the saccular type with a narrow neck and small orifice are the least common. The common

abdominal aortic aneurysm is typically a true fusiform aneurysm. Multiple aneurysms are present often. Usually the aneurysms end abruptly just above the aortic bifurcation, but may extend into the common iliac arteries and their branches.

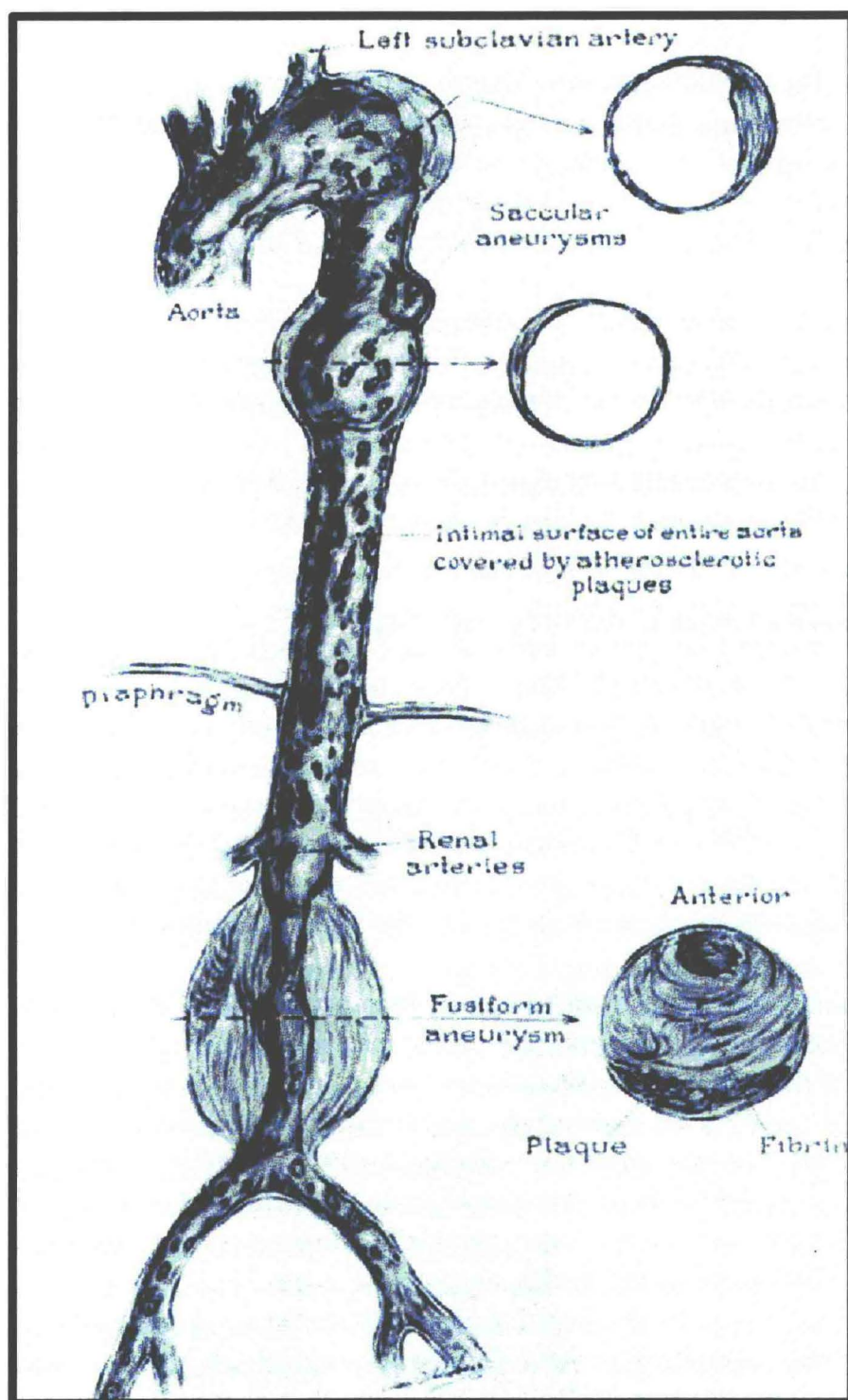


Figure 2.9 Aorta in a 66-year-old man with both saccular and fusiform aneurysms. At necropsy, the entire aorta was heavily atherosclerotic and a 6×10 cm fusiform aneurysm was present in its abdominal portion, with three saccular aneurysms in its descending thoracic portion. The residual lumen of the abdominal aorta was much smaller than normal because of the large intra-aneurysmal thrombus. (Reprinted from Bergan, 1982)

2.1.4 Thrombosis and Its Formation Factors

Thrombosis is the formation of a clot or thrombus inside a blood vessel, obstructing the flow of blood through the circulatory system. A thrombus or blood clot is the final product of blood coagulation, through the aggregation of platelets and the activation of the humoral coagulation system. (Fig. 2.10).

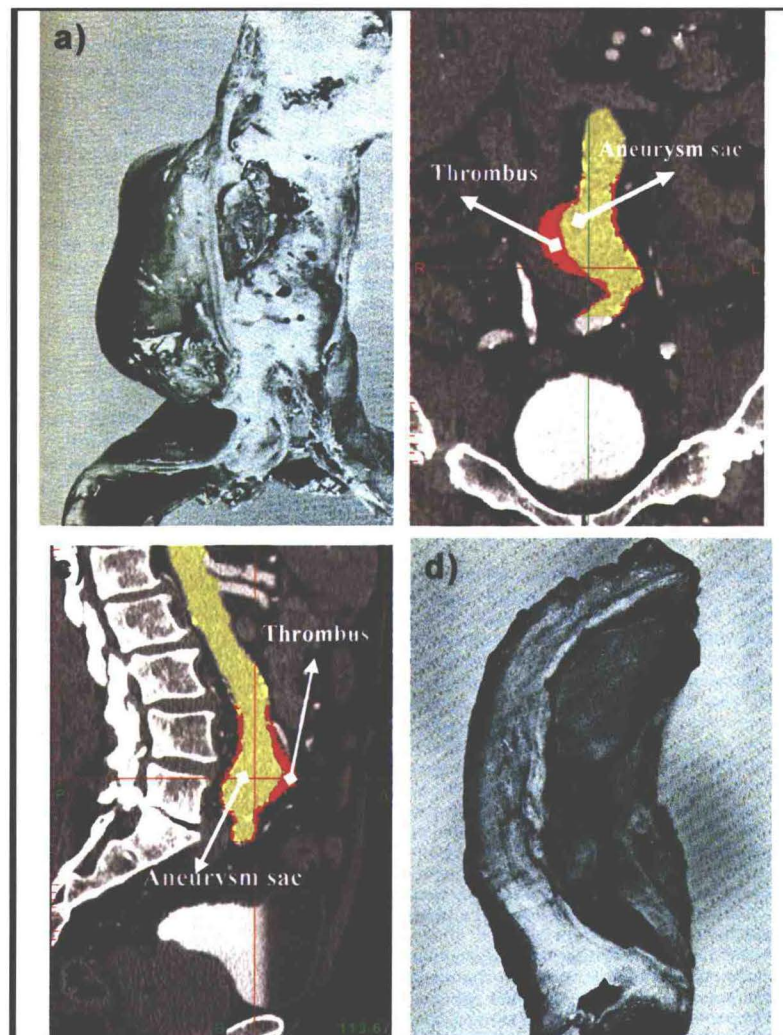


Figure 2.10 (a) Gross appearance of a saccular aneurysm of the infrarenal abdominal aorta. Note that the thrombus contained in the aneurysm consists of several layers. (Reprinted from Silver, 1983), (b) Coronal cross section of patient abdominal CT scan: The aorta has been identified as a yellow path and its thrombus has been identified with red. (c) Sagittal cross section of patient abdominal CT scan: The aorta has been identified as a yellow path and its thrombus has been identified with red. (d) Cross-cut section of a saccular aneurysm similar to that illustrated in (a). The thrombus present does not fill the dilated segment. It does not adhere firmly to the aneurysmal wall and consists of several layers indicated by faint lines of Zahn. Note the considerable thickness of the periarterial (adventitial) connective tissue. (Reprinted from Silver, 1983)

Various measures designed to induce thrombosis within an aneurysm have been proposed and employed in order to achieve fibrotic or organization of the process and thus prevent or delay the inevitable perforation of sac. Matas classified techniques that assist in this effort by 1) diminishing the blood pressure, 2) retarding the velocity of circulation, 3) increasing the coagulability of blood, and 4) provoking thrombus formation within the sac by agents that act directly on the aneurysmal tissues from within and from without [22].

When free of thrombosis, the intimal surface of aneurysms often shows ulcerated atherosclerotic lesions. Many of these expose a yellow central atheroma, or are superimposed by a small mural thrombus [14].

2.1.5 Age, Gender, Race and Etiology of Aneurysms

The AAA is the most prevalent type of aneurysm. Thus, a great deal of research has been devoted to uncovering its etiology.

The incidence of all AAA at postmortem examination has remained virtually unchanged since the middle of the 20th century, varying in different series from 0.52 percent to 3.98 percent. In a recent review-study based on reported series, the overall incidence of AAA was 1.2 percent of all postmortem examinations [14]. However, when assessed separately for age and sex, there was a 6 percent incidence for men dying in the sixth decade of life, 10 percent in the seventh, 12 percent in the eighth, and 14 percent in the ninth. In another large series of patients who were treated surgically and ranged in age from 33 to 90 years, the occurrence of AAA peaked in the seventh decade and 20 percent of patients were 70 years or older [14].

Women with aneurysm are reportedly two to eight years older than men on average, and men are more susceptible than women by a factor ranging in various series from 2.4 to 9.6. The overall ratio of men to women affected is quoted as being 5:1 or 6:1 and apparently is not altered appreciably by separating the instances of ruptured AAA from those that remain intact [14].

Bergqvist (1970) also reported that the frequency in men increases rapidly at age greater than 55, reaches a peak prevalence of 5.9% at 80 to 85 years, and

then decreases. In women there is a continuous increase after 70 years of age, reaching 4.5% at age greater than 90 (Fig. 2.11) [26].

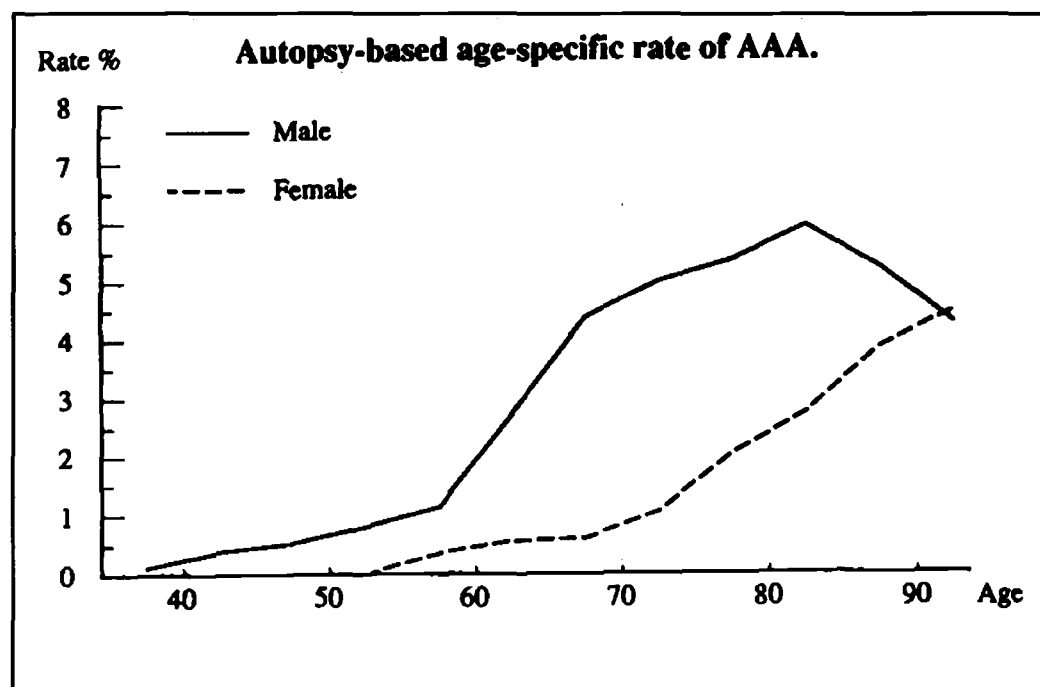


Figure 2.11 the frequency in men increases rapidly at age greater than 55, reaches a peak prevalence of 5.9% at 80 to 85 years, and then decreases. In women there is a continuous increase after 70 years of age, reaching 4.5% at age greater than 90. (Reprinted from Yao, 1994)

In only a few studies was race taken into consideration as a factor in AAA, or in atherosclerotic aortic aneurysms in general. The earlier reports indicated that the incidence is considerably higher in the black population than in the Caucasian population. Almost 80 percent of AAA in one study in 1936 and 61.2 % of all aortic aneurysms in another, 20 years later, were reported to occur in blacks. However, in a large necropsy series published only six years later, arteriosclerotic aortic aneurysms were over twice as common in the white (6 percent) as in the black (2.7 percent) population. Moreover, results tabulated from five different studies on atherosclerotic aneurysms, published from cities with a large black population between 1954 and 1964, indicate that only 4.3 percent occurred in black population [14]. Whereas it is not possible to assess adequately the available studies because some are concerned only with AAA and others relate to all aortic aneurysms. However, it is possible that the more recently reported low incidence

of AAA in the black population reflects a lower aortic susceptibility to atherosclerosis in the black than in the white population [14].

Systemic hypertension and a known history of cigarette smoking have been documented as factors positively associated with the occurrence of aneurysms [14].

Consequently, there are five main risk factors for aneurysms: (1) smoking, (2) family history, (3) peripheral vascular disease (PVD), (4) hypertension, and (5) age. The relative risks of developing an AAA in association with smoking are not quite as high as for lung cancer and smoking. However, they are greater than those found in the coronary artery disease and smoking relationship [17]. There is also evidence that smoking increases the growth rate of AAA [25].

A genetic disorder that is sometimes incorrectly associated with aneurysms is Ehlers-Danlos syndrome (EDS). There are many types of EDS, each with very different clinical symptoms. Only type IV EDS manifests frequent cardiovascular problems, and it is this type which is often mistakenly associated with aneurysms. Patients with Type IV EDS commonly exhibit the following symptoms: severe bruising, thin transparent skin, joint hypermobility of the fingers, spontaneous perforation of the colon, and frequent arterial ruptures. The arteries of these patients are extremely fragile, and they tend to rupture by tearing without dilating. True aneurysms do not usually, if ever, occur in EDS patients. Type IV EDS is known to be caused by defects in Type III collagen [26].

A family history of AAA is worth inquiring about. A first degree relative of an affected individual has over 10 times greater a risk to develop an AAA than a non-first degree relative of similar age and sex. Using ultrasonography brothers of patients with AAAs have an incidence of AAAs from 20%-29% and sons have an incidence of about 20%. Daughters have an incidence of about 4.4%, not much higher than the incidence in the general population [15].

Based on a large screening of patients referred to vascular surgeons with atherosclerotic disease of the peripheral or carotid arteries, the incidence of AAA in men was 11.5%, and in women 6.2%. However, this study was heavily biased by the smoking histories of the patients [17]. Hypertension (diastolic more so than

systolic) is considered a risk factor from the standpoint of risk of rupture of AAA and an important influence on death from dissection [15].

Several recent studies of the histopathologic changes of AAA have demonstrated that the walls of AAAs are markedly deficient in both collagen and elastin. In separate studies in 1982, Busuttil *et. al.*, Cannon and Read were the first to report increases in elastase activity in AAA disease [40]. Cannon and Read attributed the increase to leukocyte elastase. In 1989, Dobrin reported that treatment of excised canine and human cadaver arteries with elastase results in significant wall distention, while treatment with collagenase results in rapid rupture without much distention [26]. Based on these observations, Dorbin concluded the following: 1) Elastin is responsible for keeping vessels at their normal size and providing wall compliance. 2) Collagen provides the vessel with tensile strength. He then suggested that under normal conditions elastin bears most of the load; although as a vessel distends, more and more collagen is required to share the load. In light of the complex microarchitecture of the arterial media and the unsteady nature of its mechanical environment, this is certainly a simplification. However, these studies suggest a biochemical basis for the occurrence of AAAs.

2.1.6 Clinical Treatment of Aneurysms

Open-abdomen repair has been done since the 1950s. In 1976, Yao *et. al.* began to develop a plan for endovascular treatment of abdominal aortic aneurysm. Two prototypes were developed [26]. The first is a self-expandable metal cage with a zig-zag configuration covered by a nylon fabric. The second is a Silastic bag with a cylindrical lumen. Both prototypes were eventually abandoned because of the discouraging results with placement in animals. With the stent technology emerging in the field of endovascular treatment, they reinitiated their project in 1988 using balloon-expandable stents (Fig. 2.12). They update their recent clinical experience of this new technology in 32 patients. Yao *et al.* current approach is predicated on the concept that stents may be used in place of sutures to secure the proximal and distal ends of a fabric graft within the lumen of the aortic aneurysm.

With the use of graft-stent combination, it is now possible to treat patients with aortic aneurysm by transfemoral placement of a prosthetic graft [26].

The graft-stent device is depicted in Figure 2.12. The assembly contains one balloon-expandable stent, 5.5 mm in diameter and 3.5 cm long. These are stainless steel, modified Palmaz stents. A specially created thin-wall, crimped knitted Dacron graft (Barone Industries, Buenos Aires, Argentina) was sutured to the stents, over lapping half of the length of the stent. The stent is made of annealed stainless steel, and the alloy has been widely used in a variety of prosthetic applications [26].

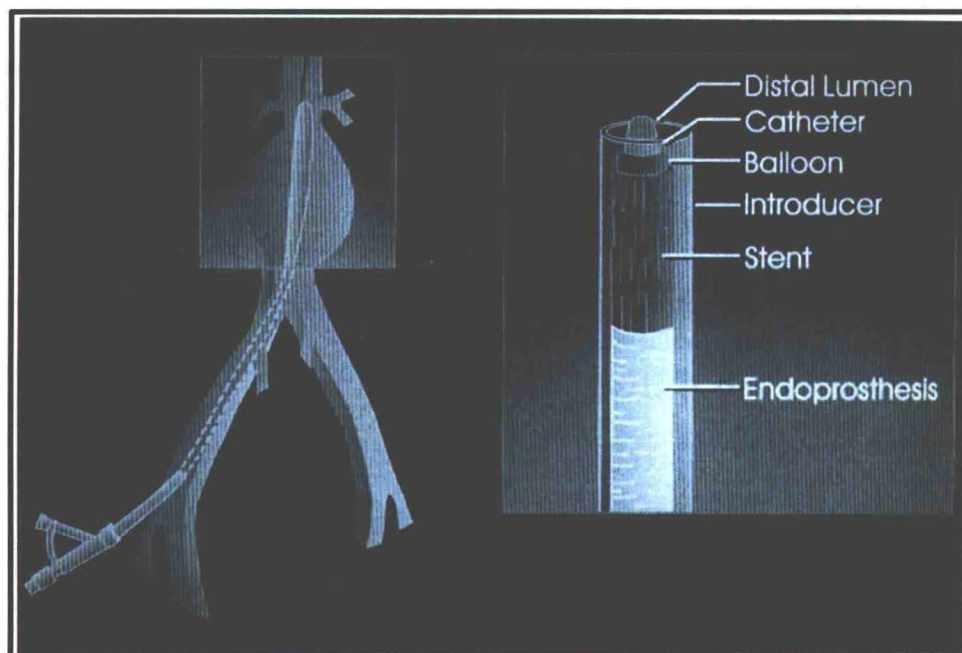


Figure 2.12 Transfemoral intraluminal graft implantation for abdominal aortic aneurysm: Stent-graft combination device for intraluminal placement through the femoral artery. (Reprinted from Yao, 1994)

The procedure of transfemoral intraluminal graft implantation for AAA which is carried out in the operating room can be summarized as following (Fig. 2.13): 1) Once particular measurements are obtained and the size match between the patient's aorta and the graft are confirmed, the catheter-based capsule containing the graft is then introduced into the sheath and advanced under fluoroscopic control to the proper position in the abdominal aorta. The position of the proximal stent in the subrenal location is critical and is aided by a radiopaque

cursor system. 2) Once the proximal stent is in the ideal position, the capsule is then remotely withdrawn and the proximal portion of the graft with the self-expanding stent is allowed to deploy. 3) The implantation balloon is then pulled back into position and expanded. The expansion seats the pins on the self-expanding stent and drives them into the wall of the aorta. 4) The balloon is deflated and the remainder of the capsule withdrawn to allow the distal self-expanding stent to deploy into the aorta proximal to the iliac bifurcation. 5) The balloon catheter is pulled back into position and expanded to achieve final fixation of the distal portion of the graft.

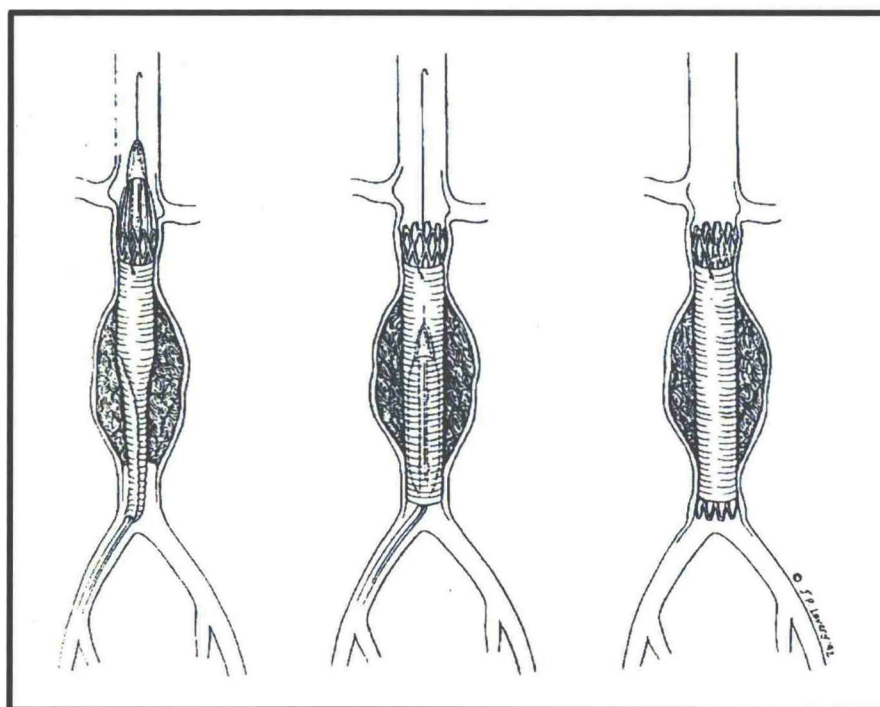


Figure 2.13 Transfemoral intraluminal graft implantation for abdominal aortic aneurysm: Step in the deployment of proximal and distal stents. From left to right: 1) The catheter-based capsule containing the graft is introduced into the sheath and advanced under fluoroscopic control to the proper position in the abdominal aorta., 2) Once the proximal stent is in the ideal position, the capsule is then remotely withdrawn and the proximal portion of the graft with the self-expanding stent is allowed to deploy, 3) The implantation balloon is then pulled back into position and expanded. The expansion seats the pins on the self-expanding stent and drives them into the wall of the aorta. (Reprinted from Yao, 1994)

2.1.7 Previous Clinical Studies

Abdominal aortic aneurysms are common and show increasing occurrence among the elderly population. For most patients with AAA, the aneurysm is the leading threat to life [27]. The risk factors vary widely among patients. However, based on the present data for older persons with an AAA, if the size is 3-5 cm and the patient is symptomatic, surgery is strongly considered [15]. If the patient is asymptomatic, he or she is normally followed every 3-6 months with an ultrasonography (or other radiological test). If the aneurysm changes more than 1 cm per year, surgery is strongly considered.

If the AAA is 5-6 cm, whether the patient is medically stable or unstable, the risk of rupture (0.4%-20% per year) plus the risk of death from emergency surgery (at least 50%) are weighed against the risk of death from elective surgical repair (roughly 5%) [15].

If the AAA is more than 6 cm and the patient is medically stable, risk of rupture and death are probably higher than risk of death from elective surgery. If the patient is medically unstable, and in that "high risk" category, two options exist: maximize the patient's medical condition and do surgery, or do not do surgery and concentrate on modifying risk factors and dealing with quality of life issues [15].

Most research has focused on finding a critical diameter for rupture, and predicting growth rates of aneurysms. It is agreed that rupture risk increases in an uneven rate as the aneurysm diameter increases. As previously mentioned, the absolute diameter of an AAA is not always indicative of the severity of its effect. The rupture risk is affected by the ratio of dilated to undiluted diameter. A study by Powell found that for 43 patients the median growth rate was 0.13 cm per annum [26]. The growth rate did not appear to depend on initial aneurysm diameter or sex. Rarely did the change in diameter, at annual follow-up, exceed 0.5cm, that is, signify real growth; however, the growth rates were obtained from the trend in aneurysm diameter over 3 years (four measurements). These growth rates for small asymptomatic aortic aneurysms in patients with peripheral arterial disease obtained over 3 years are lower than those reported for aneurysms of

similar size detected by population screening in a larger Canadian Study and other studies (Table 2.1) [26].

Patient Group	n	Reference	Aortic Diameter		Growth rate (cm/y)
			Measurement*	Range (cm)	
High risk	99	1984 San Diego, USA ¹⁴	Transverse, ultrasound	3-6	0.4
Screen detected	50	1989 Oxford, UK ¹⁶	AP, ultrasound	2.5-5	0.3
Screen detected	71	1991 Oxford, Gloucester, UK ¹⁷	AP, ultrasound	3-4	0.25
High risk	114	1991 Liege, Belgium ¹⁸	Transverse, CT and ultrasound	<4 4-4.9	0.53 0.69
Small aneurysms	268	1992 Kingslon, Canada ¹⁹	Transverse, CT and ultrasound	3-3.9	0.39
Arterial disease	43	1993 London, UK	AP, ultrasound	4-4.9 3-5	0.66 0.13

*AP = anteroposterior; CT = computed tomography.

Table 2.1 Growth rate of Abdominal Aortic Aneurysms: These growth rates for small asymptomatic aortic aneurysms in patients with peripheral arterial disease obtained over 3 years are lower than those reported for aneurysms of similar size detected by population screening in a larger Canadian Study and other studies.

From these studies there is evidently a large amount of variability in both aneurysm diameter and growth rate effects on rupture. Other criteria based on the hemodynamics of blood flow are necessary to more accurately predict the risk of rupture. A recent clinical study [28] found that *in vivo* AAAs can exhibit regular, laminar flow, and randomly fluctuating turbulent flow. Furthermore, they discovered a correlation between a frequent aneurysm rupture site, the distal region, and areas of turbulent flow just proximal to mural thrombus deposition. These findings support an earlier study by Muraki who suggested that mural thrombi forms in the distal region initially, and then develops proximally [28]. Since this region of constriction is believed to be a region of the wall which experiences the maximum stresses, Muraki's and Bluth's observations suggest that turbulence increases the risk of rupture.

2.2 BIOMECHANICS

As previously discussed, aneurysm initiation is probably created by biochemical abnormality factors. These factors are instrumental in weakening the arterial wall, however the growth and eventual rupture of the aneurysm depends on mechanical factors. Since pressure and flow pulsations are transmitted by the blood within the vessel, it is stretched and relaxed approximately 100,000 times daily. Fluid flowing through an aneurysm exerts a vector force which has both normal and shear stresses on the vessel wall. In a normal situation, the vessel is equipped to resist these forces, but in an aneurysm, when stresses exceed the strength of the wall, rupture occurs.

2.2.1 Experimental Simplifications and Assumptions

In the pressure measurement section of this study, several simplifying assumptions were made so as to reduce the complexity of the models. Tap water, which behaves as a Newtonian fluid, was used as the working fluid even though blood does not, in the strict sense, behave as an ideal Newtonian fluid. The presence of cells causes the viscosity of blood to vary as the shear rate varies. This simplification can be justified by the study of Fung [29] on blood rheology. This study reported that the non-Newtonian feature of the blood is negligible in large vessels where shear rates are relatively high. Hence, blood is often modeled as a Newtonian fluid in studies of flow through large arteries.

The models which were used for pressure distribution measurements on the wall, also neglect the celiac, renal and iliac arteries which were made so as to reduce the complexity of the flow loop table. Clingan and Friedman [30] studied the effects of the outflow of aortic blood through the celiac and renal arteries on the flow field in the external iliac arteries were studied under both steady and pulsatile flow conditions. Their steady flow results indicated that while the outflow through the renal arteries did not have a significant effect on near wall shear rate in the external iliac arteries, the flow through the celiac artery did.

One of the simplest analytical models which can be applied to the bulge geometry is the law of Laplace. Indeed, knowledge of a patient's maximum wall stress is very important, because when the actual wall stress reaches the patient's tensile strength, the aneurysm wall ruptures. Unfortunately, a patient's tensile strength is usually unknown and maximum wall stress *in vivo* is almost impossible to measure. In fact coupled fluid-structure interaction models may be the only way to generate reliable wall stress data. Therefore, as a first step in understanding wall stresses, the engineering studies of aneurysm mechanics ignored the flow by modeling the aneurysm as a thin-walled spherical pressure vessel with an applied static pressure. In this case, the stress in the vessel wall is then approximated by the law of Laplace [42],

$$\sigma = \frac{PD}{4cT} \quad (1)$$

where σ is the average wall stress, P is the pressure load, D is the diameter of dilated sphere or cylinder and t is the wall thickness, while $c = 1$ is for cylinder and $c = 2$ for sphere.

If the non-dilated spherical vessel has a diameter of d and a wall thickness of t , and constant volume is assumed, the dilated sphere will have wall thickness which can be described by $T = td^2 / D^2$. Replacing T in the equation 1 yields an equation for tensial wall stress, based on the ratio of dilated to non-dilated diameters [42]:

$$\sigma = \frac{PD}{4t} \times \left(\frac{D}{d} \right)^2 \quad (2)$$

As explained above, a normalized diameter (D/d) better correlates to wall strain and ultimate rupture than simply generalizing a standard diameter D , since the wall stress even in this highly simplistic model depends on both the dilated and undilated vessel diameters.

While modeling an aneurysm as above is a useful exercise that provides some insight into the mechanics, real aneurysms bear little resemblance to thin-walled, static, spherical pressure vessels. Aneurysm walls are not necessarily thin,

and they are certainly not spherical in shape, as well, their expansion takes place over many years, and is most likely not constant-volume procedure.

A more accurate model of aneurysmal fluid mechanics should include pulsatile flow, possibly turbulent flow and resultant pressure and wall shear fluctuations which will influence aneurysm growth and rupture of the lesion. In order to accurately model aneurysm mechanics, then, it is necessary to study the flow in detail, paying particular attention to the forces that it exerts on the aneurysm walls. Therefore, dynamic similarity must be satisfied.

2.2.2 Dynamic Similarity

To achieve reliable predictions of the forces which are produced by the flow behavior in the real situation or prototype, experimental models must be dynamically similar to *in vivo* aneurysms. If a model and prototype satisfy both geometric and kinematic similarity requirements, then they are dynamically similar. Geometric similarity ensures that any length in the model system is related to the corresponding length of the prototype by a constant scale factor. Likewise, kinematic similarity relates that the velocity magnitudes and directions of corresponding particles are in a fixed ratio at corresponding times. If these two conditions are satisfied, fluid forces in the model flow will be related to those same forces in the prototype flow by a constant scaling factor.

Geometric similarity is relatively easy to satisfy for rigid structures. In the present study, our phantoms are rigid flow-through replicas of the AAA lumens which exactly duplicated the patient *in vivo* geometry.

To achieve kinematic similarity, the governing dimensionless flow parameters of the model must be matched to those of the prototype. In this case, the Reynolds number and the Womersley number are the important governing dimensionless parameters. Since in this study we were interested in measuring pressure distribution of the AAA luminal walls with steady state flow, Reynolds number was the only important governing parameter. It is also common to begin

with steady flow experiments, which will often provide considerable insight into the real flow situation.

The Reynolds number, Re , is a ratio of inertial to viscous fluid forces, as defined below,

$$Re = \frac{Ud}{\nu} \quad (3)$$

where U is the mean flow velocity, d is the undiluted vessel diameter, and ν is the kinematic viscosity of the working fluid. This ratio shows when the Reynolds number is low, viscous forces dominate and the resulting slow flow is laminar. In contrast, for a straight pipe when the inertial forces dominate at high Reynolds number ($Re > 2000$), the flow is usually turbulent with blunt velocity profiles. The Reynolds number can also be written in terms of the volume flow rate Q for a rigid, straight pipe:

$$Re = \frac{4Q}{\pi d \nu} \quad (4)$$

where Q is the flow rate, d is the undiluted inlet tube diameter, and ν is the kinematic viscosity of the fluid.

2.2.3 Previous Engineering Studies

The flow visualization investigation of steady flow through three axisymmetric models was performed by Scherer in 1973 [31], which was the basis of modern *in vitro* aneurysm analysis. He used spherical, glass models which joined the inlet and outlet tubes with sharp edges. According to his investigation: 1) under laminar conditions, a core of swiftly moving fluid passed through the bulge center, and was surrounded by a recirculating vortex in the bulb area. The fluid velocities within these vortices were significantly smaller than those in the core flow; 2) the flow was laminar up to a critical Reynolds number which depended on the ratio of the maximum bulge diameter to the inlet diameter (D/d). For instance, for the smallest model, with $D/d = 2.0$, the transition occurred at $Re = 2800$; 3) it appeared that pressures on axisymmetric aneurysm walls are between those

upstream and downstream and that local pressure maxima within the bulbs do not occur [31]. To measure pressure differences at several points on the bulb wall, Scherer used a water manometer. Although a good initial study, model geometry was a limitation to Scherer experiment. The models were spherical, which not only presented sharp edges at the bulb inlet and outlet, but also they did not accurately model the true physiological aneurysms shape. However, most AAAs are not spherical. The sharp edges of Schere's models interfered with the flow patterns.

In a 1976 study, Tam et al. related Re and geometry to pressure and velocity using intraluminal pitot static pressure measurements in four different models. Tam's investigation also confirmed and extended Scherer's basic description of the flow. Making comparisons between turbulent and laminar flows through this study were difficult since all flow rates were high ($Re > 2000$). In this study both luminal and wall pressures were measured. Although the pressure probes were invasive, and probably changed flow slightly, they were able to measure pressure throughout the aneurysm lumen, from the center axis to the wall. Although in most models, inlet velocity was often greater than outlet velocity, pressure at the inlet was observed higher than that at the outlet. This observation contravened the Bernoulli principle, which predicts lower pressures at regions of higher velocity along the same streamline. The highest luminal pressure primarily occurred just before the outlet. He also concluded that the places where flow is converging and reattaching would logically be areas of high stresses, both shear and normal.

It is difficult to infer the pressure differences at the wall from Tam's experiment because the flow pattern changes from straight flow to rotational vortices from the center axis to the wall. He also found: 1) pressure distributions are associated with the value of Re , the degree of divergence/convergence of the aneurysm, and degree of dilation; 2) as Re increases, pressure decreases and pressure differences increase; 3) pressure are highest in converging zone, 4) wall loading and stresses are not necessarily predictable from geometry.

In 1999, Budwig analyzed steady flow in early development AAA models by combining numerical and experimental techniques. Although spanning some of

the physiological Re , his pressure simulation studies did not include fully turbulent flows. He concluded that: 1) pressure increases with increasing longitudinal distance in the recirculation zone because flow is in the negative direction [33]; 2) the total pressure drops through dilated regions were less than the pressure drop through a uniform cross-sectional tube, since the radius is larger than a uniform tube. Thus, at the distal end there was a high amount of pressure; 3) both shear and normal wall stresses appear to peak near the reattachment points; 4) as Re increases in the laminar flow range, the vortex center moves towards the distal region of the aneurysm. The movement of the vortex might correspond with downstream shift of the pressure maxima. His conclusions from flow description agreed with previous studies by Scherer [31] and Asbury *et. al.* [34].

Vorp *et. al.* (1998), Elger *et. al.* (1996) and Stringfellow *et. al.* (1987) have also evaluated AAA wall internal stress magnitude and its dependence on bulge shape and diameter. For initial purposes they utilized simplified boundary conditions at the fluid-wall interface neglecting shear effects and assuming pressure to be a single constant [9, 12, 13]. These analyses represent an important first step towards a quantified representation of the wall stress state, but considering more complex boundary conditions for accurate stress analysis is necessary since flow patterns within the AAA can be strongly influenced by the magnitude and distribution of all components of the flow-induced forces on the bulge wall. In addition, variation of the flow during the course of the cardiac cycle can magnify the importance of not assuming pressure to be constant at the wall boundary.

A (1996) investigation by Peattie *et. al.* showed that the flow in a model bulge may become unstable and exhibit random velocity fluctuations even under carefully controlled, ostensibly steady flow conditions [35, 36]. When instability occurs, peak instantaneous shear stresses at the wall may reach 20 times their mean value [38]. Studies by Budwig *et. al.*, Egelhoff *et. al.* and Bluestein *et. al.* have demonstrated flow instability *in vitro* [38-40], which also have been confirmed by Bluth *et. al.* (1990) investigations on existence of both stable, laminar and unstable, randomly fluctuating flow patterns *in vivo*.

The results of Budwig *et. al.* and Asbury *et. al.* demonstrated that a slug of turbulence in the entrance tube grows much more rapidly in the aneurysm than in a corresponding length of uniform cross section pipe. When turbulence is present in the aneurysm the recirculation zone breaks down and wall shear stress returns to a magnitude comparable to that in the entrance tube [38].

Recently, investigations in our laboratory (Peattie *et. al.*, 2004) have presented measurements of the flow field and wall pressure in series of fusiform AAA models with different bulge diameters under unsteady flow conditions dynamically simulating the *in vivo* abdominal aorta. Wall shear stress distributions have been also evaluated from the velocity measurements. These measurements also have shown that as the bulge expands, the flow field becomes increasingly complex and its susceptibility to instability increases [37].

As a result, the ability to simulate aneurysm bulges with anatomic accuracy is crucial for understanding the pathologic risk of specific lesions. Moreover, those studies that have been reported have not considered the seemingly minor geometric differences between patient aneurysms which can have major effects on their stress development, and thereby on their risk of rupture.

2.2.4 Specific Goals of This Study

This project attempts to address some of the issues discussed above. The overall goal of this study is to characterize a series of patient aneurysms based on their geometric parameters, wall pressure distributions, ages and genders. Geometric properties of AAAs were measured and compared. To evaluate all such parameters, computational models of a series of real patient AAAs were constructed from abdominal CT series using specific software (*MIMICS*, Materialise Inc). AAAs then were categorized based on having measurable thrombi and not having thrombi.

Finally, once satisfactory computational AAA models were created, wall pressure magnitude and distribution were evaluated under steady flow conditions in three phantoms constructed from the models.

CHAPTER 3: METHODS

3.1 GEOMETRIC PARAMETERS MEASUREMENT

3.1.1 *Description of Abdominal CT Scans*

Three-dimensional model AAAs in this study were constructed from CT series obtained from the presenting patient population of Hartford Hospital (Hartford, CT). This population included 35 patients who underwent elective repair of an AAA from November 2002 to March 2005. Abdominal CT scans from 35 individual patients were obtained with GE 9800 spiral CT imaging system using blood marker for contrast enhancement at 5mm axial resolution, reconstructed to 0.6-1mm axial separation.

Each of the initial patient CT series was composed of approximately 300-600 individual CT images, in a *.pat* format. They were obtained from the level of T11 or T12 of Thoracic curve to the Coccyx for quantifying abdominal body composition and diagnosing thoracic, infrarenal, abdominal or iliac aneurysms.

3.1.2 *Importing CT scans into MIMICS software*

The first step for constructing three dimensional model AAAs of each patient was importing CT images, in a *.pat* format to *MIMICS* software, in a *.mcs* format. There are three ways to import images to *MIMICS*, depending on the file format:

1. Automatic import, when the format of the files is known to *MIMICS*
2. Semi-automatic, e.g. Bitmap or Tiff images
3. Manual import, when the file type is unknown and some parameters must be specified manually.

Since all the CT images were known to *MIMICS*, they were imported through the first method, via an *import wizard* function. This function was utilized to import and set orientation parameters for all patient files. This process involved the 5 steps described below:

1. An *Import Project Wizard* is displayed when the import images option was selected.

2. A list of files was displayed in the Filename column. Each list is known as a *project* which contained a set of CT images. Most of our patient files usually contained more than one set (project). For instance, a patient CT could be found with four image sets that contained 42, 1, 497 and 58 CT slices respectively. In this case, the file with 497 slices was selected to convert, since more slices indicate less axial separation and consequently more accurate three dimensional AAA (Fig. 3.1). For each patient all the image sets were checked and the one with maximum layers was chosen to convert.

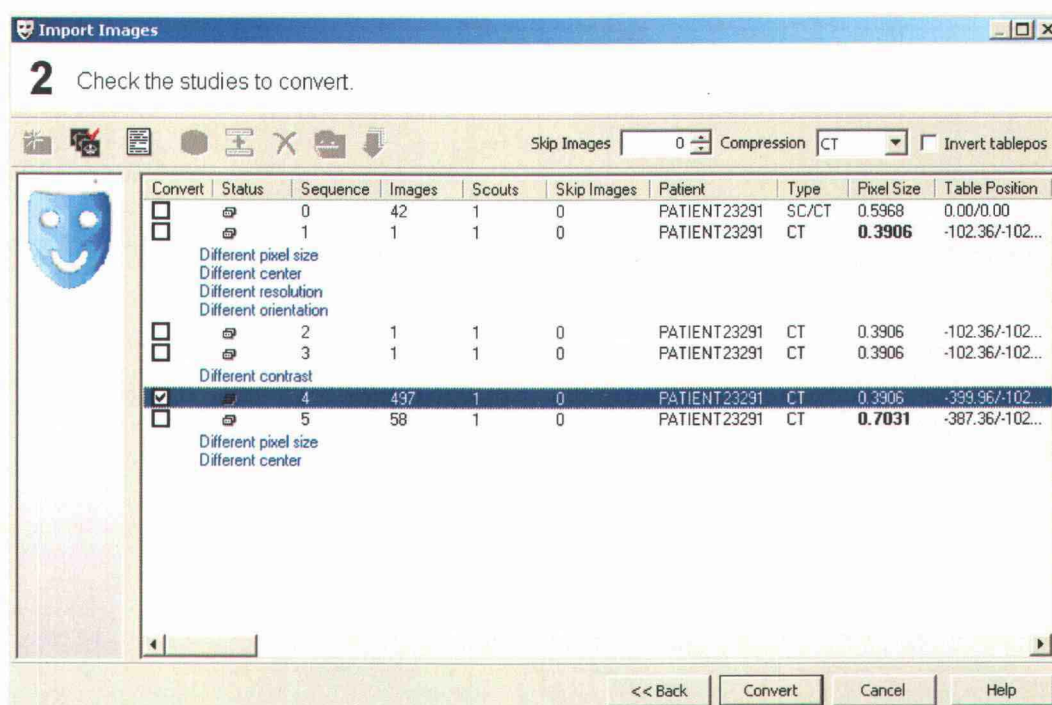


Figure 3.1 The Import Project Wizard. In this window some information about the project can be found, such as the number of images, pixel size, patient ID code and orientation parameters.

3. Other information about project was also controlled before automatic conversion, such as *status* which shows whether the file contains slices with a different center, resolution, contrast or pixel size. However, all the patient CT files with the maximum number of images contained CT slices with same value for these properties.

4. Once all the project information was checked, the conversion command was applied. The project was opened automatically displaying the *change*

orientation window, since one or more of the orientations were missing in the original images. In *MIMICS*, three different views of a CT slice can be seen at same time: axial, sagittal and coronal. Within *MIMICS*, x , y , and z coordinates system were assigned in such a way that the z -direction was oriented along the patient body axis (parallel to the spinal cord).

In the axial image the orientation strings Left (L) and Right (R) were shown together with Anterior (A) and Posterior (P). In the coronal and sagittal images in addition to L and R, the orientation strings Top (T) and Bottom (B) were shown (Fig. 3.2). Consequently, these strings show the coordinate directions, where T, B, L, R, A and P correspond to $+z$, $-z$, $+x$, $-x$, $+y$ and $-y$ respectively.

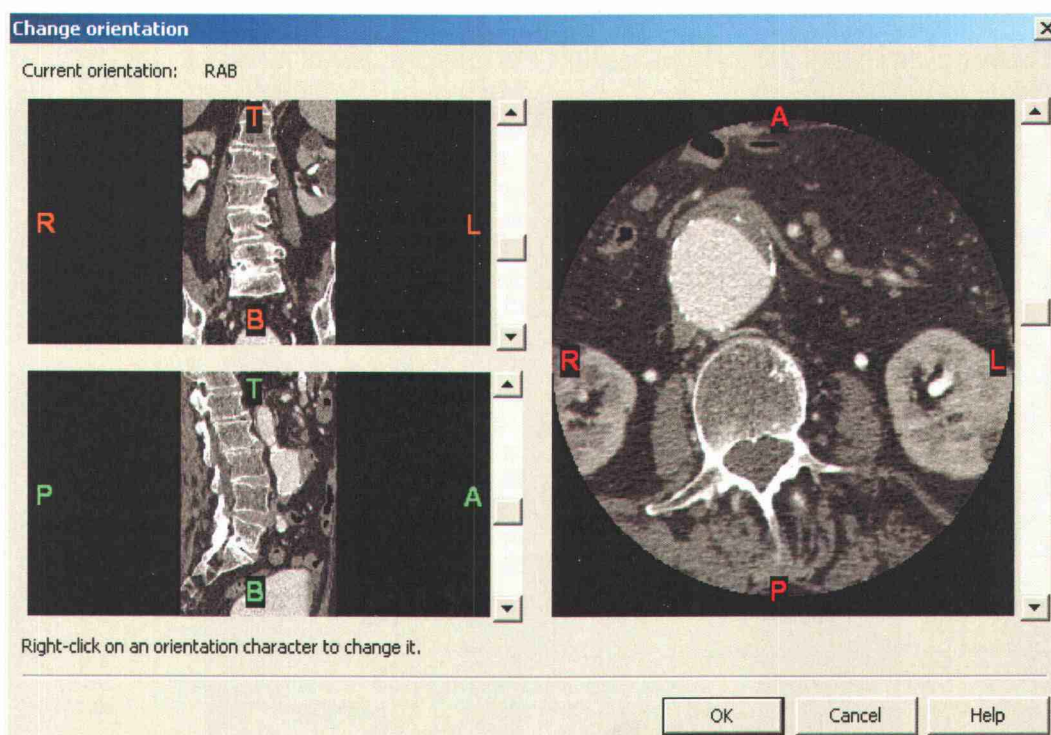


Figure 3.2. The Change Orientation window. In all three images, axial, coronal and sagittal, orientations have been shown as: Left (L) and Right (R), Anterior (A) and Posterior (P), Top (T) and Bottom (B).

5. Once the orientation was adjusted, the Mimics project was opened for image processing and creating 3D Models.

All the 35 patient files were imported into *MIMICS* in this manner.

3.1.3 Region Growing and Mask development

Once the files had been imported into *MIMICS*, image contrast was adjusted on a case-by-case basis to optimize distinguishing between the lumen, thrombus and wall of the patient aorta. Minimum and maximum contrast values were selected for each image to facilitate accurate establishment of the wall boundary position (Fig. 3.3). In some cases, *soft tissue scale* was selected, which appeared as an option of *predefined scale* in the *image contrast dialog box*.

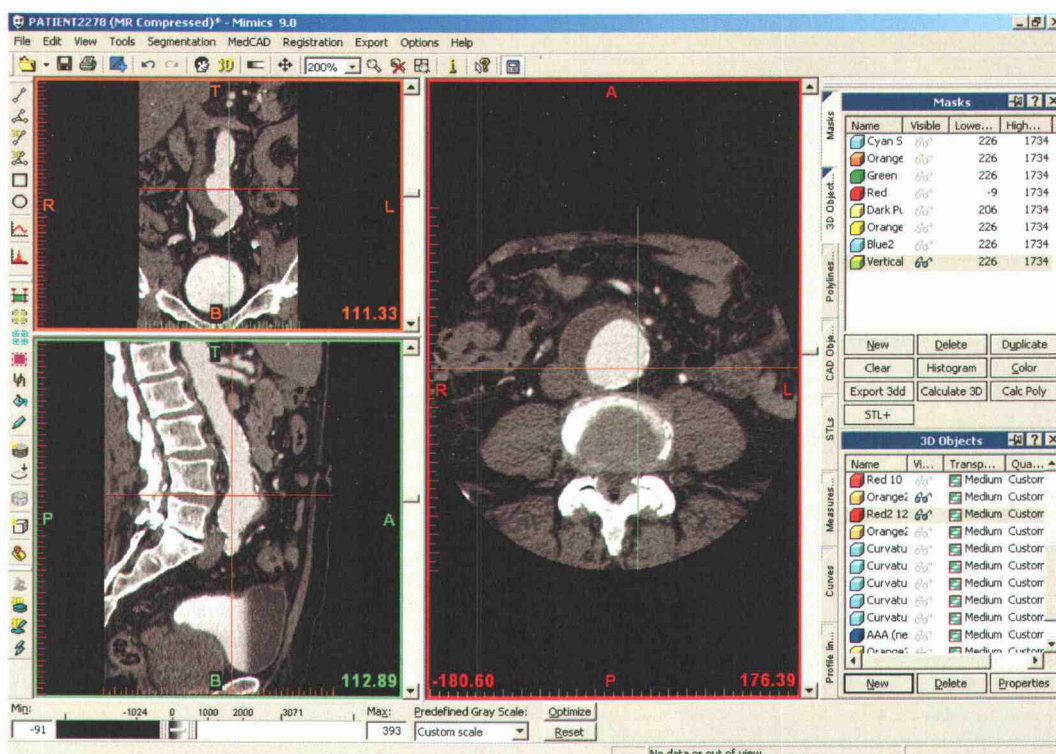


Fig 3.3 Patient CT image as displayed in *MIMICS*. Gray scale was adjusted prior to application of masks.

Segmentation masks for the aortic lumen were then constructed by highlighting areas of interest within each image. Since the lumen was very bright, it was necessary to pick a high threshold value to minimize the number of branches off the aorta that were highlighted with this mask. Once the proper threshold was set, each individual image was edited so that the *region growing* function of *MIMICS* would produce a separated, free-standing 3D representation of the aorta. In each of the individual CT slices, all the unwanted parts of the mask

were erased while saving the highlighted lumen. When this segmentation mask was complete, the *cavity fill* tool was used to fill internal gaps of the selected mask and place it in a new mask (Fig. 3.4).

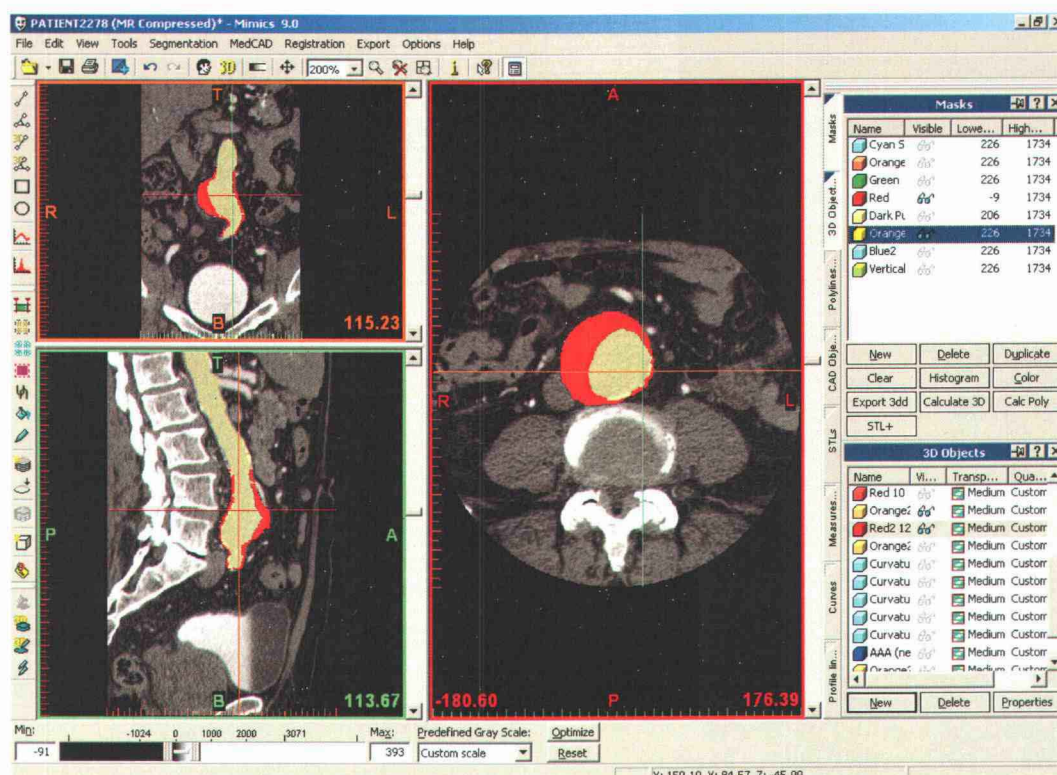


Fig 3.4 Patient CT image after applying growing region function. AAA lumen has been identified as a yellow mask and thrombus has been identified with Red.

3.1.4 Smoothing factors

Once the new mask had been created, its visualization parameters were adjusted for constructing a high quality 3D model from it. Three-dimensional generation parameters, including *quality*, *smoothing factors*, *triangle reduction* and *matrix reduction factors*, were chosen to make the smoothest and most accurate 3D model possible, by varying each of these parameters in turn. For each of the 35 patient series, between 30 and 45 test models were constructed and compared to find the smoothest model (Fig. 3.5). Ultimately, *smoothing factor ratios* were set to 1 to minimize the number of outlier points used in creating images. Also the number of triangle formation iterations needed to be maximized to eliminate the

noise present in the models. For these models, *edge-type* triangles were utilized, as the edge algorithm generates less noise than other algorithms on the resulting surface. For the triangle reduction parameters, a tolerance of 0.010 mm was selected as the maximum deviation that a related triangle may have to be part of the same plane that contains the selected triangles. The number of iterations for triangle reduction was set at 2. The last triangle reduction parameter is the *edge angle* value. An angle of 27° was chosen to accurately recreate model surfaces, while grouping any triangles less than this angle into the plane of other triangles (Fig. 3.6).

The last three-dimensional generation parameter is the *matrix reduction*, which determines how many voxels should be grouped in the XY plane and Z-direction. It was set from 4 to 7 and from 1 to 5 for XY and Z resolution respectively, depending on the CT scan quality or chosen threshold ranges (Fig. 3.5).

These parameters set the visualization quality of the models. Therefore the higher the quality, the more time the program needs to calculate the 3D images and the more memory is needed to load the 3D images afterwards. In this case, choosing the best parameters is not only a software issue but also a hardware issue.

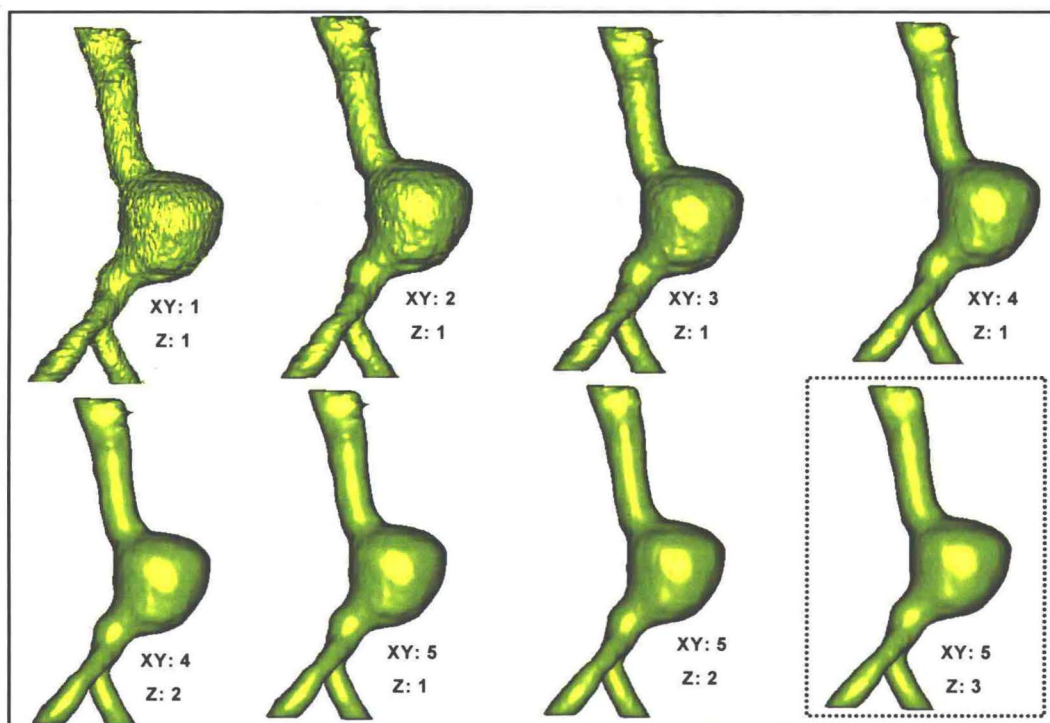


Figure 3.5 The Smoothing process: For each of the 35 patient series, between 30 to 45 test models were constructed and compared. The XY and Z stand for XY and Z resolution respectively. The model in the rectangle is the smoothest model of patient 1, and was used for geometric measurement.

3D Generation Parameters	3D	Patient 1
	AAA Volume [cm ³]	127.02
	Volume [cm ³]	197.23
	Surface [cm ²]	269.37
	# Triangles	14224
	# Points	7114
	Quality	C
	Smooth Factor	1
	Iterations (Smoothing)	5
	Tolerance [mm]	0.010
	Edge Angle [deg]	27.00
	Iterations (Triangle Reduction)	2
	Method: (Triangle Reduction)	
	a-Point based	
	b-Edge based	b
	Largest Shells (Shell Reduction)	-
	Matrix Reduction:	
	XY resolution	5
	Z resolution	3
	Working buffer size (MB)	631

Smoothest Model

Figure 3.6 3D Generation Parameters of the smoothest model which was constructed from AAA of patient 1.

3.1.5 Creating 3D Models of AAAs

For purposes of calculating AAA length and volume, the bulge top and bottom were defined as follows (Fig. 3.7):

- *Top Slice:* The level at which bulge diameter becomes 1.2 as large as the non-dilated diameter, and remains larger.
- *Bottom Slice:* The level at which bulge diameter becomes less than 1.2 as large as the non-dilated diameter, and remains less, or in cases with significant measurable thrombus, the level of the aortic bifurcation.

Table 3.1 contains the top, D_t , and bottom, D_b , diameters of all the AAAs and their corresponding slice coordinates. For each model, the ratios of the top and bottom diameters to its non-dilated diameter were also listed. For cases with significant thrombus up to their aortic bifurcation level, D_b are shown as BIF.

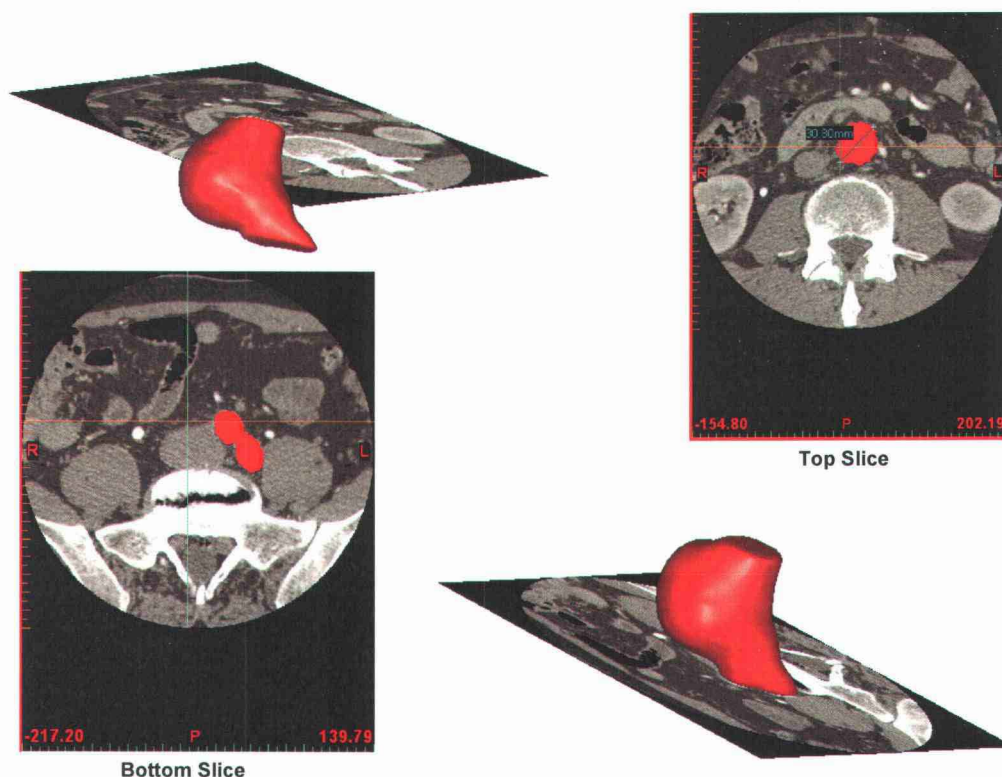


Figure 3.7 Top and Bottom slices representation of bulge for patient 5.

Bulge Definition

<i>Model</i>	<i>Top Slice Coordinate</i>	D_t (cm)	<i>Bottom Slice Coordinate</i>	D_b (cm)	d	D_t/d	D_b/d
1	-104.75	2.71	-173.5	2.85	2.32	1.17	1.23
2	-214.8	2.87	-283.8	BIF	2.35	1.22	*
3	-177.19	3.12	-257.19	BIF	2.72	1.15	*
4	-147.11	3.42	-227.11	BIF	2.84	1.2	*
5	-154.8	3.08	-217.2	BIF	2.68	1.15	*
6	-87	2.71	-193	BIF	2.26	1.2	*
7	-100.5	3.4	-150.5	3.69	2.96	1.15	1.25
8	-121	2.8	-210	BIF	2.25	1.24	*
9	-115.5	2.59	-190.5	BIF	2.11	1.23	*
10	-340.44	2.72	-434.81	BIF	2.32	1.17	*
11	-150	2.78	-257	BIF	2.42	1.15	*
12	-203.5	3.22	-293.5	BIF	2.7	1.19	*
13	-188.16	2.86	-257.16	BIF	2.48	1.15	*
14	-27.76	3.02	-159.76	3.09	2.57	1.18	1.2
15	-150	2.77	-221.4	2.65	2.25	1.23	1.18
16	-133.4	3.17	-202.4	BIF	2.76	1.15	*
17	-157.16	2.52	-218.36	BIF	2.2	1.15	*
18	-136.63	2.3	-224.83	BIF	2	1.15	*
19	-171.58	3.3	-227.98	3.11	2.66	1.24	1.17
20	-167.64	2.99	-223.44	3.06	2.58	1.16	1.19
21	-89.57	2.84	-201.17	BIF	2.39	1.19	*
22	-110.12	2.93	-194.12	BIF	2.55	1.15	*
23	-184.56	3.3	-272.16	BIF	2.77	1.19	*
24	-78	2.66	-192	2.78	2.23	1.19	1.25
25	-26.52	3.04	-118.32	BIF	2.54	1.2	*
26	-67.18	3.26	-154.18	BIF	2.75	1.19	*
27	-127.4	3.22	-203.6	3.33	2.74	1.18	1.22
28	-161.6	2.69	-248	BIF	2.17	1.24	*
29	-88.87	2.41	-163.87	2.51	2.01	1.2	1.24
30	-137.12	2.86	-234.32	BIF	2.3	1.24	*
31	-160.15	2.75	-260.35	2.84	2.29	1.2	1.24
32	-155.98	2.95	-208.18	BIF	2.57	1.15	*
33	-102.99	3.06	-180.39	BIF	2.66	1.15	*
34	117.2	2.61	15.8	BIF	2.22	1.17	*
35	52.4	3.29	-85	BIF	2.67	1.23	*

Table 3.1 Definition of Top and Bottom slices based on their coordinates and diameters. For each patient, diameter of top and bottom slices were 1.2 times larger than non-dilated diameter (d), except for models with significant thrombus volume, their bottom slices were defined as aortic bifurcation level (BIF).

After these parameters had all been selected, a 3D model of the lumen was calculated and saved for other geometric measurements.

Similarly, a three-dimensional model of thrombus was also created for those patients with measurable thrombus formation. For this purpose, a new thrombus mask was created following the same steps used to create the lumen mask (Fig. 3.2), but with a different threshold range since thrombus on the CT scans is not as bright as the lumen of the aorta. A 3D model of the thrombus could then be constructed using the same 3D generation parameters as the previously completed lumen model (Fig. 3.8).

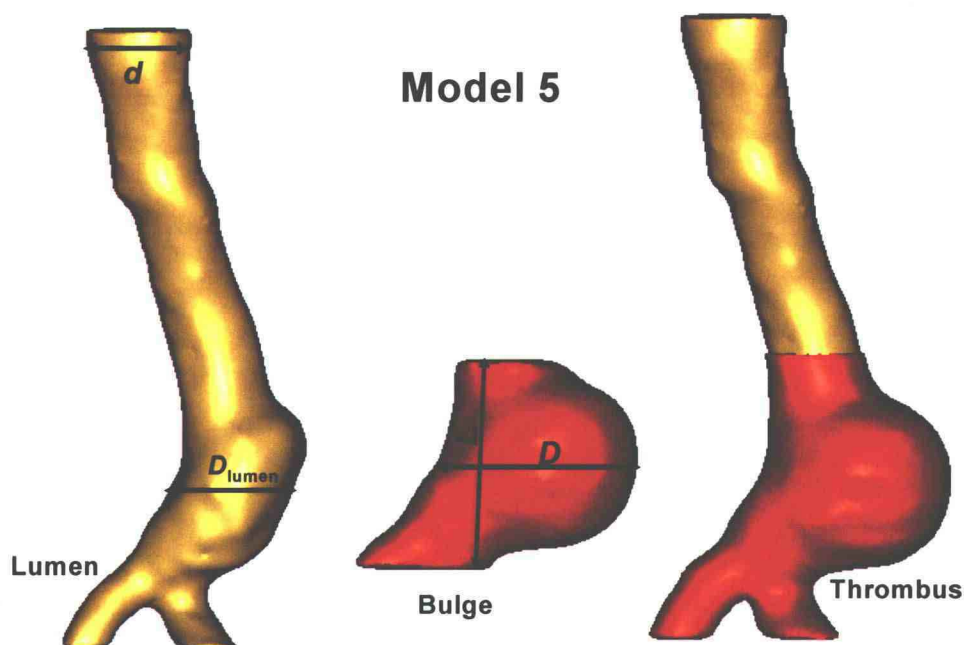


Figure 3.8 3-D reconstruction of one representative aneurysm with thrombus. The lumen is shown in yellow, with surrounding thrombus in red.

This new mask initially contained both the thrombus and lumen with no distinction between them. To calculate only the thrombus volume of bulge, the following simple equation was used to subtract off the mask containing only the lumen:

$$V_{AAA} = V_{lumen} + V_{thrombus} . \quad (3.1)$$

where V_{AAA} , V_{lumen} and $V_{thrombus}$ are the volume of the abdominal aortic aneurysm, the volume of the lumen and the volume of the thrombus respectively.

Once these parameters had all been selected, a 3D model of the lumen was calculated and saved in .dxf, .igs and .stl formats.

3.1.6 Geometric Parameters Measured by MIMICS

Many of the geometric properties of the completed 3D models could be evaluated using *MIMICS* tools. Maximum bulge diameter, aorta non-dilated diameter, maximum lumen diameter and AAA length were measured with a point-to-point measurement tool. For all AAA patients, these geometric parameters were defined as follows:

- *Maximum bulge diameter, D*: The largest bulge diameter which can be found at any axial slice between the top and bottom slices. For any model with no thrombus, *D* is as same as the largest lumen diameter, while for patient with thrombus, *D* is not equal to lumen diameter since it extended across deposited mural thrombus (Fig. 3.9).

Table 3.2 is a sample of diameter evaluation of model 28. In this table diameter of each bulge was shown with its corresponding axial slice coordinate (*Z coordinate*). Finally, the maximum diameter (*D*) was found by comparing this set of data.

- *Aorta non-dilated diameter, d*: The diameter of lumen corresponding to the last slice of L1 vertebra of Lumbar curve.

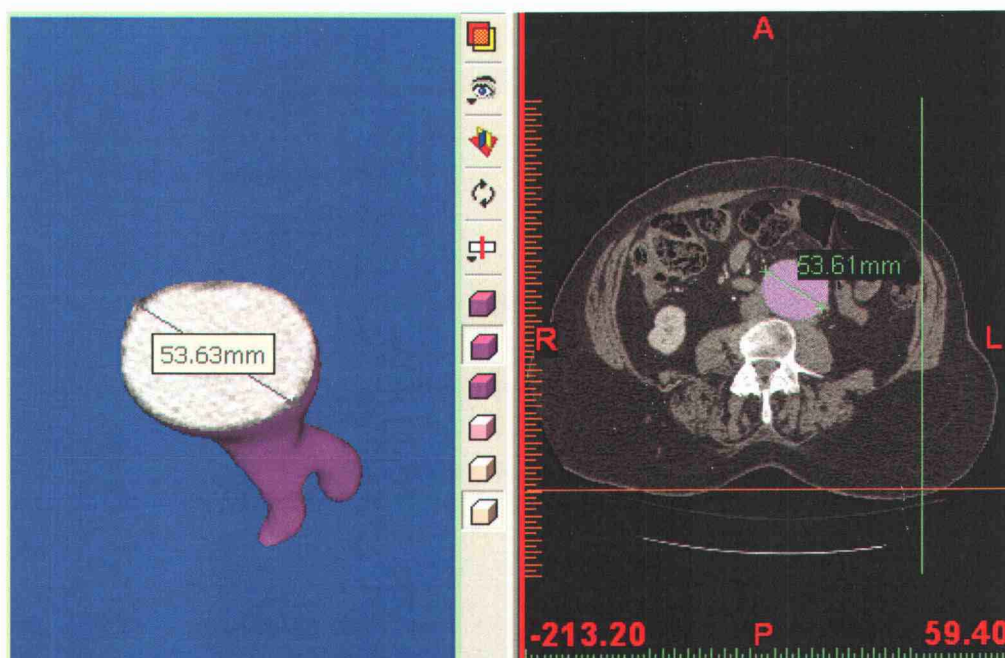


Figure 3.9 Maximum bulge diameter of model 28 was measured using point-to-point measurement tool: Cut view of a 3-D reconstruction of aneurysm bulge of model 28 with applied point-to-point tool was shown on the left. Axial representation of the slice with maximum diameter of the same model was represented on the right.

Diameter Evaluation of Model 28							
Slice Coordinate	-185.6	-186.2	-186.8	-187.4	-188.0	-188.6	-189.2
Diameter (mm)	37.2	37.2	35.9	36.4	37.2	37.8	38.0
Slice Coordinate	-189.8	-190.4	-191.0	-191.6	-192.2	-192.8	-193.4
Diameter (mm)	39.0	40.1	40.4	41.3	42.2	41.5	42.8
Slice Coordinate	-194.0	-194.6	-195.2	-195.8	-196.4	-197.0	-197.6
Diameter (mm)	43.1	42.8	42.3	43.8	42.6	44.0	43.7
Slice Coordinate	-198.2	-198.8	-199.4	-200.0	-200.6	-201.2	-201.8
Diameter (mm)	43.0	44.7	45.4	44.9	47.2	47.6	47.7
Slice Coordinate	-202.4	-203.0	-203.6	-204.2	-204.8	-205.4	-206.0
Diameter (mm)	48.8	48.6	49.7	50.2	49.4	50.2	50.6
Slice Coordinate	-206.6	-207.2	-207.8	-208.4	-209.0	-209.6	-210.2
Diameter (mm)	50.0	51.9	52.3	52.1	51.6	52.2	52.7
Slice Coordinate	-210.8	-211.4	-212.0	-212.6	-213.2	-213.8	-214.4
Diameter (mm)	51.8	52.4	51.9	52.5	53.6	53.2	52.1
Slice Coordinate	-215.0	-215.6	-216.2	-216.8	-217.4	-218.0	-218.6
Diameter (mm)	53.5	51.4	51.7	51.4	52.4	52.0	52.3
Slice Coordinate	-219.2	-219.8	-220.4	-221.0	-221.6	-222.2	-222.8
Diameter (mm)	52.4	51.3	52.8	52.8	52.0	53.1	53.4
Slice Coordinate	-223.4	-224.0	-224.6	-225.2	-225.8	-226.4	-227.0
Diameter (mm)	52.7	51.2	51.9	51.6	48.4	47.6	48.2

Table 3.2 Diameter evaluation of Model 28: For all AAA CT series, maximum diameters of each bulge slice were measured and compared. In this table diameter of each slice was shown with its corresponding axial coordinate (*Z coordinate*). Finally, the maximum diameter (*D*) was found by comparing this set of data. The maximum diameter in this model was highlight. It is equal to 53.63 mm at coordinate *Z*= -213.2.

- *Maximum lumen diameter, D_{Lumen}* : The diameter of lumen at the level of the maximum bulge diameter. For patients with thrombus this diameter was equal to *D* and for those without thrombus, it was always less than *D*.

- *AAA length, L*: The distance along the z-axis, between the top and bottom slices.

Volume calculations were performed with a volume measurement tool, using equation 1. These volume calculations also required adjustment of the model smoothing properties, as explained above. For all models, V_{AAA} , V_{lumen} and $V_{thrombus}$ was calculated and compared.

The lumenal index, LI , of each AAA was evaluated using surface measurement function which also required adjustment of the model smoothing factors, as explained in smoothing factor section. For this purpose, axial coordinate (Z coordinate) of the slice of the bulge with maximum diameter was entered as both *first and last slice positions* to limit surface area calculation to lumenal and AAA surface area of this slice (Fig. 3.10).

Lumenal Index could then be calculated using formula

$$LI = \frac{\text{Lumen Surface}}{\text{Bulge Surface}} \Big|_{\text{max bulge}} \quad (3.2)$$

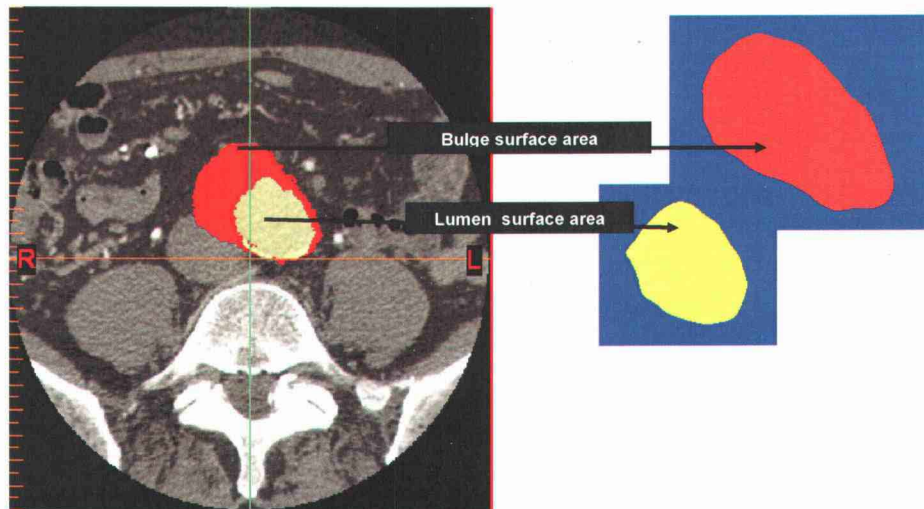


Figure 3.10 Lumenal Index calculation: For this purpose, axial coordinate (Z coordinate) of the slice of the bulge with maximum diameter was entered as both *first and last slice positions* to limit surface area calculation to lumenal and AAA surface area of this slice. In this figure the surface area of the bulge and lumen of model 5 were shown as a sample. The single slice representations of bulge and lumen surface area were presented at right. The axial representation of slice with maximum diameter was shown at left.

It is conceivable that geometrical shape, not just size may also be related to aneurysm rupture potential. Therefore, aneurysm shape may also be a factor in deciding on treatment modalities. In this case, a method was developed to quantify the seemingly arbitrary three-dimensional geometry of the aneurysm sac. In this method, the surface area of each bulge was calculated through Mimics and then compared to the surface area of a perfect cylinder and spheres which were defined based on the geometrical parameters of the bulge. Finally, ratio of the bulge surface area to its corresponding cylinder and sphere areas were calculated to show its similarity to either of these shapes.

The *corresponding cylinder* of each bulge was defined as the cylinder with diameter equal to top slice diameter of the bulge and length equal to bulge length (L). However, the *corresponding sphere* was defined as a sphere with diameter equal to maximum bulge diameter (D).

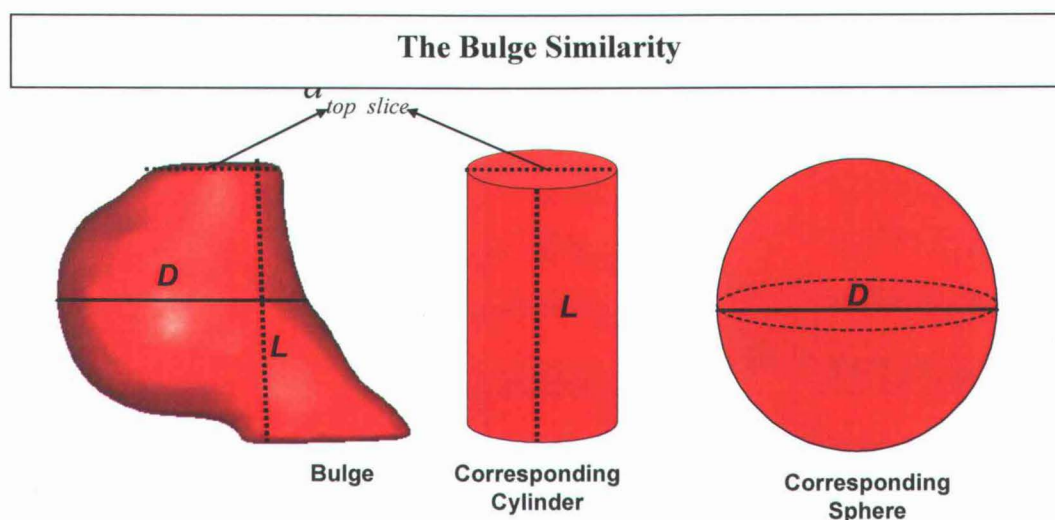


Figure 3.11 The bulge similarity: the *corresponding cylinder* of each bulge was defined as the cylinder with diameter equal to top slice diameter of the bulge and length equal to bulge length (L). However, the *corresponding sphere* was defined as a sphere with diameter equal to maximum bulge diameter (D). The ratios of surface area of each bulge to its corresponding cylinder and sphere surface areas were calculated and compared.

3.1.7 Geometric Parameters Measured by CFD-Geom

The tortuosity of each AAA was evaluated using a polyline representation of the models. For this purpose, iges files (.igs) were exported and opened in the program *CFD-GEOM* (CFD Research Inc.) (Fig. 3.12).

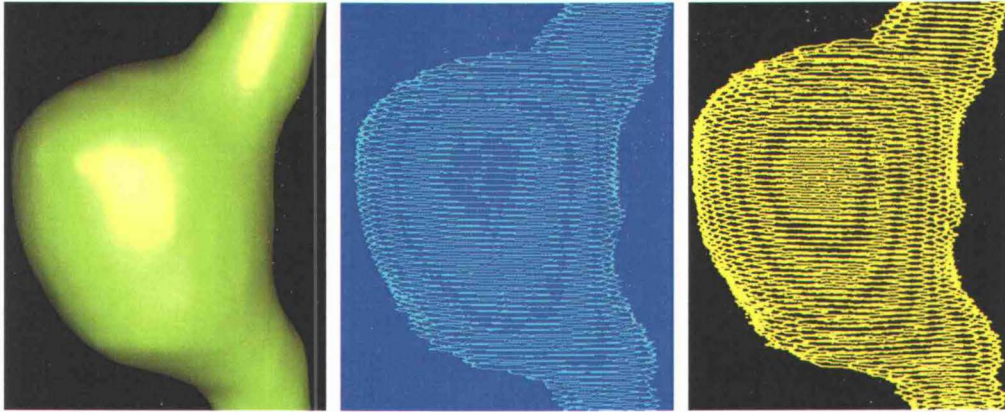


Figure 3.12 Polyline representation of the 3D model. From left to right: 3D reconstruction of AAA, polyline representation in *MIMICS* and its new format in *CFD-GEOM*.

Within *GEOM*, x , y , and z coordinates were assigned to the centerpoint of a series of polyline levels distributed at equal axial intervals along the lesion centerline, using a coordinate system with its z -direction oriented along the patient body axis. Tortuosity, τ , could then be calculated as

$$\tau = \sum S_n / L. \quad (3.3)$$

where S_n is the path length along the n centerpoints and L is the straight line distance between the first and last points. The distance S_n was calculated using the distance formula

$$S_n = \sqrt{(X_2 - X_1)^2 + (Y_2 - Y_1)^2 + (Z_2 - Z_1)^2}. \quad (3.4)$$

where (X_1, Y_1, Z_1) and (X_2, Y_2, Z_2) are the coordinates of any two of the n points. The number of layers or central points, n , varied from 30 to 50 in the different models to obtain an accurate analysis with minimal computations (Fig 3.13).

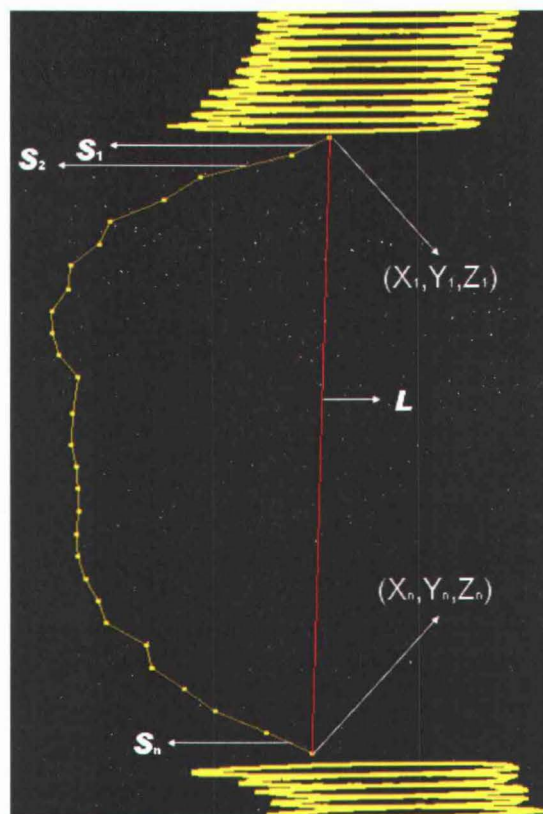


Figure 3.13 Tortuosity calculations through *CFD-GEOM*. The distance S_n is the path length along the n centerpoints and L is the straight line distance between the first and last points.

To calculate S_n , L and tortuosity, all the coordinates which had been obtained from Geom were imported to *Microsoft Excel*. A sample Excel worksheet model 24 is shown in figure 3.13. In this worksheet, X, Y and Z columns contain coordinates of each layer centerpoint; S_n column includes the distance between each two last points.

X	Y	Z	Sn	Sum(Sn)	L
186.764	-78.8991	202.657	6.532563127	187.997988	117.9257698
181.346	-81.384	205.33	7.866729944		
176.237	-83.8389	210.785	5.530481752		
172.251	-86.1218	213.865	3.904252923		
172.267	-88.4635	216.989	5.925999072		
169.647	-90.8845	221.721	4.437582161		
168.527	-93.3307	225.25	5.498593544		
166.723	-95.7221	229.861	2.699005254		
167.485	-98.1015	228.84	2.430931766		
167.131	-100.485	229.161	3.705016329		
167.887	-102.954	231.818	5.089476397		
168.147	-105.323	236.315	2.661401698		
167.64	-107.682	237.438	2.74846066		
166.636	-110.12	238.214	3.065385294		
166.079	-112.513	240.047	3.06814765		
164.724	-114.922	241.379	4.015755471		
163.992	-117.224	244.587	3.363815988		
162.916	-119.655	242.526	6.132415674		
162.955	-122.154	248.126	5.807376344		
161.827	-124.494	253.32	2.545525682		
161.623	-126.912	254.089	5.398557215		
161.155	-129.298	249.269	2.484179744		
161.565	-131.703	248.801	2.462676593		
160.997	-134.077	249.127	2.457039072		
161.193	-136.524	249.023	2.453203008		
161.355	-138.929	248.567	2.745837941		
160.038	-141.333	248.406	4.336696669		
162.039	-143.677	245.355	2.755484712		
162.853	-146.113	246.353	3.103315968		
161.753	-148.994	246.006	2.497377224		
162.663	-150.917	244.698	2.44187039		
162.35	-153.316	244.367	2.951600583		
163.321	-156.069	243.931	7.19899368		
159.638	-159.283	249.216	3.425191965		
157.478	-161.691	250.342	3.391385852		
155.971	-164.391	248.949	2.734223656		
155.852	-167.114	249.166	2.649547509		
155.307	-169.483	248.112	2.719061787		
155.469	-171.886	246.85	3.223226489		
155.62	-174.248	244.662	4.472755415		
155.634	-176.695	240.918	4.791666725		
156.149	-179.109	236.811	3.175034803		
155.311	-181.51	234.91	3.774494138		
155.593	-183.859	231.969	5.588037401		
155.917	-186.24	226.924	10.85662876		
153.533	-188.606	216.6	6.880983941		
151.311	-191.09	210.58		190 Polyline layers	48 Points

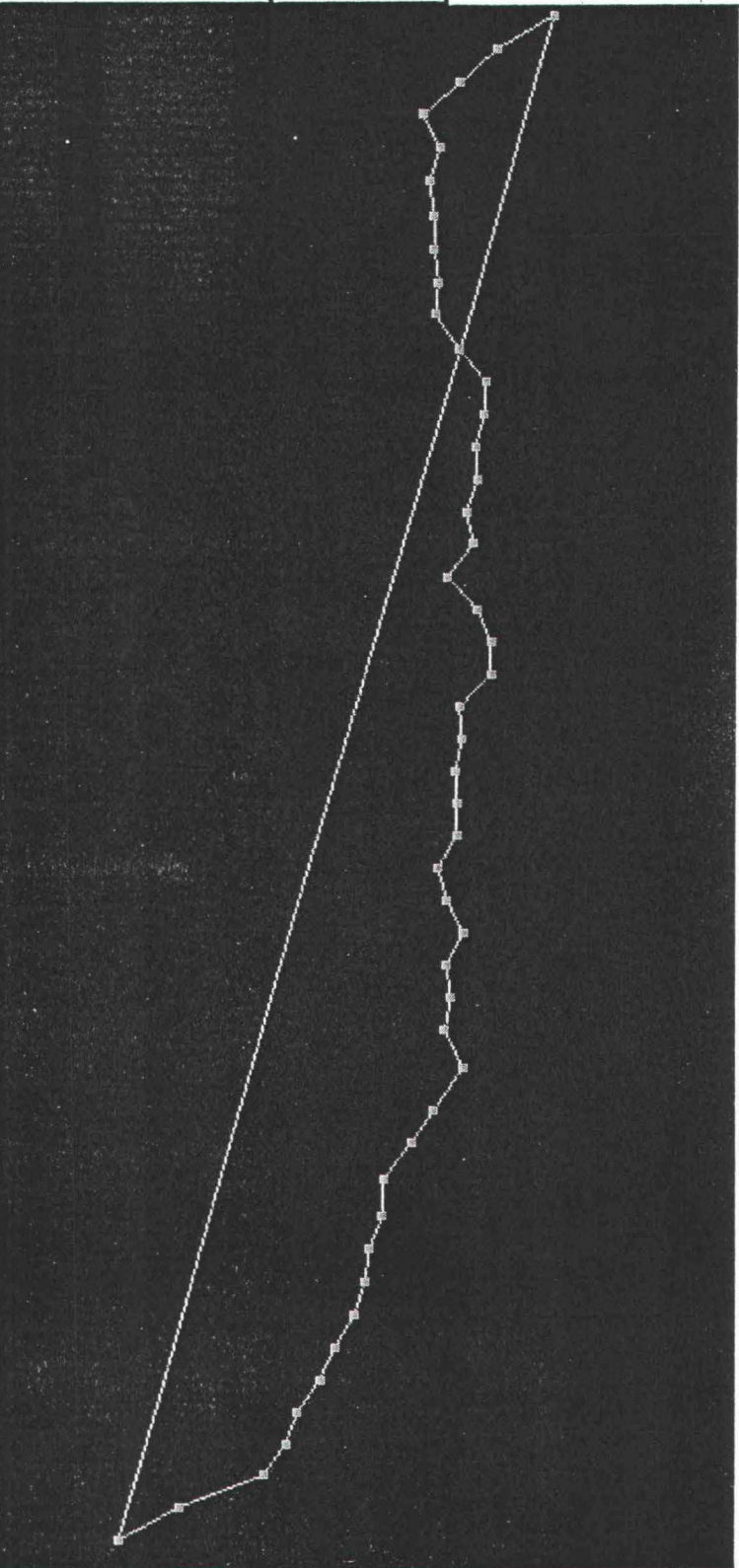


Figure 3.13 (b) Sample worksheet, for model 24: In this worksheet, X, Y and Z columns contain coordinates of each layer centerpoint; S_n column includes the distance between each two last points. These distances then were added up to use in the mentioned tortuosity formula.

The angular deviation, Θ , of the straight line L between the first and last center points of the bulge and the axial direction Z was also calculated in *GEOM*, using

$$\Theta = \text{Arc Cos } ((\Delta Y)/L) . \quad (3.5)$$

This parameter was used to show the deviation of the aneurysmal bulge from the body axis, which may be an important element in comparing and predicting the rupture risk of different AAAs.

3.1.8 Curvature Measurement by AutoCAD

Two different average curvatures for each AAA were evaluated, *vertical and horizontal curvatures*.

Overall vertical bulge curvature was evaluated using *AutoCAD* (Autodesk, Inc.), using the *.dxf* model representation file.

For each AAA, the vertical curvature was evaluated in 5 planes rotated through 7.5 degrees around the y-axis. To move through these slices, the 3D orbit command was used within *AutoCAD*. The 3D orbit display is controlled by several other commands and visual aids to make more accurate movement through the 3D possible. In this purpose a visual aid, *compass*, was applied. It draws a sphere within the 3D orbit which composed three major circle representing the X, Y, and Z axes. Each circle is divided to forty eight 7.5 degree parts (Fig. 3.15). To evaluate bulge vertical curvature in each slice, *arc tangent function* within *CAD* was applied. This tool fits to the edge of the 3 slices (top, bottom and maximum bulge diameter) on each AAA surface. Bulge curvature could then be calculated using following formula,

$$\text{Curvature} = 1/\rho. \quad (3.6)$$

where ρ is the radius of an arc tangent which was specified with three points on its circumference. The first point is the start point (1) which always was located on the

bulge top slice. The second point (2) is a point on the circumference of the arc and it was used to adjust the arc circumference on the slice with largest diameter, D . The third point is the endpoint (3) which was located on the bulge bottom slice (Fig. 3.14.d).

Unfortunately, finding the exact slices on the complete *.dxf* model at the *AutoCAD* studio was not applicable since the model slices were not represented individually (Fig. 3.14.b). Therefore, a new mask which only contained those necessary three slices was reconstructed in *MIMICS* (Fig. 3.14.a). The *.dxf* model representation this new mask was opened in *AutoCAD* for measuring its average vertical curvature (Fig. 3.14.c and d).

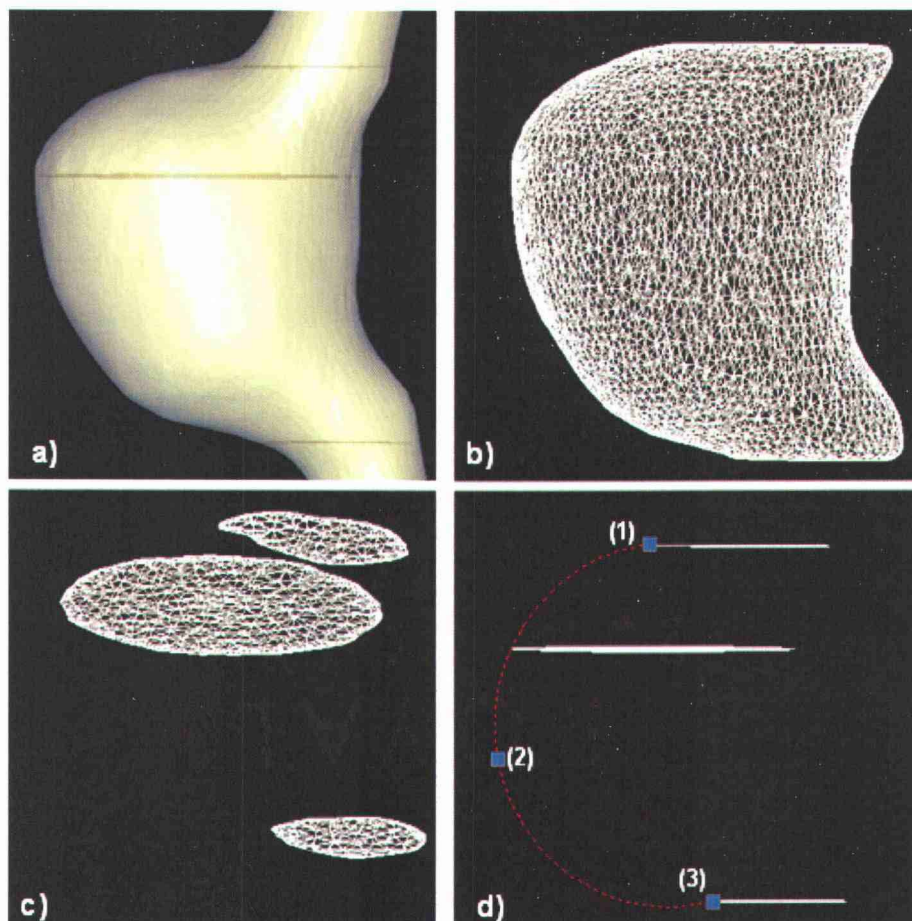


Figure 3.14 (a) Reconstructed three slices mask. (b) The *Auto-CAD* representation of AAA. The bulge slices could not be realized individually. (c) The *CAD* version of the new three slices mask, top, D , bottom slices. (d) An arc tangent command which is specified with three points. The first point is the start point (1) which always was located on the bulge top slice. The second point (2) is a point on the circumference of the arc and it was used to adjust the arc circumference on the slice with largest diameter, D . The third point is the endpoint (3) which was located on the bulge bottom slice.

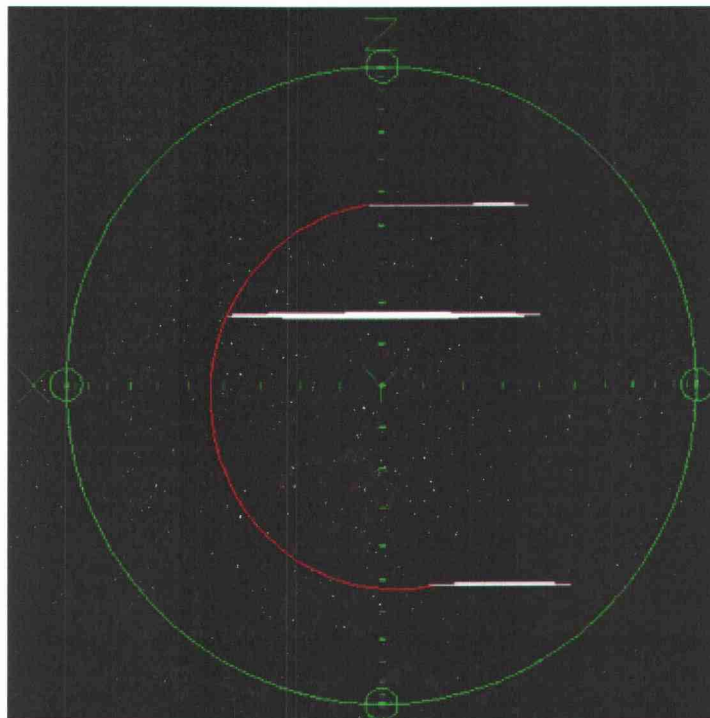


Figure 3.15 For each AAA, the vertical curvature was evaluated in 5 planes rotated through 7.5 degrees around the y-axis.

The horizontal curvature of each bulge was calculated via equation (7); however ρ (arc radius) was defined as:

$$\rho = D/2 \quad (3.7)$$

where D is the bulge diameter.

3.1.9 Statistical Analysis

All geometric parameters between two groups (patients with and without thrombus) were compared using the *statview* one-way ANOVA test approximation, while for comparing geometric parameters between four different group ages the *statview* Fisher's PLSD test was used. Any *p-value* less than 0.05 was considered significant throughout the study.

3.2 PRESSURE MEASUREMENTS

3.2.1 Flow loop configuration

Once satisfactory computational AAA models had been created, wall pressure magnitude and distribution were evaluated under steady flow conditions in three phantoms constructed from the models. These phantoms had been previously cast into flow through phantoms in the Peattie laboratory for a separate experiment [41]. For that purpose AAA computational representations in *.stl* format had been used to fabricate solid AAA replicas by stereolithography, and final phantoms constructed from the solid replicas through a series of casting steps. This produced a clear (Sylgard 184), rigid, flow-through replica of the AAA lumen that exactly duplicated the patient *in vivo* geometry [41]. Five 3mm holes were then drilled through the model wall and connected to pressure transducers (Ohmeda Inc., model DT-10, Fig. 3.16).

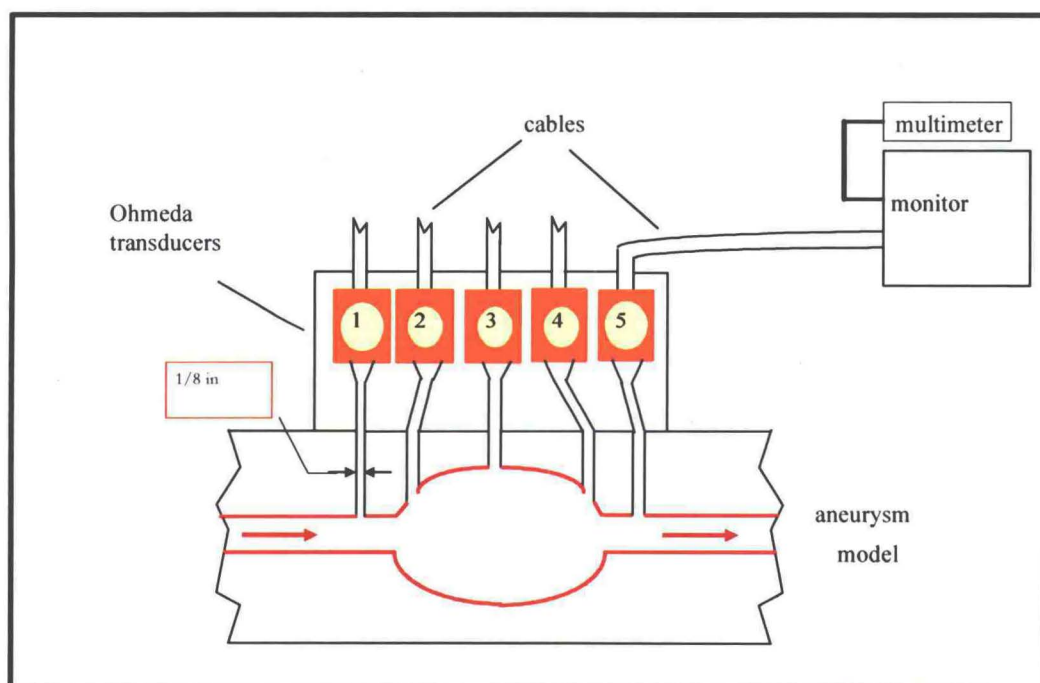


Figure 3.16 Location of the pressure taps within an aneurysm phantom. The taps are numbered 1 to 5 from the most proximal to the most distal.

One of these taps was located at the bulge center, and two were located at 2.2cm proximal to the entrance and 2.2 cm distal to the bulge exit. The final two were positioned equidistant from the center tap and the end taps.

These phantoms were incorporated into a gravity-driven flow loop simulating steady conditions in the human aorta (Fig. 3.17).

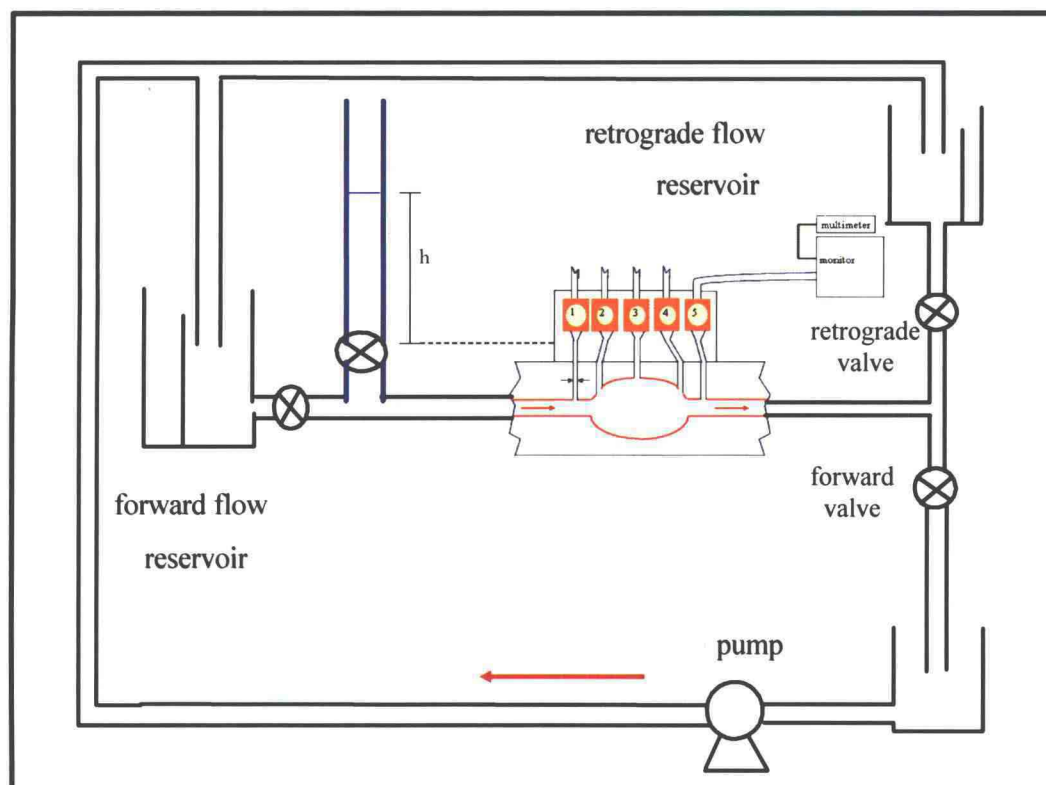


Figure 3.17 Flow loop used to deliver steady flow through the phantoms.

Flow in this loop is controlled through two electronic valves, the *retrograde* and *forward* valves, which dictate the flow direction and rate. One manual valve was also placed before a T connection for disconnecting the phantom from the flow reservoir and connecting it to a static water column. For steady flow conditions, only the retrograde valve was used, which was adjusted to regulate flow rates. A 1.5m- long section of rigid tubing with 2.54cm inner diameter was secured immediately proximal to the model and a similar length was placed distal to it, to provide straight entrance and exit regions, ensuring that flow entering the model was fully developed. The rigid tubing was fastened to the

model with silicone sealant such that its lumen was continuous with the model entrance.

The loop also included 4m of soft, flexible tubing, positioned downstream of the pump. The complete loop held about 25 L of fluid, including 2L in the reservoir which was located approximately 1.95m above the model and kept filled with the certain height of water during running. The working fluid of these experiments was tap water.

3.2.2 Transducer Calibration

Flow rate in the loop was determined via a timed collection method. Output signals from the pressure transducers were obtained from a dedicated monitor (Hewlett-Packard Inc., model 78532B), connected to a multimeter (Keithley Inc., model 175). Prior to beginning measurements, the pressure transducers were calibrated through application of a static water column of known height. Each pressure transducer was calibrated in the following manner: The stable flow loop was set by turning off all electronic devices including valves and pump. The free column which had been connected to the phantom by opening the manual valve was filled with varying heights of water. Voltages corresponding to the column height were recorded for each transducer. A calibration curve of voltage versus pressure ($\Delta P = \rho gh$) for each transducers was then plotted (Fig. 3.16). In all calibration plots, the voltage was found to be linearly related to the pressure, and a linear least-square regression was used to compute the best-fit line.

When the flow was then established, outputs from the multimeter were collected as voltages and converted to pressure based on these calibrations. Calibration curves are shown in section 4.2.a and Appendix D.

3.2.3 Flow rate Measurement and Reynolds Number

Wall pressure distributions in the three flow-through phantoms were evaluated at a series of flow rates producing Reynolds numbers of 500, 1000, 1500, 2000, 2500 and 3000. A time collection method was used to measure the rate of flow. For this purpose, the retrograde valve was adjusted to deliver flow rates

producing desired values of Reynolds number (where $Re = 4Q/\pi vd$, with Q the flow rate, d the undilated tube diameter, and ν the kinematic viscosity of the fluid). For each Reynolds number, output signals (voltages) were obtained and their corresponding pressures calculated.

Finally, a correction factor accounting for the vertical distance between the pressure transducers and the model wall was applied to the measurements. The vertical distance between the pressure sensor of each transducer and model wall was measured using a caliper needle. The corresponding pressure to this height was added to each pressure result ($\Delta P = \rho gh$). Correction factors for each transducer are shown in section 4.2.b.

CHAPTER 4: RESULTS

4.1 GEOMETRIC PARAMETERS

4.1.1 AAA Geometric Parameters

To evaluate AAA geometric parameters, computational models of real patient AAAs were constructed from abdominal CT series using specific software (*MIMICS*, Materialise Inc.).

Figure 4.1, shows 4 representative examples of 3D reconstructions from the 35 AAA patients. The remainder are shown in Appendix A. Patient AAAs can be categorized into two groups, those without thrombus and those presenting measurable thrombus deposits. In each case, the model lumen and thrombus when present are designated by different color shading. For the thrombosed models, separate images are shown of the thrombus distribution, AAA (bulge) and clear lumen, while for the unthrombosed models just the lumen and AAA (bulge) are shown.

Geometric Parameters of 35 patient-based models are presented in Table 4.2. Of these 35, only 6 showed no measurable thrombus. Of the 29 AAAs with thrombus, 26 were found to have thrombus deposits not only throughout the bulge, but also extending both proximally and distally away from the bulge (models 3, 15, 32, Fig. 4.1 and Appendix A).

Similarly, figure 4.2 and appendix B show the same AAA models in polyline (.igs) formats, which were exported and opened in the program *CFD-GEOM* to measure their bulge tortuosities. In this figure, the path length along the centerpoints is also shown for each bulge. In each *centerpoint path* model, the centerpoint of a series of polyline levels distributed at equal axial intervals along the lesion centerline was established, using a coordinate system with its z-direction oriented along the patient body axis. The coordinates (X , Y , Z) of each centerpoint which were obtained through *Geom* software then imported to an Excel worksheet for the tortuosity calculation.

3D representations of 35 AAA patients

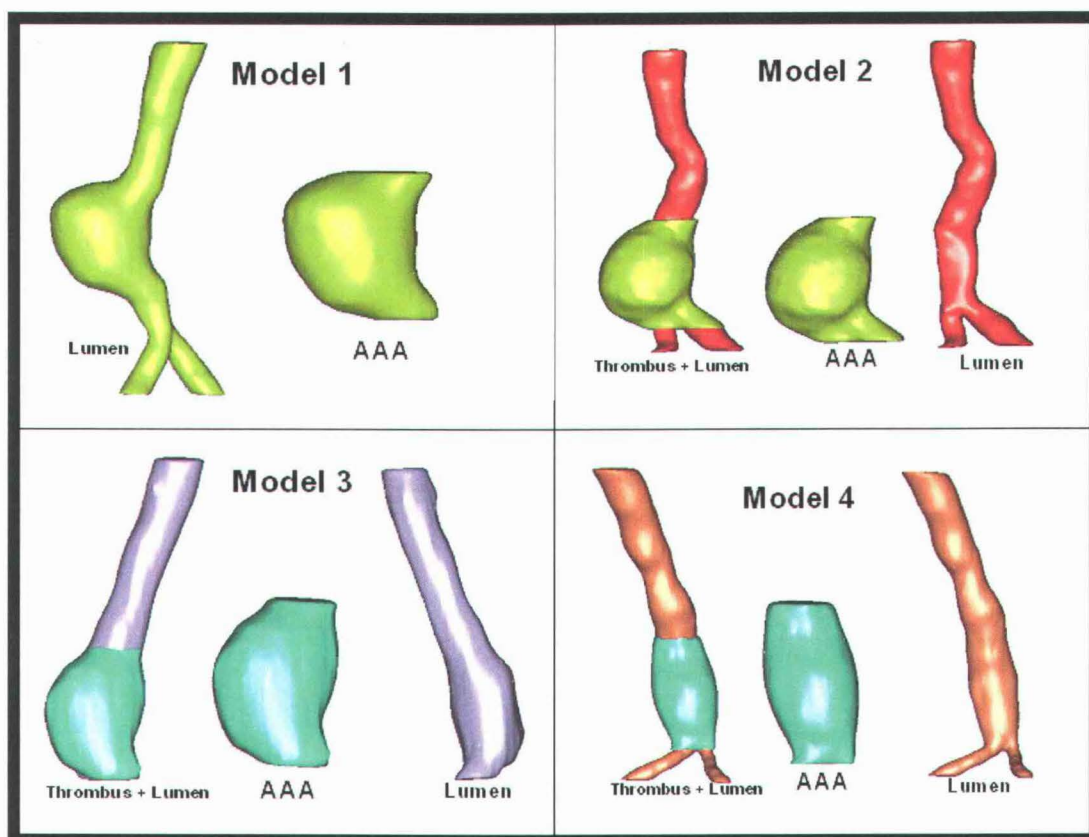


Figure 4.1 3-D representatives of models 1, 2, 3 and 4 AAA patients: In each case, the model lumen and thrombus when present, are designated by different color shading. For the thrombosed models, separate images are shown, the thrombus distribution, AAA (bulge) and clear lumen. For the unthrombosed models images are shown just lumen and AAA (bulge).

Polyline and Centerpoint path of 35 AAA patients

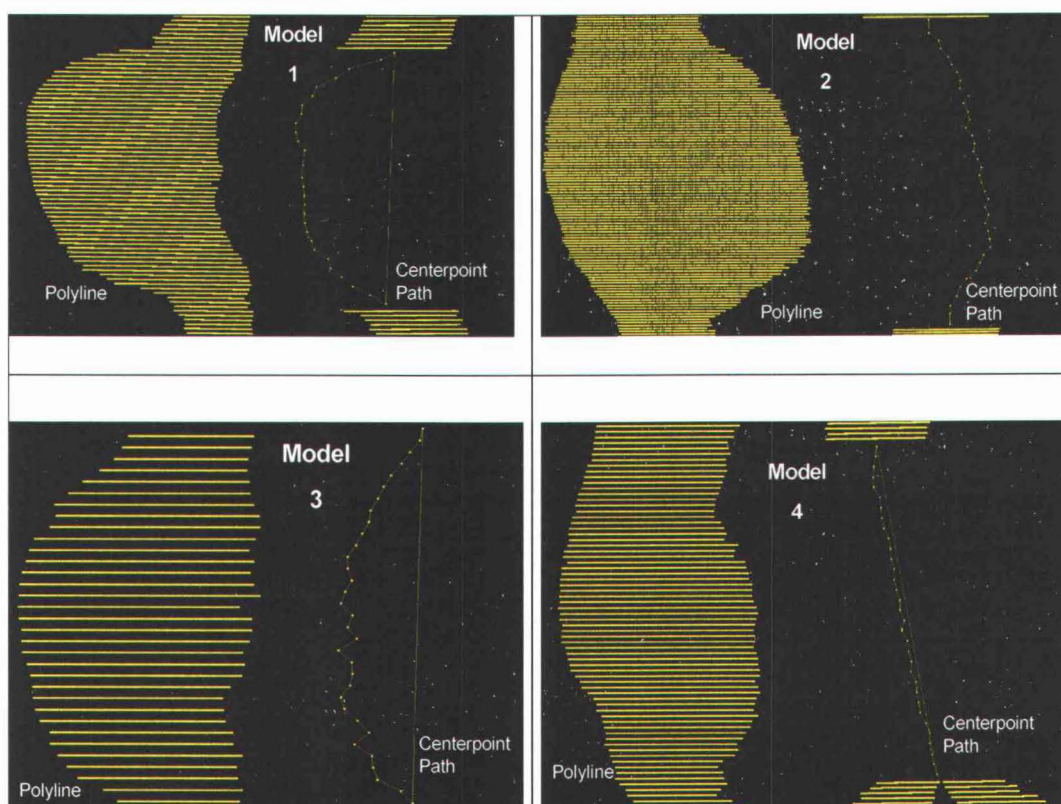


Figure 4.2 Model 1, 2, 3 and 4 of AAA patients in their polyline (.igs) formats: In this figure, the path length along the centerpoints was also shown for each bulge. In each centerpoint path model, the centerpoint of a series of polyline levels distributed at equal axial intervals along the lesion centerline, using a coordinate system with its z -direction oriented along the patient body axis.

One of the significant geometric parameters which was calculated through *MIMICS* software was the luminal index (*LI*) (Equ. 3.2). This parameter was determined for each AAA by measuring its luminal and bulge surface areas at the level of its maximum bulge diameter, then calculating their ratio. In figure 4.3 and appendix C, transverse cross-sections of all the AAAs at the level of maximum bulge diameter are presented. For the thrombosed models, the luminal surface areas always were separated from their thrombus layers with different color shadings.

All the measured transverse cross-sections areas of 35 patients at the levels of their maximum bulge diameters are listed in Table 4.1. In this table, two

measured parameters are shown for each AAA bulge: Luminal transverse cross-sections areas ranged from 3.66 cm^2 to 47.74 cm^2 with mean \pm S.D. equal to $19.87 \pm 12.75 \text{ cm}^2$. Bulge transverse cross-sections areas ranged from 7.73 cm^2 to 60.95 cm^2 with mean \pm S.D. equal to $36.80 \pm 11.50 \text{ cm}^2$. Obviously, for models without significant thrombus these two are the same and their *LI* are equal to one (model 1, 12, 18, 20, 27 and 28).

Axial cross-sections of AAA bulges at their maximum diameter

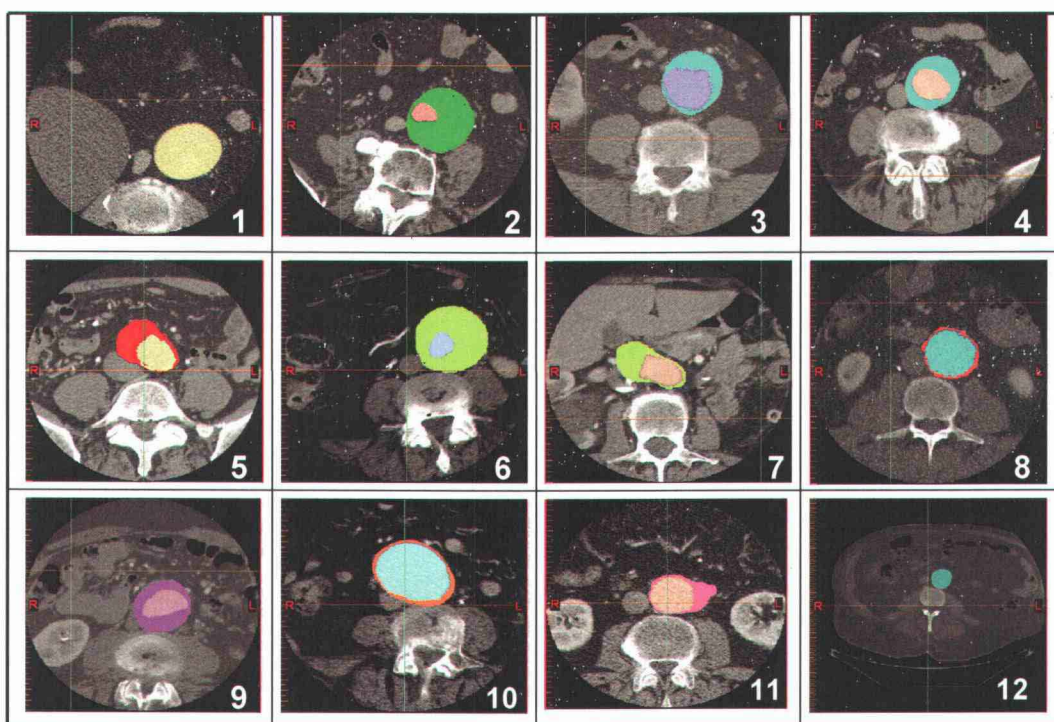


Figure 4.3 (a) Transverse cross- section of models 1 to 12 at their maximum diameter levels: At this level the surface area of lumen and bulge were calculated through *Mimics* surface area function to measure luminal index (*LI*) for all 35 patients (Appendix C).

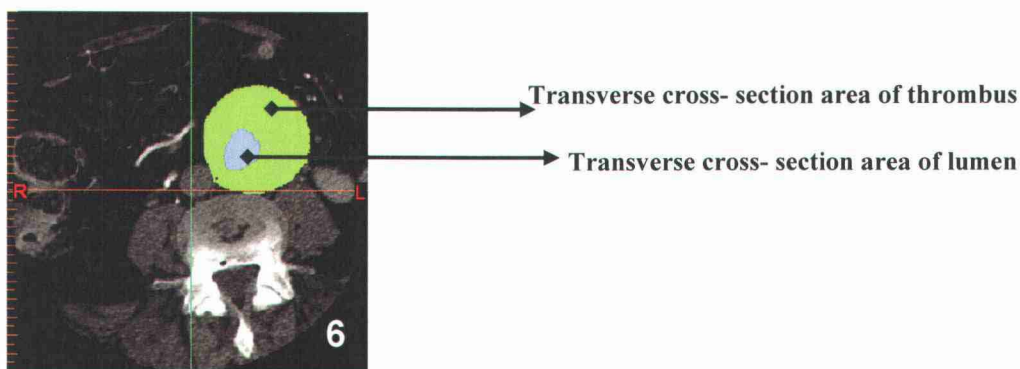


Figure 4.3 (b) Transverse cross- section areas of models 6 at its maximum diameter levels.

Luminal and Bulge Surface Areas of 35 AAA Patients

Model	1	2	3	4	5	6	7	8	9	10	11	12
Area of Lumen (cm ²)	44.26	4.67	23.92	12.76	13.57	4.92	11.20	24.32	11.52	47.74	17.80	27.78
Area of Bulge (cm ²)	44.26	47.77	43.23	34.21	30.09	51.40	26.49	30.61	32.52	59.35	28.53	27.78

Model	13	14	15	16	17	18	19	20	21	22	23	24
Area of Lumen (cm ²)	29.70	7.85	21.42	20.31	5.13	7.73	25.51	28.51	50.02	6.39	14.69	13.13
Area of Bulge (cm ²)	39.63	30.81	47.57	27.96	25.10	7.73	36.96	28.51	60.95	56.97	30.57	36.01

Model	25	26	27	28	29	30	31	32	33	34	35	Mean
Area of Lumen (cm ²)	9.15	10.84	45.19	34.22	18.52	3.66	29.69	23.29	12.96	16.51	16.49	19.87 ± 12.75
Area of Bulge (cm ²)	33.08	36.10	45.19	34.22	33.12	30.85	40.07	34.99	23.00	59.46	32.81	36.80 ± 11.50

Table 4.1 Measured surface areas of lumen and bulge (lumen+ thrombus) of each AAA patient at its maximum bulge diameter level: These parameters were calculated through *Mimics* surface area function for determining the luminal index (LI) of each bulge. This parameter was listed in table 4.2 as one of the AAA geometric parameters for each bulge. The maximum and minimum values are highlighted as red and blue font color.

Table 4.2 presents maximum bulge diameters, non-dilated diameters, ratio of maximum diameters to their non-dilated diameter, lumen diameters at the maximum bulge levels, bulge lengths, lumen volumes, thrombus volumes if present, AAA volumes, luminal indexes, tortuosities and angular deviations of bulges, AAA horizontal and vertical curvatures for each model. The maximum, minimum and mean \pm S.D. of each parameter are also listed in this table.

The maximum bulge diameter of the models, D , which are shown in column 1, ranged from 3.14 cm to 7.70 cm with a mean 5.67 ± 0.835 cm. Simultaneously, the aorta non-dilated diameter, d , are listed in column 2, varied from 2.00 cm to 2.96 cm with a mean 2.47 ± 0.250 cm. Consequently, the diameter ratio D/d for these patients, column 3, varied between 1.57 and 3.47 with a mean \pm S.D. equal to 2.30 ± 0.430 .

The lumen diameter at the level of maximum bulge diameter of the models, D_{Lumen} , is shown in column 4. This parameter ranged from 2.09 cm to 6.28 cm, mean \pm S.D. equal to 3.95 ± 1.086 cm. This is less on average than the bulge diameter, since only for the 6 patients lacking thrombus is D_{lumen} equal to D . By definition, for the 29 patients with thrombus formation D_{lumen} is less than D . Lesion lengths ranged from 4.83 cm to 13.50 cm, with a mean \pm S.D. of 8.42 ± 2.145 cm.

Columns 6, 7 and 8 present the results of volume calculations, V_{lumen} , $V_{thrombus}$ and V_{AAA} , respectively. V_{lumen} , the total volume of the bulge lumen, had a minimum and maximum value of 26.67 cm^3 and 251.45 cm^3 respectively. $V_{thrombus}$, the thrombus volume, when present had a maximum value of 170.72 cm^3 . As a result, V_{AAA} (which equals $V_{lumen} + V_{thrombus}$) had a maximum value of 304.0 cm^3 .

Luminal Indexes, LI , of 35 models are listed in column 10. They ranged from 0.096 to 1, with mean and standard deviation of 0.555 ± 0.293 .

Tortuosities of the 35 models ranged from 1.05 to 2.920 with mean \pm S.D. of 1.37 ± 0.321 . Angular deviation was found to have a very wide range from 1.10 to 31.33 degrees with average \pm S.D. equal to 12.49 ± 7.104 .

The two final columns of table 4.2 present model curvatures, which include both horizontal and vertical curvatures. The horizontal curvature was

found to range from 0.260 cm^{-1} to 0.637 cm^{-1} . It had mean \pm S.D. value of $0.362 \pm 0.075 \text{ cm}^{-1}$. The vertical curvature of each AAA varied from 0.113 cm^{-1} to 0.390 cm^{-1} with mean \pm S.D. of $0.216 \pm 0.835 \text{ cm}^{-1}$.

AAA Geometric Parameters

	D (cm)	d (cm)	D/d	D_{Lumen} (cm)	L (cm)	V_{Lumen} (cm ³)	$V_{Thrombus}$ (cm ³)	V_{AAA} (cm ³)	LI	τ	θ (deg)	K_h (cm ⁻¹)	K_v (cm ⁻¹)
1	5.73	2.32	2.47	5.73	6.88	127.02	0	127.02	1.00	1.38	3.70	0.349	0.288
2	5.99	2.35	2.55	2.09	6.90	26.67	100.18	126.85	0.098	1.38	9.63	0.334	0.283
3	5.90	2.72	2.17	4.28	8.00	94.16	44.41	138.57	0.553	1.35	14.9	0.339	0.232
4	5.23	2.84	1.84	3.31	8.00	51.10	51.02	102.12	0.373	1.10	14.9	0.382	0.168
5	5.72	2.68	2.13	3.36	6.24	53.12	50.96	104.08	0.451	1.42	18.4	0.350	0.310
6	6.20	2.26	2.74	2.39	10.60	54.22	170.72	224.94	0.096	1.23	9.46	0.323	0.186
7	6.33	2.96	2.14	3.49	5.00	31.18	59.97	91.51	0.423	1.33	5.52	0.316	0.390
8	5.05	2.25	2.24	4.24	8.90	81.05	20.33	101.37	0.795	1.06	15.5	0.396	0.150
9	5.47	2.11	2.59	3.83	7.50	44.09	74.75	118.84	0.354	1.20	15.4	0.366	0.174
10	6.98	2.32	3.01	6.22	9.44	169.20	34.35	203.55	0.804	1.08	21.16	0.287	0.165
11	5.70	2.42	2.36	3.52	10.70	89.24	30.01	119.52	0.624	1.14	1.70	0.351	0.161
12	4.49	2.70	1.66	3.24	9.00	101.99	0	101.99	1.00	1.05	18.5	0.445	0.160
13	5.97	2.48	2.41	4.97	6.90	80.85	22.09	102.94	0.794	1.57	21.14	0.335	0.288
14	5.91	2.57	2.30	3.36	13.20	77.34	124.87	202.21	0.255	1.25	9.95	0.338	0.283
15	6.45	2.25	2.87	4.46	7.14	78.57	61.06	139.63	0.450	1.52	9.85	0.310	0.232
16	4.71	2.76	1.71	4.28	6.90	72.75	22.8	95.55	0.726	1.53	18.02	0.425	0.168
17	5.48	2.2	1.85	2.65	6.12	35.57	35.7	71.27	0.204	1.56	29.61	0.365	0.310
18	3.14	2.00	1.57	3.14	8.82	32.62	0	32.62	1.00	1.15	7.02	0.637	0.186
19	5.71	2.66	2.15	4.12	5.64	73.06	27.85	100.91	0.690	1.72	8.40	0.350	0.390
20	5.09	2.58	1.97	5.09	5.58	78.99	0	78.99	1.00	1.25	31.33	0.393	0.150
21	7.29	2.39	3.05	6.28	11.16	251.45	52.55	304.00	0.821	1.57	15.62	0.274	0.174
22	7.01	2.55	2.75	2.40	8.40	37.35	110.82	148.17	0.112	2.92	2.13	0.285	0.165

	D (cm)	d (cm)	D/d	D_{Lumen} (cm)	L (cm)	V_{Lumen} (cm ³)	$V_{Thrombus}$ (cm ³)	V_{AAA} (cm ³)	LI	τ	θ (deg)	K_h (cm ⁻¹)	K_v (cm ⁻¹)
23	5.48	2.77	1.98	3.85	8.76	78.05	39.44	117.49	0.481	1.27	1.10	0.365	0.161
24	5.82	2.23	2.61	3.51	11.40	117.07	92.7	209.77	0.365	1.59	17.95	0.344	0.160
25	5.46	2.54	2.15	3.15	9.18	45.36	87.44	132.80	0.277	1.21	17.31	0.366	0.178
26	5.46	2.75	1.98	3.50	8.70	69.47	53.36	122.83	0.300	1.25	11.91	0.366	0.202
27	6.00	2.74	2.19	6.00	7.62	144.99	0	144.99	1.00	1.19	9.92	0.333	0.244
28	5.36	2.17	2.47	5.36	8.64	114.45	0	114.45	1.00	1.40	5.46	0.373	0.232
29	5.49	2.01	2.73	3.99	7.50	54.79	36.01	90.803	0.559	1.33	16.69	0.364	0.258
30	5.17	2.30	2.25	2.30	9.72	41.82	80.67	122.49	0.119	1.19	11.03	0.387	0.139
31	5.48	2.29	2.39	4.54	10.02	94.80	31.81	126.61	0.741	1.18	6.34	0.365	0.172
32	5.70	2.57	2.22	4.32	5.22	61.49	21.61	83.10	0.666	1.62	10.21	0.351	0.375
33	4.70	2.66	1.77	3.60	7.74	67.96	41.29	109.25	0.563	1.30	7.00	0.426	0.113
34	7.70	2.22	3.47	4.0	10.14	94.02	128.12	222.14	0.278	1.31	8.26	0.260	0.157
35	4.96	2.67	1.87	3.49	13.74	112.08	64.15	176.23	0.503	1.28	12.22	0.403	0.139
MAX	7.70	2.96	3.47	6.28	13.74	251.45	170.72	304.00	1	2.920	31.33	0.637	0.390
MIN	3.14	2.00	1.57	2.09	5.00	26.67	0	32.62	0.096	1.05	1.10	0.260	0.113
Mean±S.D.	5.67 ± 0.835	2.47 ± 0.250	2.30 ± 0.430	3.95 ± 1.086	8.44 ± 2.09	81.08 ± 44.492	50.60 ± 41.301	131.70 ± 52.944	0.555 ± 0.293	1.37 ± 0.321	12.49 ± 7.104	0.362 ± 0.063	0.216 ± 0.075

Table 4.2 AAAGeometric Parameters of 35 patient-based models: This table contains maximum bulge diameter, non-dilated diameter, ratio of maximum diameter to non-dilated diameter, lumen diameter at the maximum bulge level, bulge length, lumen volume, thrombus volume if present, AAA volume, ratio of thrombus volume to total bulge volume, lumenal index, tortuosity and angular deviation of bulge, AAA horizontal and vertical curvature. The maximum and minimum values are highlighted in red and blue font colors in table respectively.

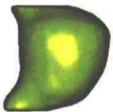
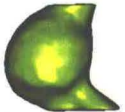


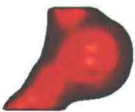

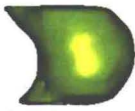


4.1.2 Bulge Surface Similarity of AAA




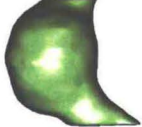

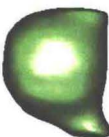

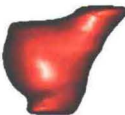

Aneurysm shapes were also evaluated to quantify the complex three-dimensional geometry of the aneurysm sac, since it is possible that geometrical shape, not just size may also be related to aneurysm rupture potential. Shape similarity parameters of the 35 patient-based models are presented in table 4.3 along with their bulge 3-D representation.

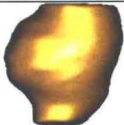




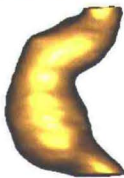




The bulge surface areas, S_b , which are shown in column 1, ranged from 68.23 cm^2 to 242.94 cm^2 with a mean \pm S.D. of $143.73 \pm 39.38 \text{ cm}^2$. Columns 2 and 3 present the results of corresponding cylinder and sphere surface area calculations, S_c and S_s . The corresponding cylinder surface area had maximum and minimum value of 139.53 cm^2 and 46.15 cm^2 , while it had mean and standard deviation of $77.11 \pm 20.95 \text{ cm}^2$. The corresponding sphere ranged from 30.98 cm^2 to 166.96 cm^2 with mean \pm S.D. of $103.01 \pm 29.79 \text{ cm}^2$.

To evaluate the bulge similarity of each AAA, the ratio of the bulge surface area, S_b , to S_c and S_s were calculated and listed in columns 4 and 5 respectively. The bulge similarity to cylinder, S_b/S_c , ranged from 1.08 to 2.74 while it had mean \pm standard deviation value of 1.90 ± 0.39 . The bulge similarity to sphere, S_b/S_s , had minimum and maximum value of 0.940 to 2.69 and mean \pm S.D. of 1.45 ± 0.39 .

Bulge Surface Similarity

Model	Surface of Bulge (S_b) (cm^2)	Surface of Cylinder(S_c) (cm^2)	Surface of Sphere (S_s) (cm^2)	$\frac{S_b}{S_c}$	$\frac{S_b}{S_s}$	3-D representation of Bulge
1	132.27	57.89	103.15	2.29	1.28	
2	136.69	61.40	112.72	2.23	1.21	
3	143.44	79.10	109.36	1.81	1.31	
4	117.78	86.17	85.93	1.37	1.37	
5	118.53	60.57	102.79	1.96	1.15	
6	201.54	89.56	120.76	2.25	1.67	
7	134.28	51.59	125.88	2.60	1.07	
8	119.61	77.41	80.12	1.55	1.49	
9	170.96	62.41	94.00	2.74	1.82	

10	184.05	88.02	153.06	2.09	1.20	
11	147.14	91.88	102.07	1.60	1.44	
12	124.63	102.07	63.34	1.22	1.97	
13	122.02	61.37	111.97	1.99	1.09	
14	209.93	125.24	109.73	1.68	1.91	
15	138.59	59.52	130.70	2.33	1.06	
16	111.09	69.02	69.69	1.61	1.59	
17	96.92	48.45	94.34	2.00	1.03	
18	68.23	63.44	30.98	1.08	2.20	

19	108.82	57.85	102.43	1.88	1.06	
20	98.82	48.47	81.39	2.04	1.21	
21	242.94	101.09	166.96	2.40	1.46	
22	154.72	76.22	154.38	2.030	1.002	
23	135.75	90.92	94.34	1.49	1.44	
24	218.10	95.77	106.41	2.28	2.05	
25	152.05	86.53	93.66	1.76	1.62	
26	132.97	89.82	93.66	1.48	1.42	
27	140.26	77.79	113.10	1.80	1.24	
28	134.20	71.58	90.26	1.87	1.49	




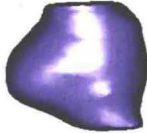



29	110.59	56.71	94.69	1.95	1.17	
30	139.64	85.72	83.97	1.63	1.66	
31	147.22	83.89	94.34	1.76	1.56	
32	96.88	46.15	102.07	2.10	0.949	
33	126.47	73.83	69.40	1.71	1.82	
34	205.93	81.83	186.27	2.52	1.11	
35	207.65	139.53	77.29	1.49	2.69	
MAX	242.94	139.53	166.96	2.60	2.69	
MIN	68.23	46.15	30.98	1.08	0.949	
Mean ± S.D.	143.73 ± 39.38	77.11 ± 20.95	103.01 ± 29.79	1.90 ± 0.39	1.45 ± 0.39	

Table 4.3 The bulge similarity table: this table includes the exact surface area of each AAA bulge, surface areas of its corresponding cylinder and sphere, 3D representation of each bulge maximum (red), mean \pm S.D. and minimum (blue) value of each parameter. The corresponding cylinder diameter and length was considered as same as the top slice diameter of the bulge (bulge entrance diameter) and bulge length (L). However, the corresponding sphere diameter was considered as same as maximum bulge diameter (D).

4.1.3 Age and AAA Geometric Parameters

Since age is one of the main risk factors in aneurysm ruptures, in this study, a method was developed to characterize AAA patients based on this factor.

Tables 4.4 to 4.8 were designed based on patient ages. In these tables, 28 AAA patients from 35 patients with some of their geometric parameters (table 4.2) were categorized in 4 different group ages. Age data for the other 7 patients were not available:

- Age group 1: patients with age ranged from 65 to 70 years old, (Table 4.4).
- Age group 2: patients with age ranged from 70 to 75 years old, (Table 4.5).
- Age group 3: patients with age ranged from 75 to 80 years old, (Table 4.6).
- Age group 4: patients with age above 80 years old, (Table 4.7).

The first age group contains 9 of 28 AAA patients (column 1). Their maximum bulge diameter ranged from 3.14 cm to 7.29 cm with mean \pm S.D. value of 5.33 ± 1.11 cm. The diameter ratio D/d for these patients, column 3, varied between 1.57 cm and 3.05 cm with a mean \pm S.D. equal to 2.25 ± 0.430 cm. Lesion lengths of this age group ranged from 6.8 cm to 13.50 cm, with a mean \pm S.D. of 9.09 ± 2.22 cm.

Columns 5 and 6 present V_{AAA} and $V_{thrombus}/V_{AAA}$ respectively. V_{AAA} in this group ranged from 32.62 cm^3 to 304 cm^3 , with mean \pm S.D. equal to $135.59 \pm 74.70 \text{ cm}^3$, while the ratio of $V_{thrombus}/V_{AAA}$, had minimum and maximum value of 0 (model with no measurable thrombus) and 0.659.

Lumenal Indexes, LI , listed in column 7, ranged from 0.119 to 1 with mean and standard deviation of 0.719 ± 0.292 .

Tortuosities of this group varied from 1.15 to 1.57 with mean \pm S.D. of 1.31 ± 0.156 .

Horizontal and vertical curvatures of this group age are also listed. The horizontal curvature was found to be in the range of 0.274 cm^{-1} to 0.637 cm^{-1} , while it had mean \pm S.D. value of $0.393 \pm 0.101 \text{ cm}^{-1}$. The vertical curvature of each AAA varied from 0.139 cm^{-1} to 0.288 cm^{-1} with mean \pm S.D. of $0.196 \pm 0.054 \text{ cm}^{-1}$.

Age group 1: 65 to 70 years old										
<i>Model</i>	<i>Age</i> (years)	<i>D</i> (cm)	<i>D/d</i>	<i>L</i> (cm)	<i>V_{AAA}</i> (cm ³)	<i>V_{Thrombus}</i> / <i>V_{AAA}</i>	<i>LI</i>	τ	<i>K_h</i> (cm ⁻¹)	<i>K_v</i> (cm ⁻¹)
21	65	7.29	3.05	11.16	304.00	0.173	0.821	1.57	0.274	0.174
30	65	5.17	2.25	9.72	122.49	0.659	0.119	1.19	0.387	0.139
27	66	6.00	2.19	7.62	144.99	0	1.00	1.19	0.333	0.244
31	68	5.48	2.39	10.02	126.61	0.251	0.741	1.18	0.365	0.172
16	69	4.71	1.71	6.90	95.55	0.239	0.726	1.53	0.425	0.168
29	69	5.49	2.73	7.50	90.803	0.397	0.559	1.33	0.364	0.258
1	70	5.73	2.47	6.88	127.02	0	1.00	1.38	0.349	0.288
18	70	3.14	1.57	8.82	32.62	0	1.00	1.15	0.637	0.186
35	70	4.96	1.87	13.74	176.23	0.364	0.503	1.28	0.403	0.139
MAX	70	7.29	3.05	13.74	304	0.659	1	1.57	0.637	0.288
MIN	65	3.14	1.57	6.88	32.62	0	0.119	1.15	0.274	0.139
Mean ± S.D.	68 ± 1.12	5.33 ± 1.11	2.25 ± 0.480	9.15 ± 2.28	135.59 ± 74.70	0.231 ± 0.221	0.719 ± 0.292	1.31 ± 0.156	0.393 ± 0.101	0.196 ± 0.054

Table 4.4 Age group 1: this group contains 9 of 28 AAA patients. This table presents following parameters for each patient: the patient age, maximum bulge diameter, D/d ratio, bulge length, AAA volume, ratio of thrombus volume to AAA volume, lumenal index, tortuosity, horizontal and vertical curvatures.

The second age group contains 5 of 28 AAA patients (column 1). Their maximum bulge diameter ranged from 4.7 cm to 5.9 cm with mean \pm S.D. value of 5.38 ± 0.433 cm. The diameter ratio *D/d* for these patients, column 3, varied between 1.77 cm and 2.47 cm with a mean \pm S.D. equal to 2.11 ± 0.258 cm. Lesion lengths of this age group ranged from 7.68 cm to 9.06 cm, with a mean \pm S.D. of 8.41 ± 0.549 cm.

Columns 5 and 6 present V_{AAA} and $V_{thrombus}/V_{AAA}$ respectively. V_{AAA} in this group ranged from 109.25 cm^3 to 138.57 cm^3 , with mean \pm S.D. equal to $122.51 \pm 12.55 \text{ cm}^3$, while the ratio of $V_{thrombus}/V_{AAA}$, had minimum and maximum value of 0 (model with no measurable thrombus) and 0.658.

Luminal Indexes, LI , listed in column 7, ranged from 0.277 to 1 with mean and standard deviation of 0.575 ± 0.264 .

Tortuosities of this group varied from 1.21 to 1.40 with mean \pm S.D. of 1.31 ± 0.073 .

Horizontal and vertical curvatures of this group age are also listed. The horizontal curvature was found in the range of 0.339 cm^{-1} to 0.426 cm^{-1} , while it had mean \pm S.D. value of $0.374 \pm 0.032 \text{ cm}^{-1}$. The vertical curvature of each AAA varied from 0.113 cm^{-1} to 0.232 cm^{-1} with mean \pm S.D. of $0.183 \pm 0.051 \text{ cm}^{-1}$.

Age Group 2: 70 to 75 years old

<i>Model</i>	<i>Age (years)</i>	<i>D (cm)</i>	<i>D/d</i>	<i>L (cm)</i>	<i>V_{AAA} (cm³)</i>	<i>V_{Thrombus}/V_{AAA}</i>	<i>LI</i>	<i>τ</i>	<i>K_h (cm⁻¹)</i>	<i>K_v (cm⁻¹)</i>
28	73	5.36	2.47	8.64	114.45	0	1.00	1.40	0.373	0.232
3	74	5.90	2.17	8.00	138.57	0.320	0.553	1.35	0.339	0.232
23	74	5.48	1.98	8.76	117.49	0.336	0.481	1.27	0.365	0.161
25	74	5.46	2.15	9.18	132.80	0.658	0.277	1.21	0.366	0.178
33	75	4.70	1.77	7.74	109.25	0.378	0.563	1.30	0.426	0.113
MAX	75	5.9	2.47	9.18	138.57	0.658	1	1.4	0.426	0.232
MIN	73	4.7	1.77	7.74	109.25	0	0.277	1.21	0.339	0.113
Mean \pm S.D.	74 \pm 0.707	5.38 \pm 0.433	2.11 \pm 0.258	8.46 \pm 0.585	122.51 \pm 12.55	0.338 \pm 0.234	0.575 \pm 0.264	1.31 \pm 0.073	0.374 \pm 0.32	0.183 \pm 0.051

Table 4.5 Age group 2: this group contains 5 of 28 AAA patients. This table presents following parameters for each patient: the patient age, maximum bulge diameter, D/d ratio, bulge length, AAA volume, ratio of thrombus volume to AAA volume, luminal index, tortuosity, horizontal and vertical curvatures.

The third age group contains 6 of 28 AAA patients (column 1). Their maximum bulge diameter ranged from 5.09 cm to 7.01 cm with mean \pm S.D. value of 5.75 ± 0.758 cm. The diameter ratio D/d for these patients, column 3, varied between 1.84 cm and 2.75 cm with a mean \pm S.D. equal to 2.19 ± 0.349 cm. Lesion lengths of this age group ranged from 4.98 cm to 8.28 cm, with a mean \pm S.D. of 6.40 ± 1.61 cm.

Columns 5 and 6 present V_{AAA} and $V_{thrombus}/V_{AAA}$ respectively. V_{AAA} in this group ranged from 78.99 cm^3 to 148.17 cm^3 , with mean \pm S.D. equal to $102.66 \pm 27.47 \text{ cm}^3$, while the ratio of $V_{thrombus}/V_{AAA}$, had minimum and maximum value of 0 (model with no measurable thrombus) and 0.748.

Luminal Indexes, LI , listed in column 7, ranged from 0.112 to 1 with mean and standard deviation of 0.568 ± 0.338 .

Tortuosities of this group varied from 1.10 to 2.92 with mean \pm S.D. of 1.72 ± 0.717 .

Horizontal and vertical curvatures of this age group were also listed. The horizontal curvature was found to be in the range of 0.285 cm^{-1} to 0.393 cm^{-1} , while it had mean \pm S.D. value of $0.352 \pm 0.042 \text{ cm}^{-1}$. The vertical curvature of each AAA varied from 0.150 cm^{-1} to 0.390 cm^{-1} with mean \pm S.D. of $0.250 \pm 0.122 \text{ cm}^{-1}$.

Age Group 3: 75 to 80 years old

<i>Model</i>	<i>Age</i> (years)	<i>D</i> (cm)	<i>D/d</i>	<i>L</i> (cm)	<i>V_{AAA}</i> (cm ³)	<i>V_{Thrombus} / V_{AAA}</i>	<i>LI</i>	<i>τ</i>	<i>K_h</i> (cm ⁻¹)	<i>K_v</i> (cm ⁻¹)
15	76	6.45	2.87	7.14	139.63	0.437	0.450	1.52	0.310	0.232
19	76	5.71	2.15	5.64	100.91	0.276	0.690	1.72	0.350	0.390
22	77	7.01	2.75	8.40	148.17	0.748	0.112	2.92	0.285	0.165
32	78	5.70	2.22	5.22	83.10	0.260	0.666	1.62	0.351	0.375
4	79	5.23	1.84	8.00	102.12	0.500	0.373	1.10	0.382	0.168
20	79	5.09	1.97	5.58	78.99	0	1.00	1.25	0.393	0.150
MAX	79	7.01	2.75	8.40	148.17	0.748	1	2.92	0.393	0.390
MIN	76	5.09	1.84	5.22	78.99	0	0.112	1.10	0.285	0.150
Mean ± S.D.	77.8 ± 1.30	5.75 ± 0.758	2.19 ± 0.349	6.57 ± 1.51	102.66 ± 27.47	0.357 ± 0.281	0.568 ± 0.338	1.72 ± 0.717	0.352 ± 0.042	0.250 ± 0.122

Table 4.6 Age group 3: this group contains 6 of 28 AAA patients. This table presents following parameters for each patient: the patient age, maximum bulge diameter, D/d ratio, bulge length, AAA volume, ratio of thrombus volume to AAA volume, luminal index, tortuosity, horizontal and vertical curvatures.

The fourth age group contains 8 of 28 AAA patients (column 1). Their maximum bulge diameter ranged from 5.46 cm to 7.7 cm with mean \pm S.D. value of 6.02 ± 0.770 cm. The diameter ratio D/d for these patients, column 3, varied between 1.85 cm and 3.47 cm with a mean \pm S.D. equal to 2.43 ± 0.541 cm. Lesion lengths of this age group ranged from 6.83 cm to 13.2 cm, with a mean \pm S.D. of 8.06 ± 2.07 cm.

Columns 5 and 6 present V_{AAA} and $V_{thrombus}/V_{AAA}$ respectively. V_{AAA} in this group ranged from 71.27 cm^3 to 222.14 cm^3 , with mean \pm S.D. equal to $137.13 \pm 56.88 \text{ cm}^3$, while the ratio of $V_{thrombus}/V_{AAA}$ had minimum, maximum and mean \pm S.D value of 0.215, 0.790 and 0.493 ± 0.173 .

Luminal Indexes, LI , listed in column 7, ranged from 0.098 to 0.794 with mean and standard deviation of 0.356 ± 0.224 .

Tortuosities of this group varied from 1.25 to 1.59 with mean \pm S.D. of 1.44 ± 0.136 .

Horizontal and vertical curvatures of this age group are also listed. The horizontal curvature was found to be in the range of 0.260 cm^{-1} to 0.366 cm^{-1} , while it had mean \pm S.D. value of $0.336 \pm 0.036 \text{ cm}^{-1}$. The vertical curvature of each AAA varied from 0.157 cm^{-1} to 0.310 cm^{-1} with mean \pm S.D. of $0.244 \pm 0.069 \text{ cm}^{-1}$.

Age Group 4: Above 80 years old

<i>Model</i>	<i>Age</i> (years)	<i>D</i> (cm)	<i>D/d</i>	<i>L</i> (cm)	<i>V</i> _{AAA} (cm ³)	<i>V</i> _{Thrombus} / <i>V</i> _{AAA}	<i>LI</i>	τ	<i>K</i> _h (cm ⁻¹)	<i>K</i> _v (cm ⁻¹)
17	81	5.48	1.85	6.12	71.27	0.500	0.204	1.56	0.365	0.310
26	82	5.46	1.98	8.70	122.83	0.434	0.300	1.25	0.366	0.202
5	83	5.72	2.13	6.24	104.08	0.490	0.451	1.42	0.350	0.310
24	83	5.82	2.61	11.40	209.77	0.442	0.365	1.59	0.344	0.160
34	83	7.70	3.47	10.14	222.14	0.577	0.278	1.310	0.260	0.157
2	85	5.99	2.55	6.90	126.85	0.790	0.098	1.38	0.334	0.283
13	86	5.97	2.41	6.90	102.94	0.215	0.794	1.57	0.335	0.288
14	87	5.91	2.30	13.20	202.21	0.618	0.255	1.25	0.338	0.283
MAX	87	7.7	3.47	13.2	222.14	0.79	0.794	1.59	0.366	0.31
MIN	81	5.46	1.85	6.12	71.27	0.215	0.098	1.25	0.26	0.157
Mean \pm S.D.	83.75 \pm 2.05	6.00 \pm 0.714	2.41 \pm 0.503	8.70 \pm 2.64	145.26 \pm 57.47	0.508 \pm 0.166	0.343 \pm 0.210	1.42 \pm 0.143	0.337 \pm 0.033	0.249 \pm 0.065

Table 4.7 Age group 4: this group contains 8 of 28 AAA patients. This table presents following parameters for each patient: the patient age, maximum bulge diameter, D/d ratio, bulge length, AAA volume, ratio of thrombus volume to AAA volume, luminal index, tortuosity, horizontal and vertical curvatures.

4.2 PRESSURE MEASUREMENT

4.2.a Calibration Curves

In this study, absolute wall pressure distributions, in mmHg, were measured in the three flow-through phantoms, models 7,8 and 11, with D/d ratio of 0.97, 1.80 and 1.50 respectively at a series of flow rates producing Reynolds numbers of 500, 1000, 1500, 2000, 2500 and 3000. From these data, pressure differences along various regions of the models were calculated.

The pressure transducers were calibrated through application of a static water column of known height. For each transducer, the voltages to its corresponding height were recorded (Table, 4.8, 4.9 and 4.10) and then the calibration curve of voltage versus pressure ($\Delta P = \rho gh$) was plotted.

In figures 4.4, 4.5, 4.6, calibration plots of transducer 1 for all the phantoms are plotted, along with the best-fit line computed by least squares regression. The equation for the best-fit line was used in all wall pressure distribution experiments to convert measured voltages into pressure. All other calibration plots (transducers 2, 3, 4 and 5 of each phantom are given in Appendix D.

Model 7: Calibration Table						
Height (inch)	P (mmHg)	Voltage 1 (v)	Voltage 2 (v)	Voltage 3 (v)	Voltage 4 (v)	Voltage 5 (v)
6	11.21	0.117	0.114	0.120	0.126	0.108
12	22.43	0.228	0.224	0.234	0.235	0.217
24	44.86	0.444	0.443	0.452	0.452	0.436
36	67.28	0.666	0.663	0.672	0.672	0.655
48	89.71	0.894	0.891	0.899	0.899	0.882
60	112.14	1.120	1.118	1.125	1.126	1.109
72	134.57	1.336	1.335	1.340	1.341	1.324

Table 4.8 Calibration table of model 7: All the five pressure transducers were calibrated through application of a static water column of known height. For each transducer, the voltages to its corresponding height were recorded and then the calibration curve of voltage versus pressure was plotted.

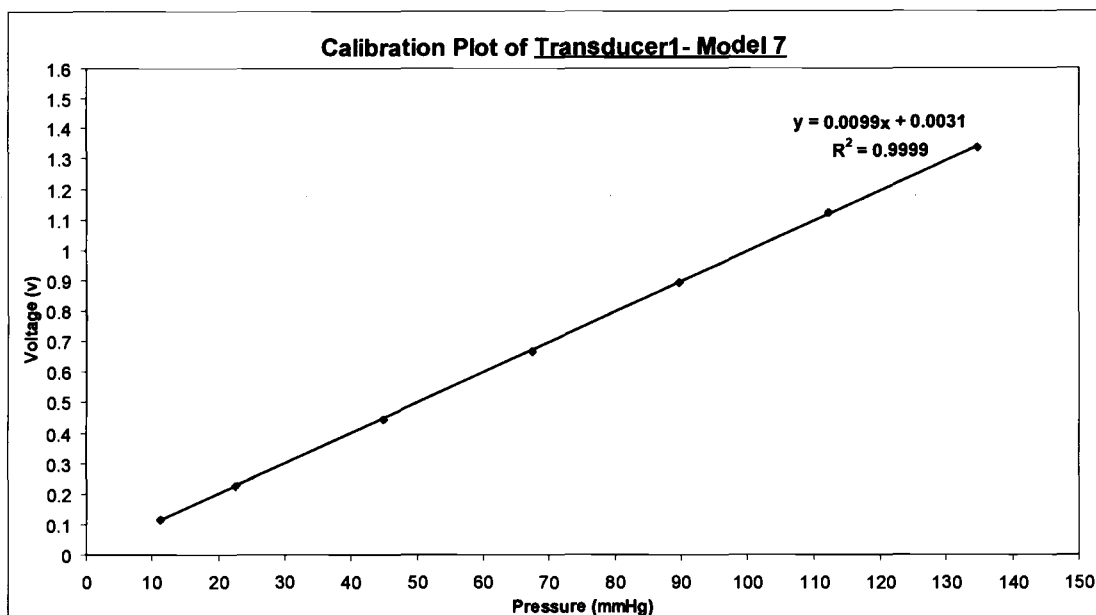


Figure 4.4 The Calibration curve of transducer 1 of the model 7. Measured voltages are plotted as symbol, along with the best fit line from linear least square regression.

Model 8: Calibration Table						
<i>Height</i> (inch)	<i>P</i> (mmHg)	<i>Voltage 1</i> (v)	<i>Voltage 2</i> (v)	<i>Voltage 3</i> (v)	<i>Voltage 4</i> (v)	<i>Voltage 5</i> (v)
13	24.30	0.248	0.225	0.250	0.247	0.237
29	54.20	0.523	0.523	0.547	0.542	0.533
39	72.89	0.730	0.730	0.731	0.726	0.718
45	84.10	0.845	0.823	0.847	0.841	0.833
50	93.45	0.929	0.909	0.933	0.927	0.919
60	112.14	1.120	1.099	1.122	1.115	1.109
74	138.30	1.375	1.375	1.379	1.371	1.361

Table 4.9 Calibration table of model 8: All the five pressure transducers were calibrated through application of a static water column of known height. For each transducer, the voltages to its corresponding height were recorded and then the calibration curve of voltage versus pressure was plotted.

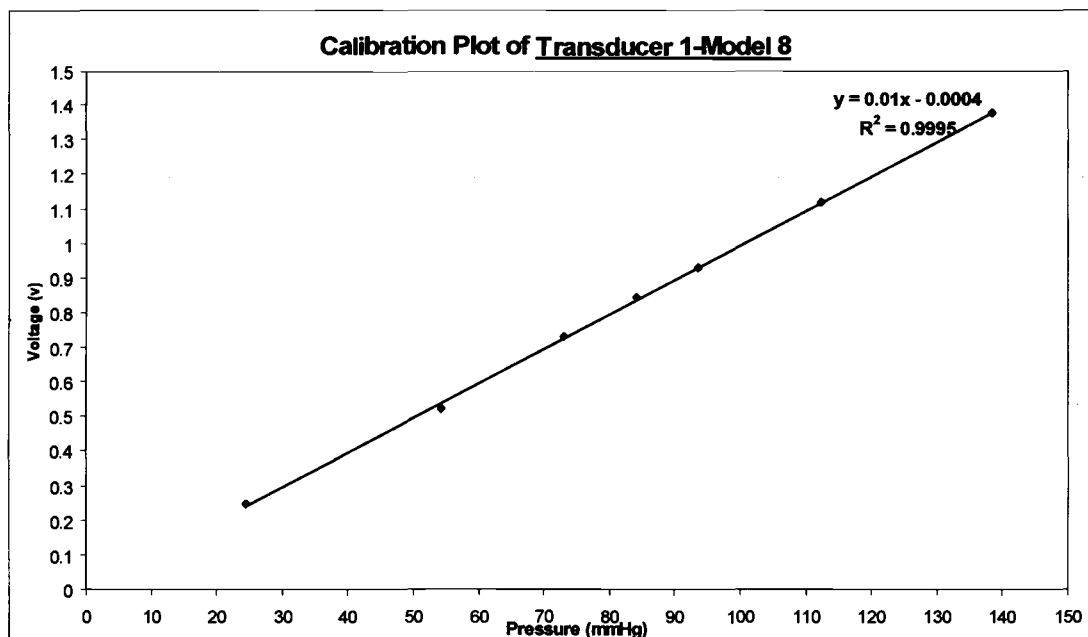


Figure 4.5 The Calibration curve of transducer 1 of the model 8. Measured voltages are plotted as symbol, along with the best fit line from linear least square regression.

Model 11: Calibration Table						
<i>Height</i> (inch)	<i>P</i> (mmHg)	<i>Voltage1</i> (v)	<i>Voltage2</i> (v)	<i>Voltage3</i> (v)	<i>Voltage4</i> (v)	<i>Voltage5</i> (v)
0	0	0.049	0.035	0.049	0.041	0.042
17	31.77	0.323	0.309	0.324	0.315	0.317
20	37.38	0.376	0.362	0.377	0.369	0.371
29	54.20	0.543	0.530	0.545	0.537	0.540
40	74.76	0.746	0.734	0.749	0.742	0.744
53	99.06	0.984	0.972	0.988	0.981	0.982
60	112.14	1.117	1.104	1.121	1.114	1.115
70	130.83	1.301	1.288	1.307	1.300	1.300

Table 4.10 Calibration table of model 11: All the five pressure transducers were calibrated through application of a static water column of known height. For each transducer, the voltages to its corresponding height were recorded and then the calibration curve of voltage versus pressure was plotted.

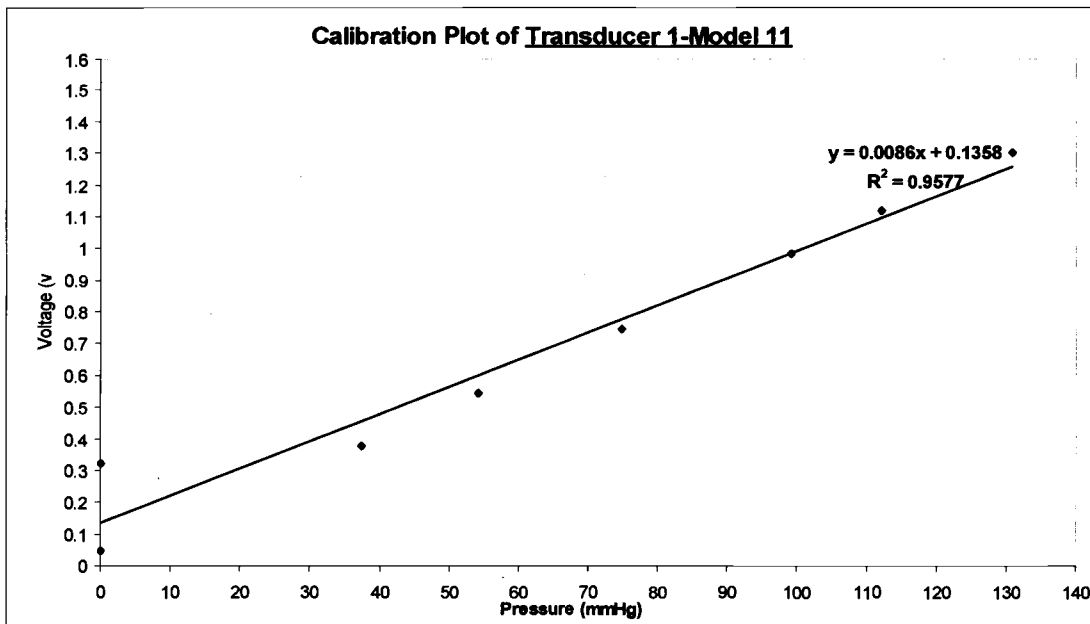


Figure 4.6 The Calibration curve of transducer 1 of the model 11. Measured voltages are plotted as symbol, along with the best fit line from linear least square regression.

4.2.2 Pressure Distribution Measurements

Calculated pressures for each Reynolds number ($Re = 4Q/\pi vd$) of model 7, 8 and 11 were shown in Appendix E respectively. A correction factor accounting for the vertical distance between the pressure transducers and the model wall, $H_{correction}$, was then applied to the results. In Tables 4.11, 4.13 and 4.15, H_1 is the vertical distance from sensor to the top of the model, while H_2 is the length of the holes inside the Model. $H_{correction}$ was then calculated from the formula,

$$H_{correction} = H_1 + H_2 \quad (4.1)$$

The corresponding pressure ($\rho g H_{correction}$) to this height was added to each pressure results (Tables, 4.12, 4.14, 4.16).

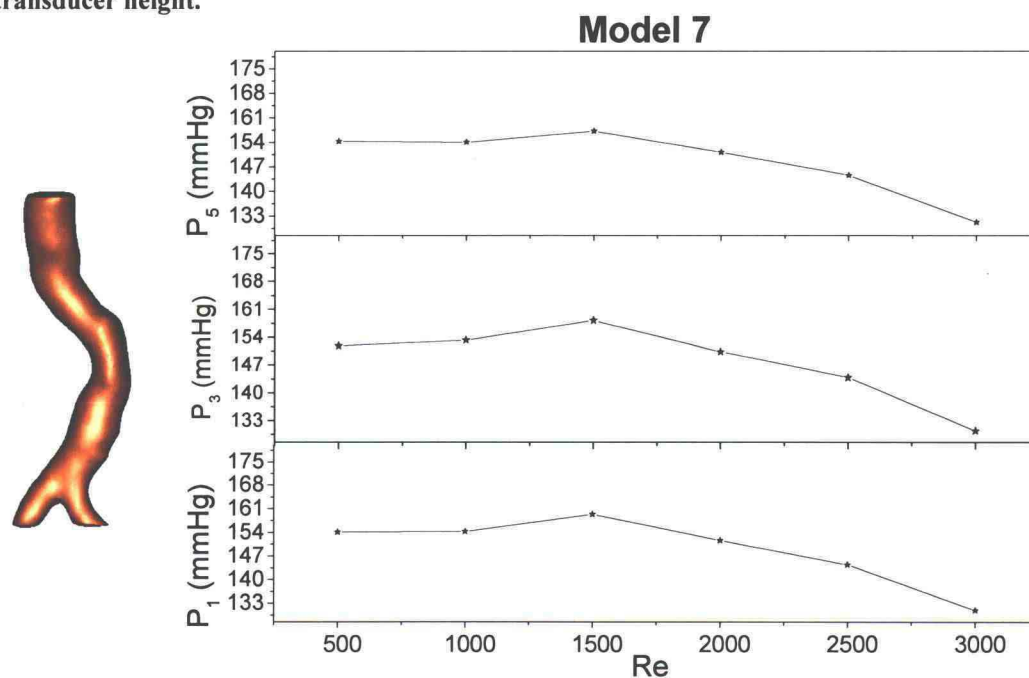
In figure 4.7, 4.8 and 4.9, pressure plots of P_1 , P_3 and P_5 of model 7,8 and 11 for all Reynolds numbers were shown. From these plots wall pressure is found to decrease with increasing Re (Q).

Correction Factors of Model 7				
Transducer	H_1 (cm)	H_2 (cm)	$H_{correction}$ (cm)	$P_{correction}$ (mmHg)
1	6.383	3.905	10.288	7.570
2	6.383	3.228	9.611	7.072
3	6.383	3.160	9.5428	7.0217
4	6.383	3.421	9.804	7.214
5	6.383	4.190	10.573	7.780

Table 4.11 Correction factors of model 7.

Wall Pressure Distribution of Model 7						
Pressure \ Re	500	1000	1500	2000	2500	3000
P_{1wall} (mmHg)	154.065	154.206	159.358	151.691	144.418	130.939
P_{2wall} (mmHg)	153.204	153.214	158.527	150.749	143.719	130.951
P_{3wall} (mmHg)	151.850	153.254	158.244	150.345	143.941	130.777
P_{4wall} (mmHg)	155.618	153.295	156.659	150.406	143.851	130.442
P_{5wall} (mmHg)	154.275	154.083	157.163	151.123	144.557	131.205

Table 4.12 Absolute wall pressure distributions, in mmHg of, model 7, corrected for transducer height.

Figure 4.7 Pressure plots of P_1 , P_3 and P_5 of model 7 for all Reynolds numbers were shown.

Correction Factors of Model 8

Transducer	H_1 (cm)	H_2 (cm)	$H_{\text{correction}}$ (cm)	$P_{\text{correction}}$ (mmHg)
1	6.365	4.368	10.733	7.897
2	6.365	4.374	10.739	7.902
3	6.365	3.808	10.173	7.485
4	6.365	4.531	10.897	8.018
5	6.365	3.785	10.150	7.468

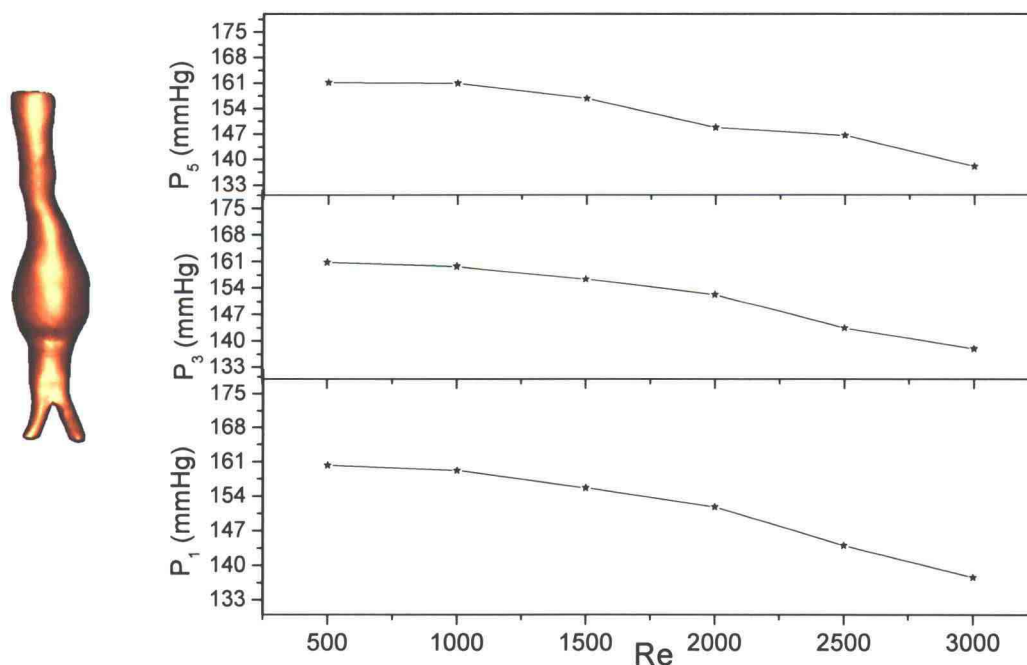
Table 4.13 Correction factors of model 8.

Wall Pressure Distribution of Model 8

Pressure \ Re	500	1000	1500	2000	2500	3000
$P_{1\text{wall}}$ (mmHg)	160.287	159.197	155.657	151.777	144.030	137.551
$P_{2\text{wall}}$ (mmHg)	160.142	159.452	155.862	152.022	144.127	137.955
$P_{3\text{wall}}$ (mmHg)	160.718	159.728	156.273	152.293	143.441	137.955
$P_{4\text{wall}}$ (mmHg)	160.462	159.432	156.089	152.280	144.146	138.168
$P_{5\text{wall}}$ (mmHg)	159.822	159.175	155.367	151.509	143.569	137.803

Table 4.14 Absolute wall pressure distributions, in mmHg of, model 8, corrected for transducer height.

Model 8

Figure 4.8 Pressure plots of P_1 , P_3 and P_5 of model 8 for all Reynolds numbers were shown.

Correction Factors of Model 11

Transducer	H_1 (cm)	H_2 (cm)	$H_{\text{correction}}$ (cm)	$P_{\text{correction}}$ (mmHg)
1	6.975	4.483	11.458	8.431
2	6.975	5.532	12.507	9.203
3	6.975	4.357	11.332	8.338
4	6.975	4.633	11.608	8.541
5	6.975	5.156	12.131	8.926

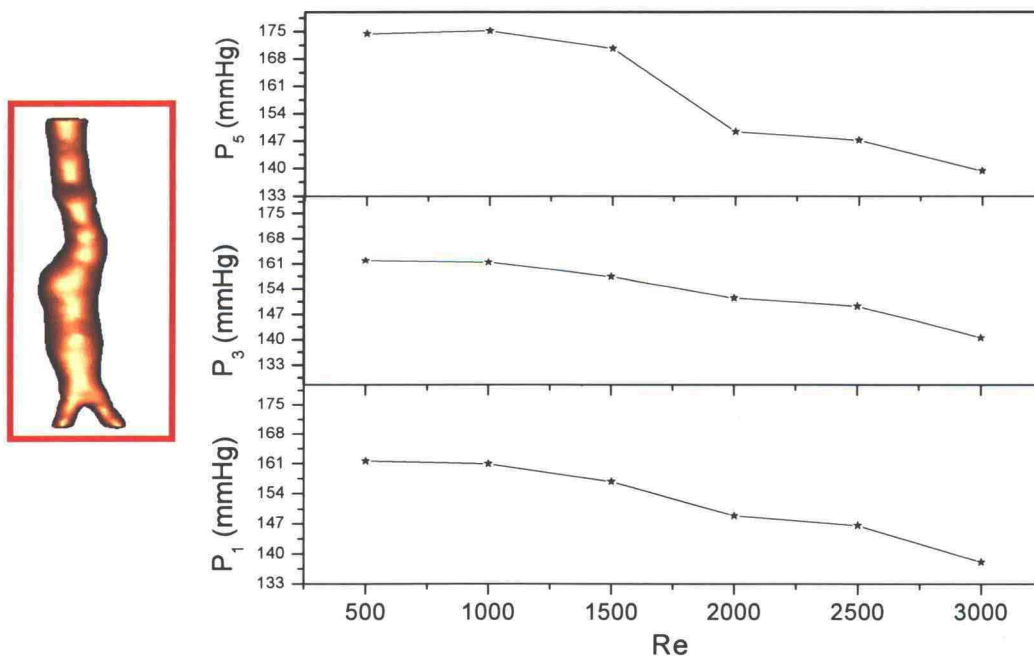
Table 4.15 Correction factors of model 11.

Wall Pressure Distribution of Model 11

Pressure \ Re	500	1000	1500	2000	2500	3000
$P_{1\text{wall}}$ (mmHg)	161.153	160.875	156.782	148.805	146.653	138.112
$P_{2\text{wall}}$ (mmHg)	162.037	161.646	157.677	149.530	147.467	138.812
$P_{3\text{wall}}$ (mmHg)	161.978	161.421	157.452	151.389	149.268	140.503
$P_{4\text{wall}}$ (mmHg)	162.294	161.799	157.778	149.027	146.822	138.740
$P_{5\text{wall}}$ (mmHg)	174.472	175.188	170.619	149.243	147.130	139.333

Table 4.16 Absolute wall pressure distributions, in mmHg of, model 11, corrected for transducer height.

Model 11

Figure 4.9 Pressure plots of P_1 , P_3 and P_5 of model 11 for all Reynolds numbers were shown.

CHAPTER 5: DISCUSSION

5.1 GEOMETRIC PARAMETERS

5.1.1 AAA Geometric Parameter Analysis Based on Thrombus Existence

Patient AAAs can be categorized into two groups, those without thrombus and those presenting measurable thrombus deposits. Six of the models shown in figure 4.1 which are shown separately in figure 5.1, presented with no measurable thrombus (Table 5.1). The other 29 showed extensive regions of distributed thrombus (Table 5.2). To determine the statistical significance of differences between these two groups a one-way ANOVA test approximation was used. For each geometric parameter, p -values less than 0.05 were considered significant (Table 5.3).

AAA without measurable thrombus

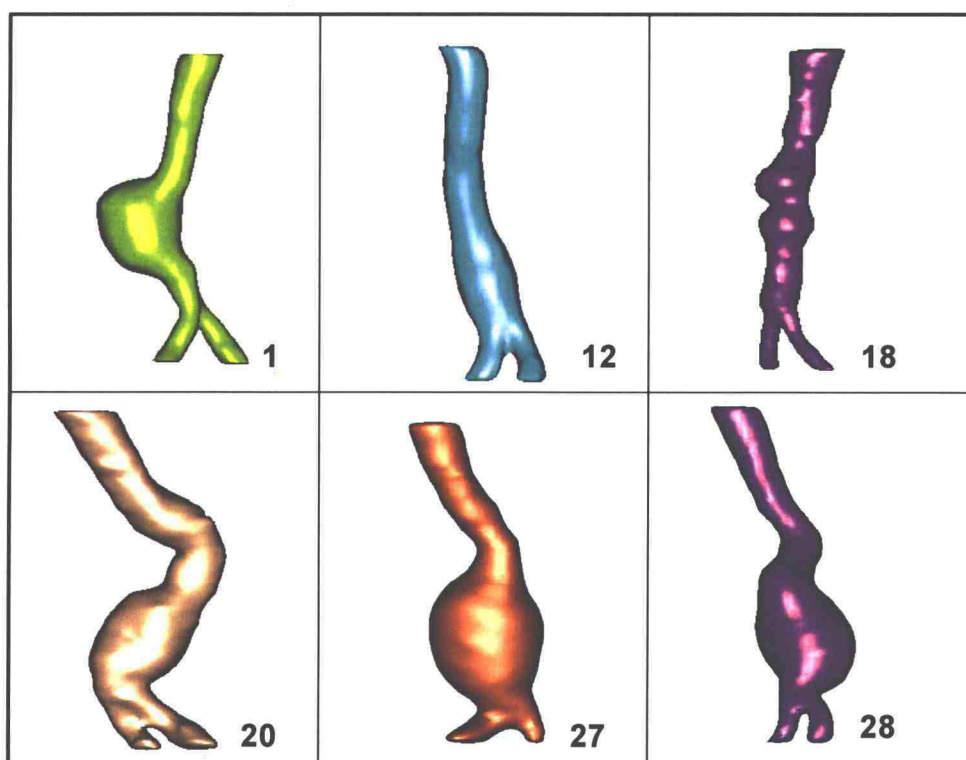


Figure 5.1 Six of 35 AAA models without measurable thrombus: Patient AAAs can be categorized into two groups, those without thrombus and those presenting measurable thrombus deposits.

Mean \pm S.D. of AAA Geometric Parameters (*without thrombus*)

N=6	D (cm)	d (cm)	D/d	D_{Lumen} (cm)	L (cm)	V_{Lumen} (cm³)	$V_{Thrombus}$ (cm³)	V_{AAA} (cm³)	LI	τ	θ (deg)	κ_h (cm⁻¹)	κ_v (cm⁻¹)
MIN	3.14	2.00	1.57	3.140	5.58	32.62	0	32.62	1	1.05	3.70	0.333	0.150
MAX	6.00	2.74	2.47	6.00	9.00	144.99	0	144.99	1	1.40	31.33	0.637	0.288
Mean\pmS.D.	4.97 \pm 1.04	2.42 \pm 0.302	2.06 \pm 0.39	4.76 \pm 1.26	7.83 \pm 1.71	100.0 \pm 39.9	0	100.0 \pm 39.9	1	1.24 \pm 0.136	12.7 \pm 10.5	0.422 \pm 0.112	0.210 \pm 0.054

Table 5.1 Mean and standard deviation of AAA geometric parameters for patients without measurable thrombus (N= 6).

Mean \pm S.D. of AAA Geometric Parameters (*with thrombus*)

N=29	D (cm)	d (cm)	D/d	D_{Lumen} (cm)	L (cm)	V_{Lumen} (cm³)	$V_{Thrombus}$ (cm³)	V_{AAA} (cm³)	LI	τ	θ (deg)	κ_h (cm⁻¹)	κ_v (cm⁻¹)
MIN	4.70	2.01	1.71	2.09	5.00	26.67	20.33	71.27	0.096	0.169	1.10	0.260	0.113
MAX	7.70	2.96	3.47	6.28	13.74	251.45	170.72	304.00	0.821	0.790	29.61	0.426	0.390
Mean\pmS.D.	5.81 \pm 0.727	2.48 \pm 0.244	2.35 \pm 0.427	3.78 \pm 0.990	8.55 \pm 2.23	77.2 \pm 45.0	61.1 \pm 37.5	138.3 \pm 53.5	0.463 \pm 0.230	1.40 \pm 0.343	12.46 \pm 6.44	0.349 \pm 0.041	0.217 \pm 0.080

Table 5.2 Mean and standard deviation of AAA geometric parameters for patients with measurable thrombus (N= 29).

Significant Differences (<i>p</i> -value)											
	D (cm)	d (cm)	D/d	D_{Lumen} (cm)	L (cm)	V_{Lumen} (cm ³)	V_{AAA} (cm ³)	τ	θ (deg)	κ_h (cm ⁻¹)	κ_v (cm ⁻¹)
<i>p</i> -Value	0.0221	0.6201	0.1228	0.0415	0.4657	0.2584	0.1082	0.2777	0.9520	0.0083	0.8464

Table 5.3 To find the significant differences between patients with measurable thrombi and those without, *p*-values for each geometric parameter were calculated using ANOVA test.

These results clearly suggest a number of small but significant differences between aneurysms with measurable thrombi and those without. The first distinction between the two groups is in the diameter of the lumen ($p=0.04$). Patients with thrombi showed an average lumen diameter of 3.78 cm, with a standard deviation of 0.990 cm. In contrast, the models without thrombus had an average diameter of 4.76 cm with a standard deviation of 1.26 cm (Fig. 5.2).

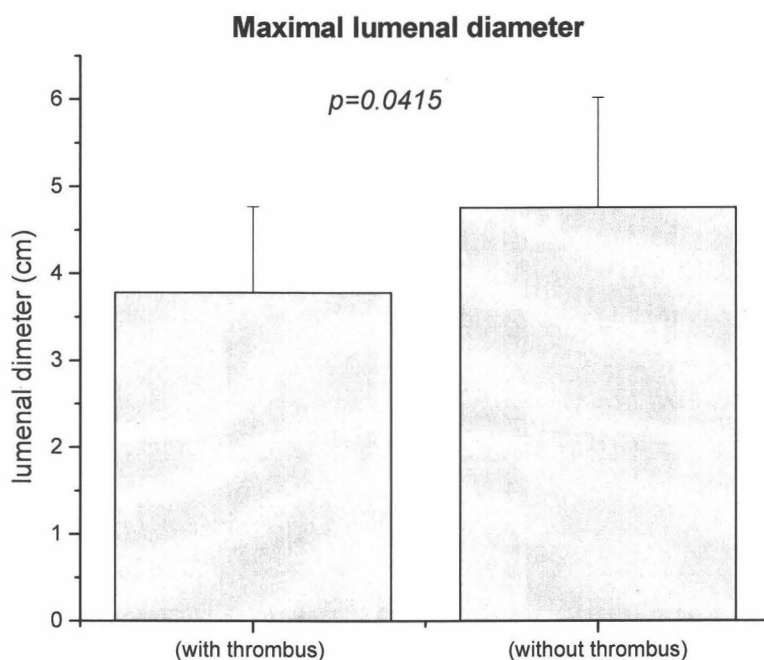


Figure 5.2 Maximal luminal diameter of the AAAs for 35 patients: non-thrombosed patients (N=29) had significant larger luminal diameter than thrombosed group (N=6) ($p<0.05$), where patients with and without thrombus had mean \pm S.D. values of 3.78 ± 0.990 cm and 4.76 ± 1.26 cm respectively.

Although it seemed that patients without thrombus had larger luminal volumes than those with thrombus (77.2 ± 45.0 vs. $100.0 \pm 39.9 \text{ cm}^3$) in fact the difference was not significant ($p=0.26$). However, thrombosed patients had significant larger bulge diameter than non-thrombosed group ($p=0.02$), where patients with and without thrombus had mean \pm S.D. values of $5.81 \pm 0.727 \text{ cm}$ and $4.97 \pm 1.04 \text{ cm}$ respectively (Fig. 5.3).

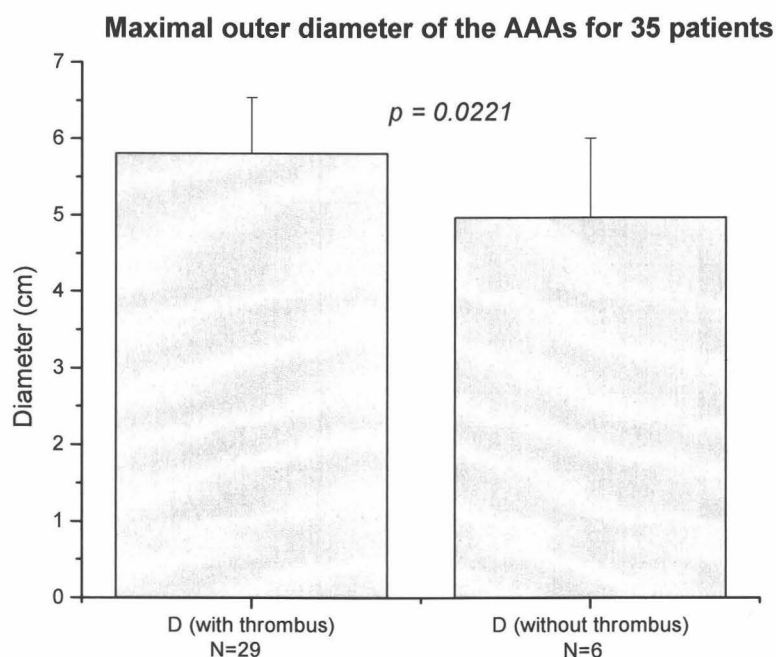


Figure 5.3 Maximal outer diameter of the AAAs for 35 patients: thrombosed patients (N=29) had significant larger bulge diameter than non-thrombosed group (N=6) ($P<0.05$), where patients with and without thrombus had mean \pm S.D. values of $5.81 \pm 0.727 \text{ cm}$ and $4.97 \pm 1.04 \text{ cm}$ respectively.

In spite of that discrepancy, there was no significant difference between the average total volume of group one and two ($p=0.11$) with mean \pm S.D. of 138.3 ± 53.5 vs. $100.0 \pm 39.9 \text{ cm}^3$. In addition, the diameter ratio was higher for patients with thrombus (2.35 ± 0.427 vs. 2.06 ± 0.39), although this difference is not significant ($p=0.12$).

Even though thrombosed patients had larger mean non-dilated diameter than those without thrombus (2.48 ± 0.244 vs. 2.42 ± 0.302 cm) in fact this difference is not significant ($p=0.6$).

There were no significant differences between the average lesion length of patients with thrombus and without thrombus ($p=0.47$), even though lesion lengths of thrombosed patients had larger average and standard deviation than those without (8.58 ± 2.21 vs. 7.76 ± 1.34 cm).

Degrees of vertical curvatures were not also significantly different between these two groups ($p=0.85$). Patients with thrombus had an average vertical curvature of 0.217 cm^{-1} with a standard deviation of 0.080 cm^{-1} , while those without had average and standard deviation of $0.210 \pm 0.054 \text{ cm}^{-1}$. However, patients without thrombus had significantly larger horizontal curvature than thrombosed patients ($p=0.008$). Alternatively, patients with thrombus were more horizontally straight ($0.349 \pm 0.041 \text{ cm}^{-1}$ vs. $0.422 \pm 0.112 \text{ cm}^{-1}$) (Fig. 5.4).

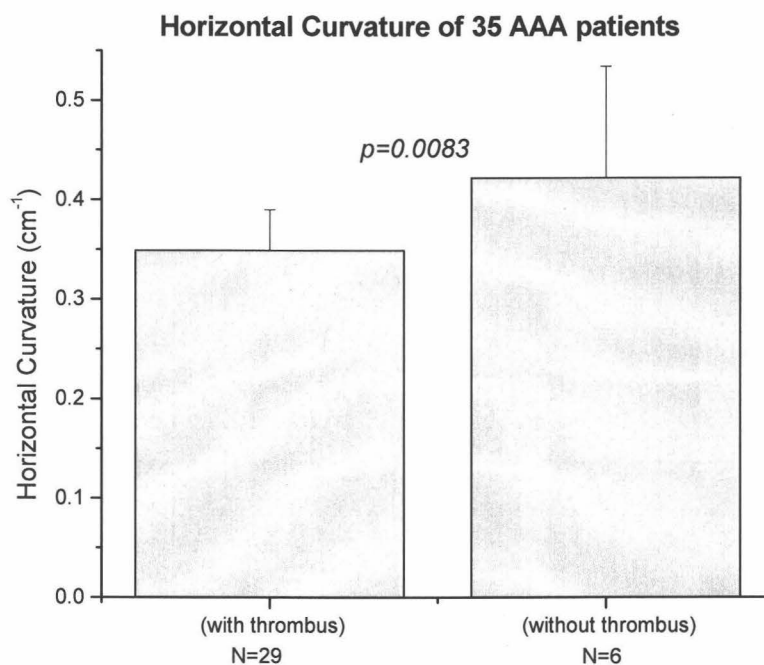


Figure 5.4 Horizontal curvature, κ_h , of the 35 AAA patients: patients without thrombus had significantly larger horizontal curvature than thrombosed patients ($P<0.05$) or patients with thrombus were more horizontally straight ($0.349 \pm 0.041 \text{ cm}^{-1}$ vs. $0.422 \pm 0.112 \text{ cm}^{-1}$).

Patients with thrombi had also larger average tortuosity than without thrombus (1.40 ± 0.343 vs. 1.24 ± 0.136), but this is not a significant difference ($p=0.28$). Angular deviation was nearly identical for both groups (12.46 ± 6.44 vs. 12.7 ± 10.5).

All of these differences are potentially highly clinically important, since it is known that large diameter AAAs are more prone to failure than are smaller lesions [1].

5.1.2 AAA Geometric Parameters Analysis

To assess geometric characteristics of AAA patients, the correlations of relations between parameters were analyzed. The following questions were posed:

- 1) Does larger diameter indicate larger bulge volume?
- 2) Is it appropriate to assume AAA maximum diameter as the only risk factor in assessing the risk of rupture?
- 3) Does a bulge with larger diameter have also larger tortuosity?
- 4) Is there any correlation between horizontal curvature and bulge tortuosity?
- 5) Does a bulge with larger angular deviation have also larger vertical curvature?
- 6) Does higher D/d ratio mean high LI ?
- 7) Does model with high LI have necessarily high $V_{Thrombus} / V_{AAA}$ ratio?
- 8) Does model with high $V_{Thrombus}$ ratio have also large angular deviation?
- 9) Do thrombosed models with higher D/d ratio have necessarily larger thrombus volume?
- 10) Is there any relationship between thrombus formation and non-dilated diameter?

To discuss each question, these parameters were plotted appropriately. The low value of the least squares regression (R^2) related to the high individual variability between patients, while generally in this study $R^2 > 0.1$

was assumed as a best-fit line. Alternatively, $R^2 > 0.1$ shows significant relationship between any two discussed parameters (Fig. 5.5-5.17).

1) Does larger diameter indicate larger bulge volume?

Figure 5.5 is a plot of AAA volume versus diameter, along with the best-fit line computed by least squares regression. Since R^2 is larger than 0.1, therefore diameter and AAA volume have significant correlation. In addition, the positive slope of the best-fit line indicates that AAA with larger diameter has also larger volume, on average.

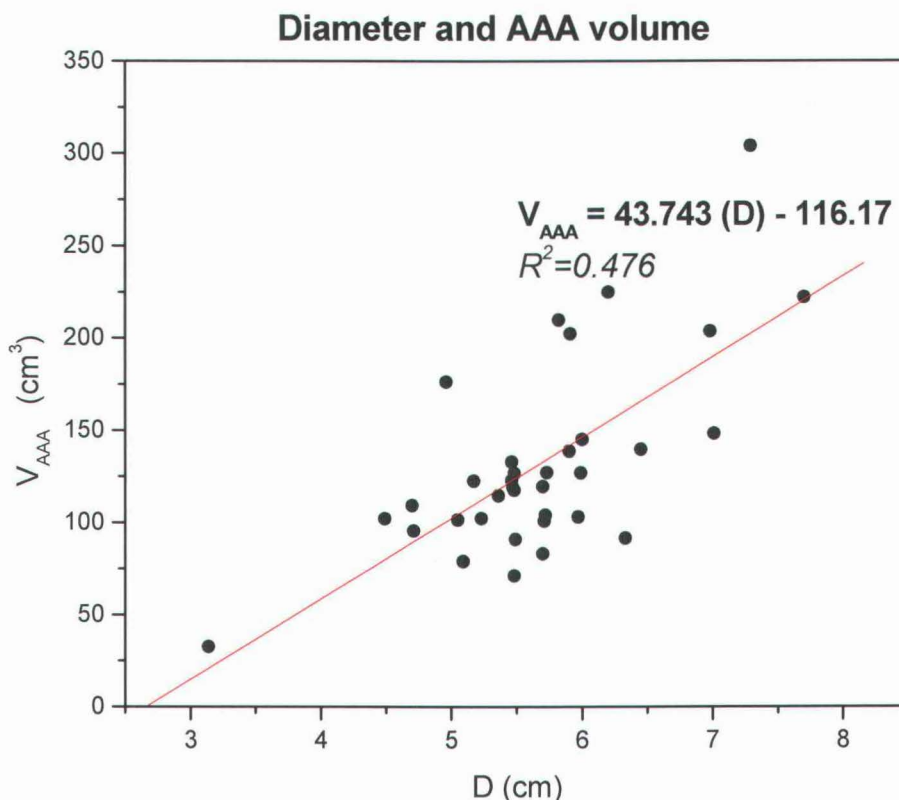


Figure 5.5 Plot of AAA volume versus diameter, along with the best-fit line computed by least squares regression. Since R^2 is larger than 0.1, therefore diameter and AAA volume have significant correlation.

2) Is it appropriate to assume AAA maximum diameter as the only factor in assessing the bulge volume growing?

According to the present definition, AAA is a local progressive dilation of an artery to at least 1.5 times its normal diameter [16]. Diameter has been the most commonly used factor to predict rupture risk since the work of Szilagyi *et. al.* 40 years ago [1]. However as the aneurysmal lesion progresses, both diameter and length can be expected to grow. Therefore dilation volume may be a more complete indicator of progression than diameter alone. We tested correlations between dilation volume and other geometric parameters. Finding these correlations is critical in an effort to improve on the limitations of the use of AAA diameter as the only factor in assessing risk of rupture.

In plots 5.6, 5.7 and 5.8, correlations between AAA volume and other geometric parameters are shown. In figure 5.6, bulge volume versus tortuosity was plotted along with the best-fit line computed by least squares regression. The low regression value ($R^2 = 0.006$) reveals that there is no significant relationship between these two parameters.

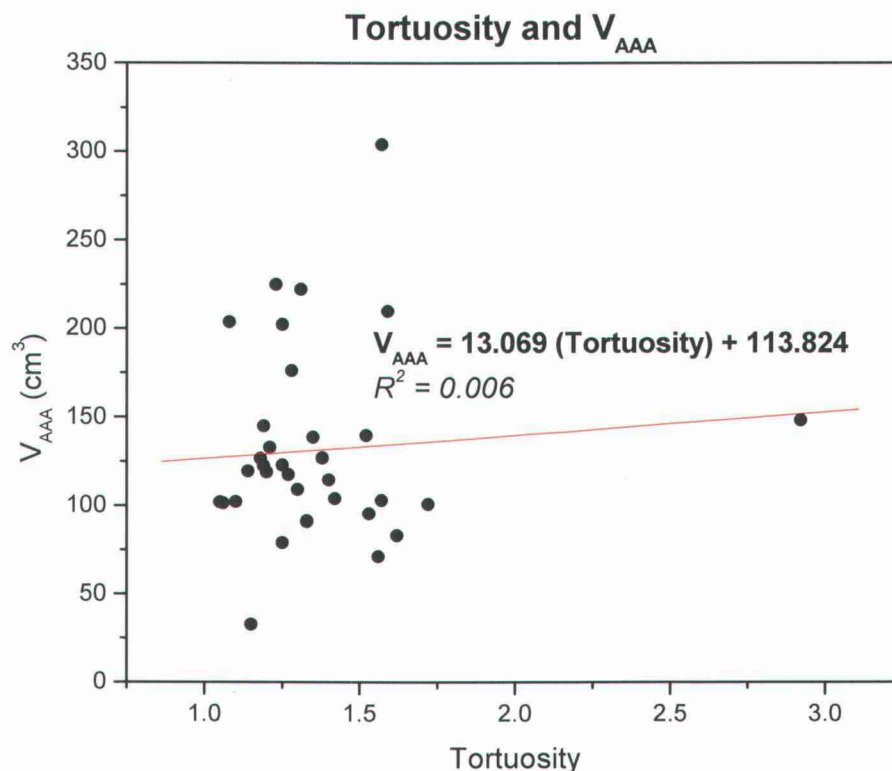


Figure 5.6 Bulge volume versus tortuosity was plotted along with the best-fit line computed by least squares regression.

Figure 5.7 is a plot of the bulge volume versus length along with the best-fit line computed by least squares regression. In this case, the regression value ($R^2 > 0.1$) reveals significant relationship between these two parameters.

Based on this graph longer AAAs also have larger volume on average.

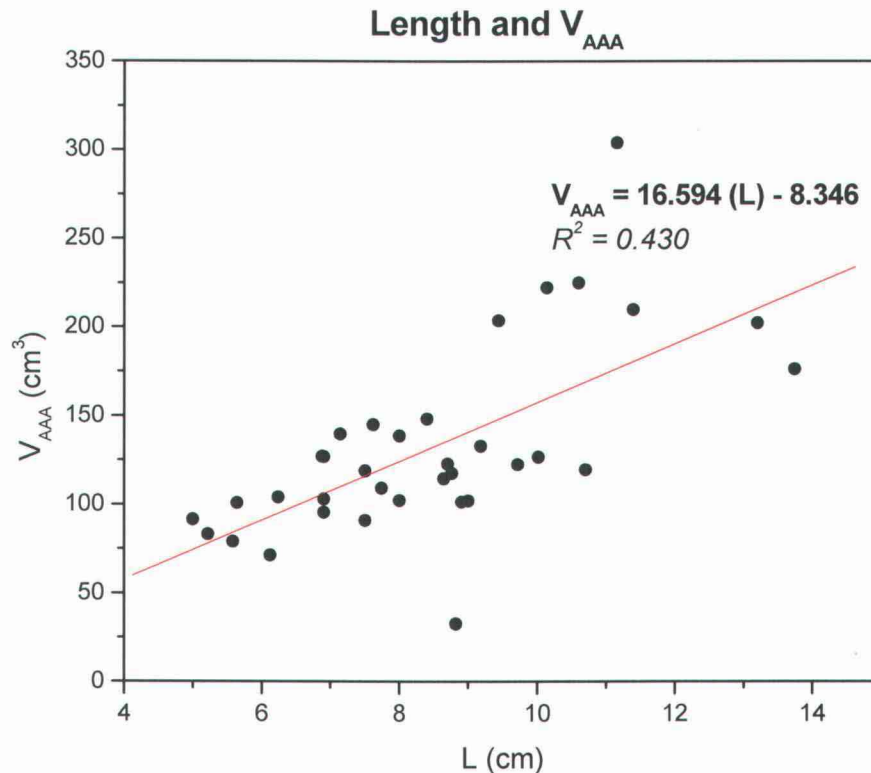


Figure 5.7 Plot of the bulge volume versus length along with the best-fit line computed by least squares regression. The regression value ($R^2 > 0.1$) reveals significant relationship between these two parameters.

Figure 5.8 is a plot of AAA volume versus vertical curvature, along with the best-fit line computed by least squares regression. The negative slope of the line shows that AAA volume decreasing with growing of vertical curvature. However, low value of the least squares regression ($R^2 = 0.074$) shows the large individual variability between patients.

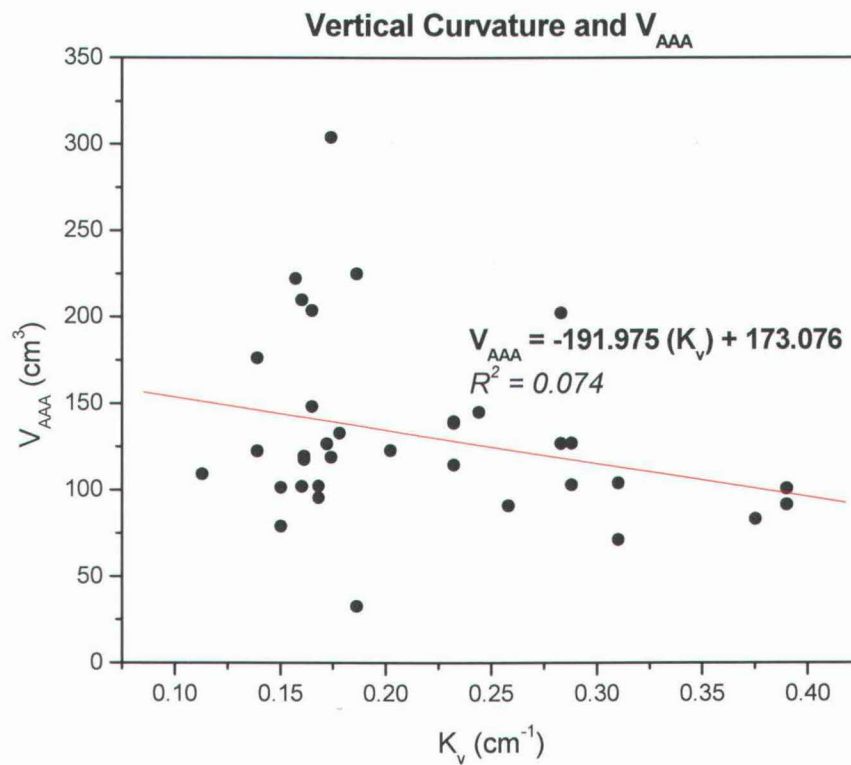


Figure 5.8 Plot of the bulge volume versus vertical curvature along with the best-fit line computed by least squares regression. The low value of the correlation coefficient (R^2) related indicates the large individual variability between patients.

The plot of the bulge volume versus diameter ratio (D/d) is shown in figure 5.9. The AAA volume is functionally dependent on this ratio since the high regression value ($R^2 = 0.454$) displays significant relationship between these two parameters.

Consequently, beside diameter the dilation volume is also related to its length and D/d on average.

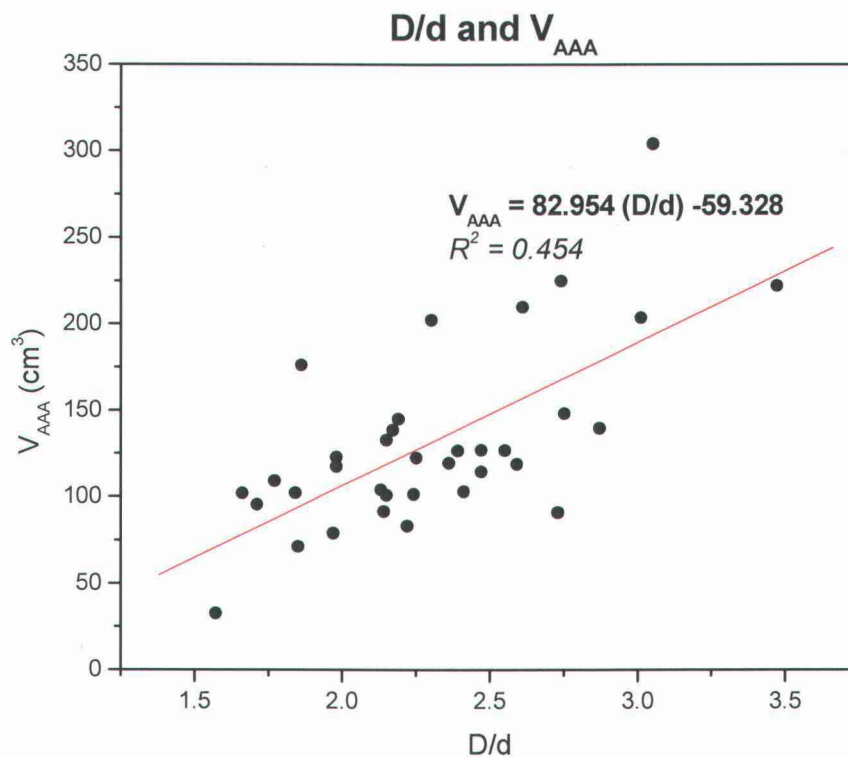


Figure 5.9 Plot of the bulge volume versus diameter ratio (D/d) along with the best-fit line computed by least squares regression was shown. It shows that AAA volume is functionally dependent to this ratio.

3) Does a bulge with larger diameter have also larger tortuosity?

To analyze this correlation, a scatter graph of tortuosity versus diameter along with the best-fit line was computed and plotted (Fig. 5.10). The value of the least squares regression ($R^2 = 0.141$) shows that on average bulge with larger diameter has also higher tortuosity.

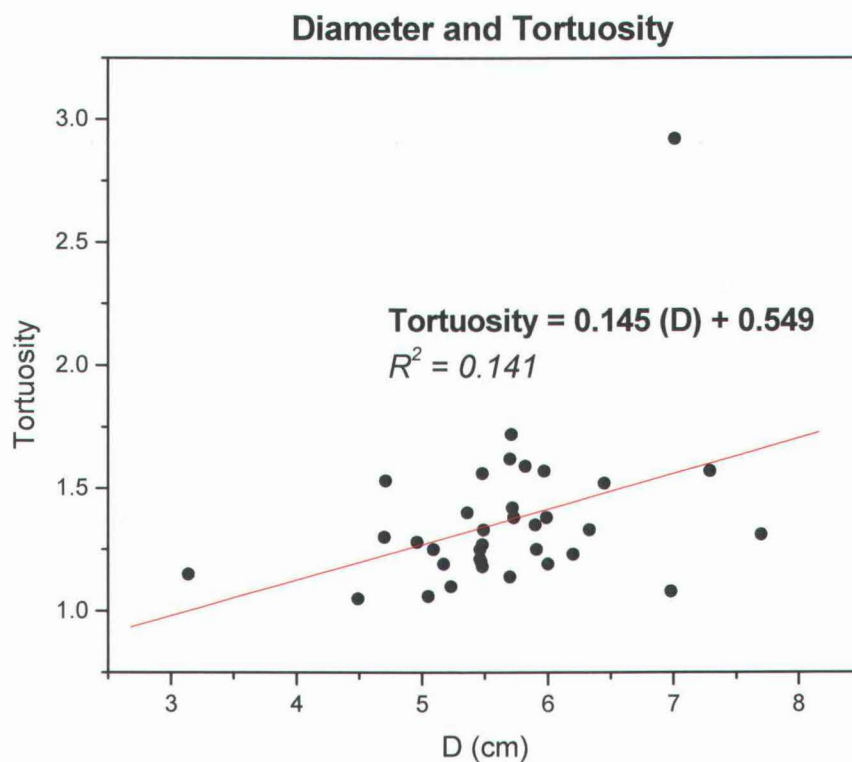


Figure 5.10 A scatter graph of tortuosity versus diameter along with the best-fit line was computed and plotted by least squares regression. According to this plot these two parameters are linearly dependent.

4) Is there any correlation between horizontal curvature and bulge tortuosity?

For the purposes of finding this correlation, a plot based on these two set of data was produced (Figure 5.11). The least squares regression of the best-fit line shows a significant dependency between these two parameters ($R^2 = 0.108$).

The negative slope of this plot shows that generally as the horizontal curvature of a bulge decreases the tortuosity of it increases.

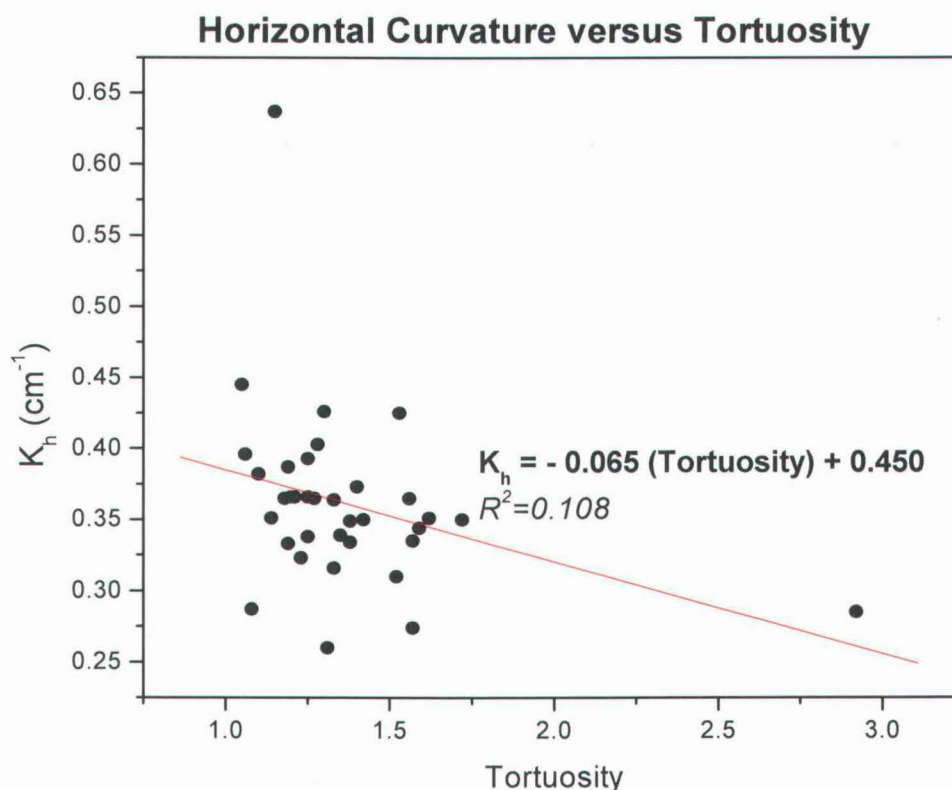


Figure 5.11 A scatter plot of the horizontal curvature versus tortuosity along with the best-fit line. The least squares regression of this line shows a significant dependency between these two parameters ($R^2 > 0.1$).

5) Does a bulge with larger angular deviation have also larger vertical curvature?

In figure 5.12, vertical curvature versus angular deviation is plotted along with the best-fit line seems computed by least squares regression. The low regression value ($R^2 = 0.001$) reveals no significant relationship between these two parameters. Therefore, a bulge with larger angular deviation does not necessarily have larger vertical curvature.

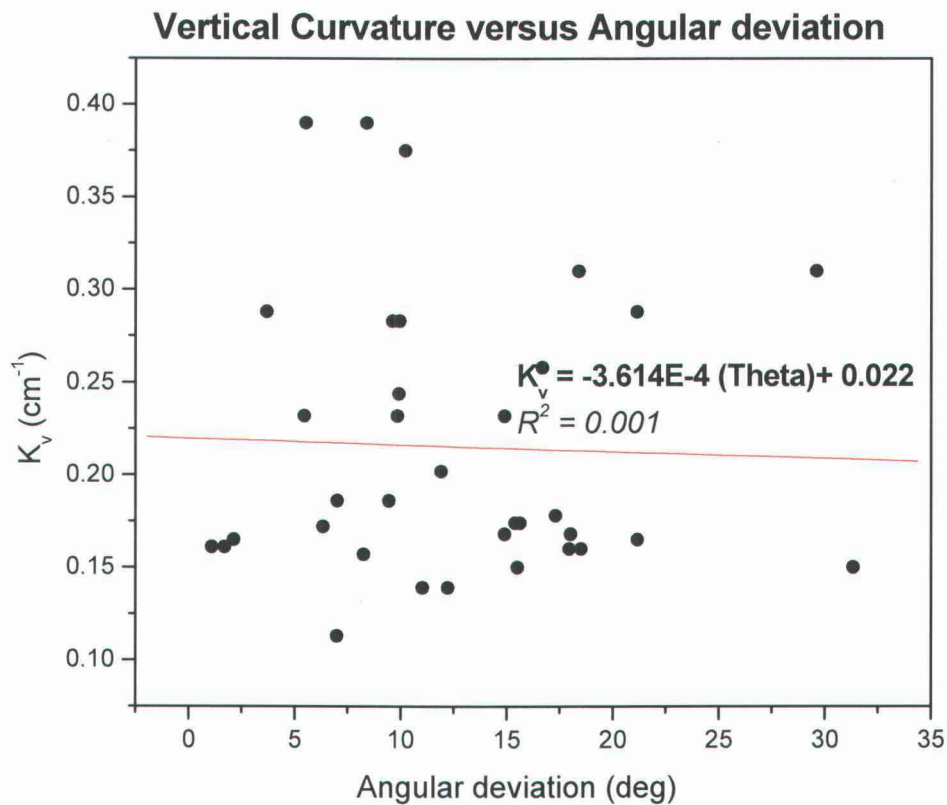


Figure 5.12 Vertical curvature versus angular deviation. The low regression value ($R^2 = 0.001$) reveals no significant relationship between these two parameters.

6) Does higher D/d ratio mean also higher LI ?

For the purposes of finding this correlation, a plot based on these two set of data were produced. The least squares regression of the best-fit line shows no significant dependency between these two parameters ($R^2 \ll 0.1$) (Figure 5.13).

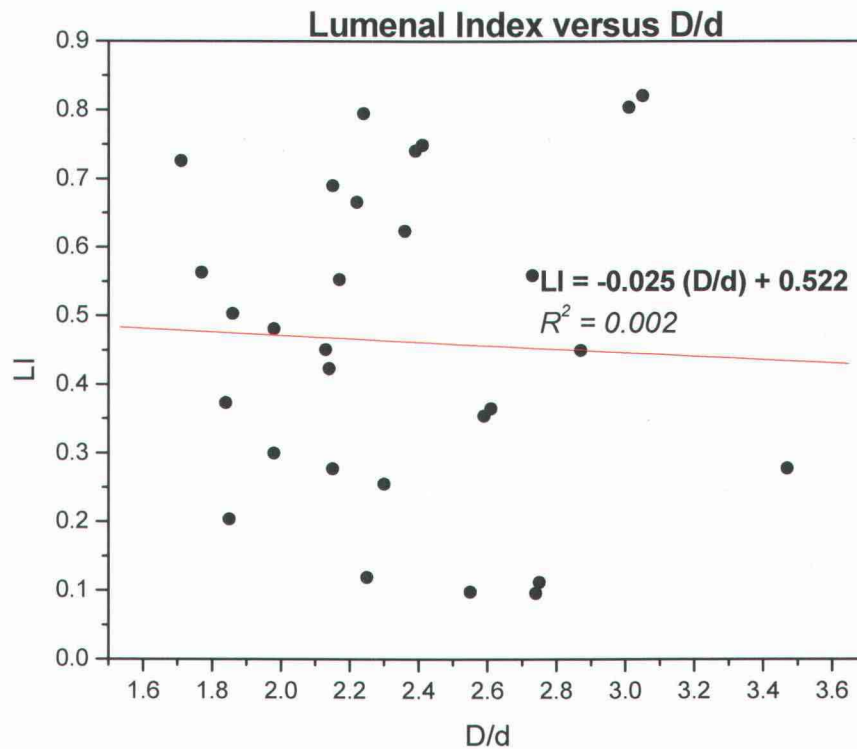


Figure 5.13 Luminal index versus D/d was plotted along with the best-fit line computed by least squares regression for 28 patients with measurable thrombus. Although this line shows dependency of LI to D/d, but the low regression value ($R^2 = 0.002$) reveals no significant relationship between these two parameters.

7) Does a model with high LI necessarily have a high $V_{Thrombus} / V_{AAA}$ ratio?

Since luminal index and $V_{Thrombus} / V_{AAA}$ both are parameters which were defined based on the thrombus existence (28 patients), these two parameters may also functionally related. To find their correlation, a scatter plot of $V_{Thrombus} / V_{AAA}$ versus luminal index is shown in figure 5.14. The least squares regression value ($R^2 = 0.126$) shows that these two geometric properties of the bulge are functionally dependent. In this case, the line reveals that bulges with higher LI have also higher $V_{Thrombus} / V_{AAA}$ on average.

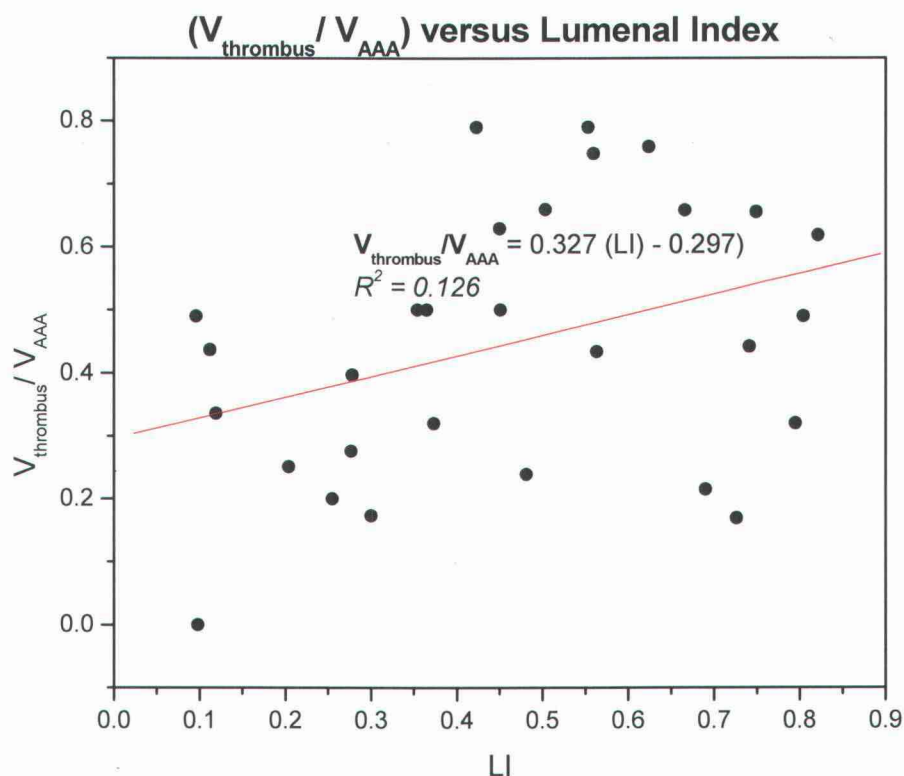


Figure 5.14 Plot of the volume ratio versus luminal index (for 28 thrombosed patients). The least squares regression value ($R^2 > 0.1$) shows that these two geometric properties of the bulge are functionally dependent. In this case, the positive slope of the line reveals that on average, bulge with higher LI have also higher $V_{\text{Thrombus}} / V_{\text{AAA}}$.

8) Do models with high V_{Thrombus} ratio also have large angular deviation?

The plot of the V_{Thrombus} versus angular deviation along with the best-fit line computed by least squares regression, is shown in figure 5.15. Since the value of R^2 is lower than 0.1, it can be concluded that there is no functional relationship between these two parameters.

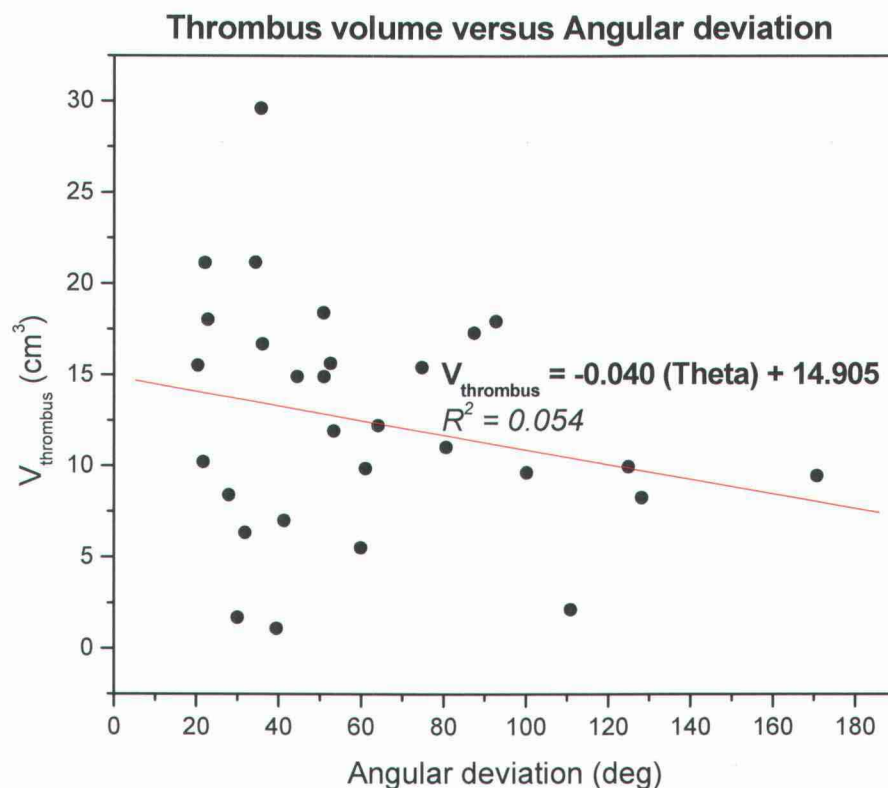


Figure 5.15 Plot of the thrombus volume versus angular deviation (for 28 patients with thrombus). The low value of least squares regression ($R^2 < 0.1$) shows that these two geometric properties of the bulge are not functionally dependent.

9) Do thrombosed models with higher D/d ratio have necessarily larger thrombus volume?

While thrombus formation within AAA sac is still under investigation, the correlation between thrombus volume and D/d ratio was investigated here.

Figure 5.16 this data along with the best-fit line. According to this plot, on average any lumen with higher D/d has also higher thrombus volume.

Consequently, there is a significant relationship between thrombus volume and D/d ratio between 28 thrombosed patients ($R^2 = 0.188$).

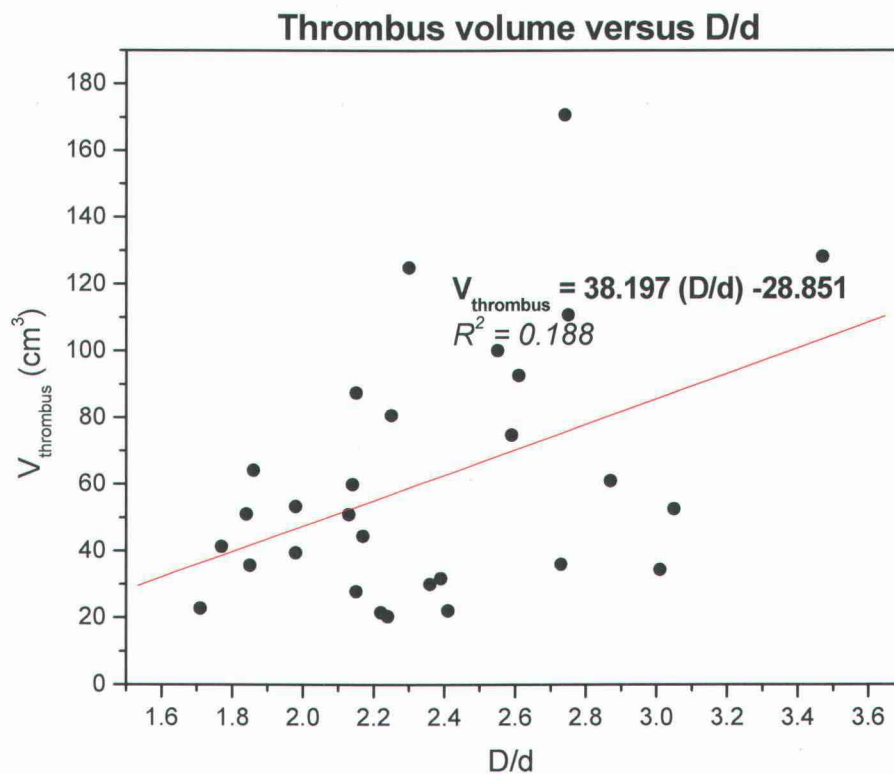


Figure 5.16 The best-fit line computed for analysis of thrombus volume versus D/d. On average, any lumen with higher D/d has also higher thrombus volume. Consequently, there is a significant relationship between thrombus volume and D/d ratio between 28 thrombosed patients ($R^2 = 0.188$).

10) Is there any relationship between thrombus volume and non-dilated diameter?

Because question 9 shows a significant relationship between thrombus volume and D/d, the correlation of thrombus volume and non-dilated diameter of the lumen was also investigated. For this purpose, a scatter plot of these two geometric parameters is shown in figure 5.17 along with the best-fit line computed by least squares regression. The high value of ($R^2 = 0.433$) reveals significant correlation between these two parameters. The negative slope of the best-fit line reveals that lumens with larger non-dilated diameter generally have lower thrombus volume within its AAA sac.

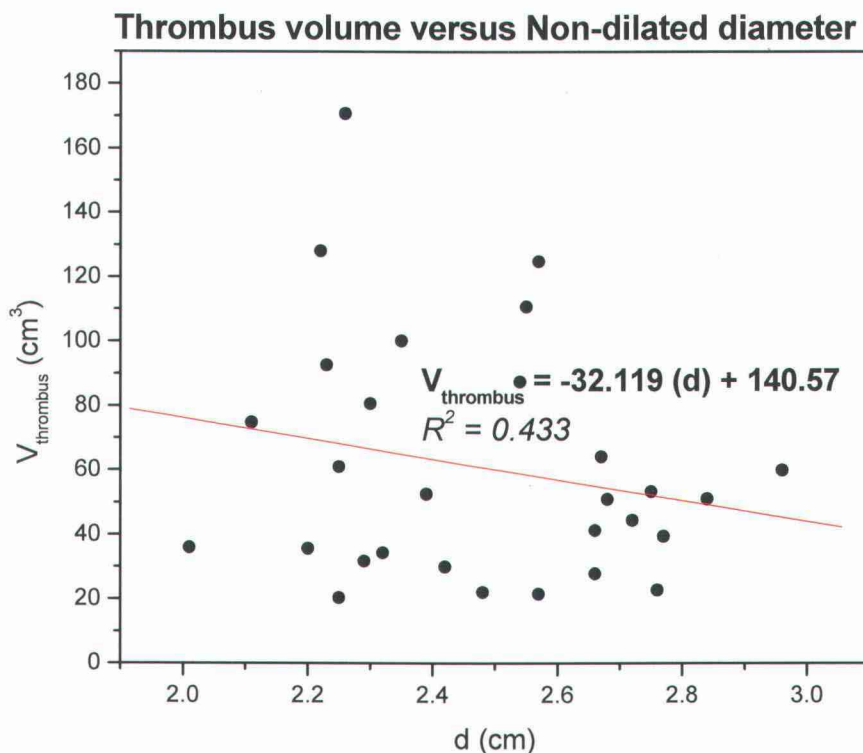


Figure 5.17 Scatter plot of thrombus volume versus non-dilated lumen diameter. The high value of R^2 reveals that there is a significant correlation between these two parameters. The negative slope of the best-fit line reveals that lumen with bigger non-dilated diameter generally has higher thrombus volume within its AAA sac.

5.1.3 Bulge Surface Similarity Evaluation

Bulge surface similarity parameters were also analyzed based on measurable thrombus deposits (29 thrombosed patients, 6 non-thrombosed patients (Fig. 5.1)). For finding the significant differences between these two groups, p -values for each bulge surface similarity parameter were also calculated and are shown in table 5.4.

Patients with thrombus appeared to have larger bulge surface areas than those without thrombus (149.390 ± 39.41 vs. $116.39 \pm 27.70 \text{ cm}^3$), but this difference is not significant, since its p -value is 0.0607. Means and standard deviations of bulge surface similarity ratios ($\frac{S_b}{S_c}$ and $\frac{S_b}{S_s}$) for patients with and

without thrombus were also shown in the table. Column 3 present mean and standard deviation of $\frac{S_b}{S_c}$ ratio of patients without thrombus and with thrombus which have mean and standard deviation values of 1.716 ± 0.472 and 1.940 ± 0.366 respectively, while $\frac{S_b}{S_s}$ of thrombosed patients and non-thrombosed patients have mean and standard deviation values of 1.429 ± 0.386 and 1.566 ± 0.420 .

Bulge Surface Similarity			
	Surface of Bulge (S_b) (cm^2)	$\frac{S_b}{S_c}$	$\frac{S_b}{S_s}$
<i>Patients with thrombus (N=29)</i>	149.390 ± 39.413	1.940 ± 0.366	1.429 ± 0.386
<i>Patients without thrombus (N=6)</i>	116.390 ± 27.695	1.716 ± 0.472	1.566 ± 0.420
<i>p-value</i>	0.0607	0.2027	0.4402

Table 5.4 Bulge surface similarities, based on measurable thrombus deposits (29 thrombosed patients, 6 non-thrombosed patients).

The differences between thrombosed and non-thrombosed patients were not statistically significant ($p > 0.05$). However, by evaluating each group individually, it was concluded that the bulge shape of patients with thrombus is significantly more similar to a sphere than a cylinder ($p < 0.0001$) (Fig. 5.18). Consequently, for thrombosed patients, the similarity of their bulge shapes is more near to their corresponding spheres which were defined for each bulge as a sphere with maximum diameter of the bulge (D).

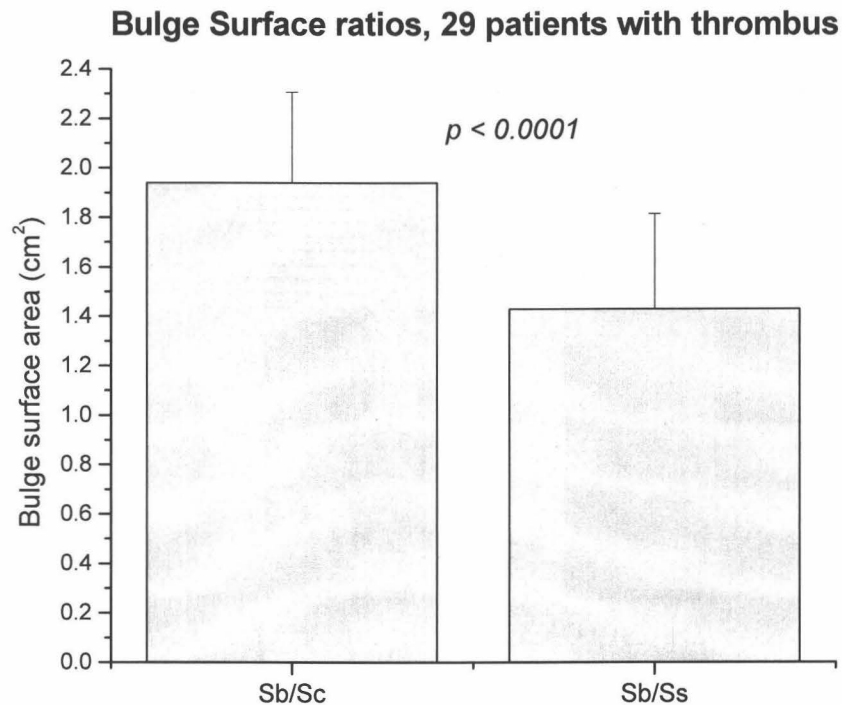


Figure 5.18 It concluded that bulge shape of patients with thrombus is significantly more similar to a sphere than cylinder ($p < 0.0001$). Consequently, for thrombosed patients, similarity of their bulge shapes are more near to their corresponding spheres which were defined for each bulge as a sphere with maximum diameter of the bulge (D).

Bulge surface similarity parameters were also evaluated based on finding their correlations with geometric parameters. Therefore, in the next set of figures (Fig. 5.19 to 23), the scatter plots of these parameters were shown along with best-fit line computed by least squares regression. In all of these plots

Figure 5.19 presents bulge surface area versus tortuosity. These two parameters are not functionally dependent ($R^2 = 0.001 < 0.1$).

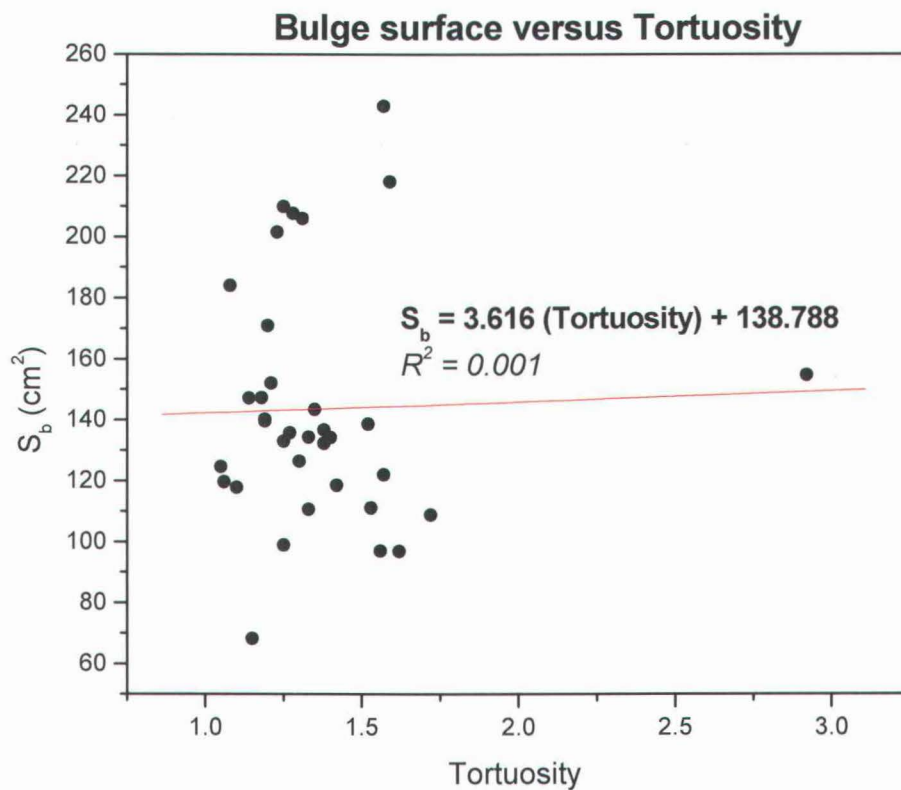


Figure 5.19 Bulge surface area versus tortuosity. These two parameters are not functionally dependent ($R^2 = 0.001 \ll 0.1$).

Figure 5.20 shows a significant correlation between bulge surface area and D/d ratio ($R^2 > 0.1$). According to this plot, generally a lumen with higher D/d ratio has also bigger bulge surface area.

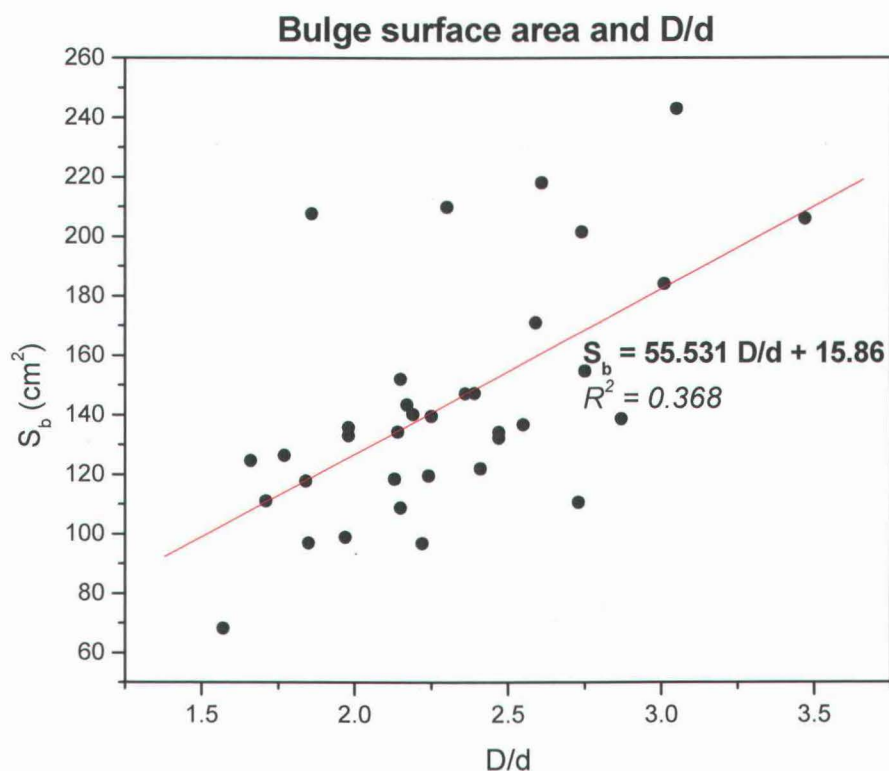


Figure 5.20 A plot of bulge surface area versus D/d . These two parameters are functionally dependent ($R^2 = 0.368 > 0.1$).

In the next 3 plots, correlations between bulge surface area, S_b/S_c , S_b/S_s and thrombus volume for 29 thrombosed patients were graphed (Fig. 5.21, 5.22 and 5.23).

There is a significant dependency between bulge surface area and thrombus volume (Fig. 5.21). Since the slope of the best-fit line is positive, on average any bulge with bigger thrombus volume has also higher surface area.

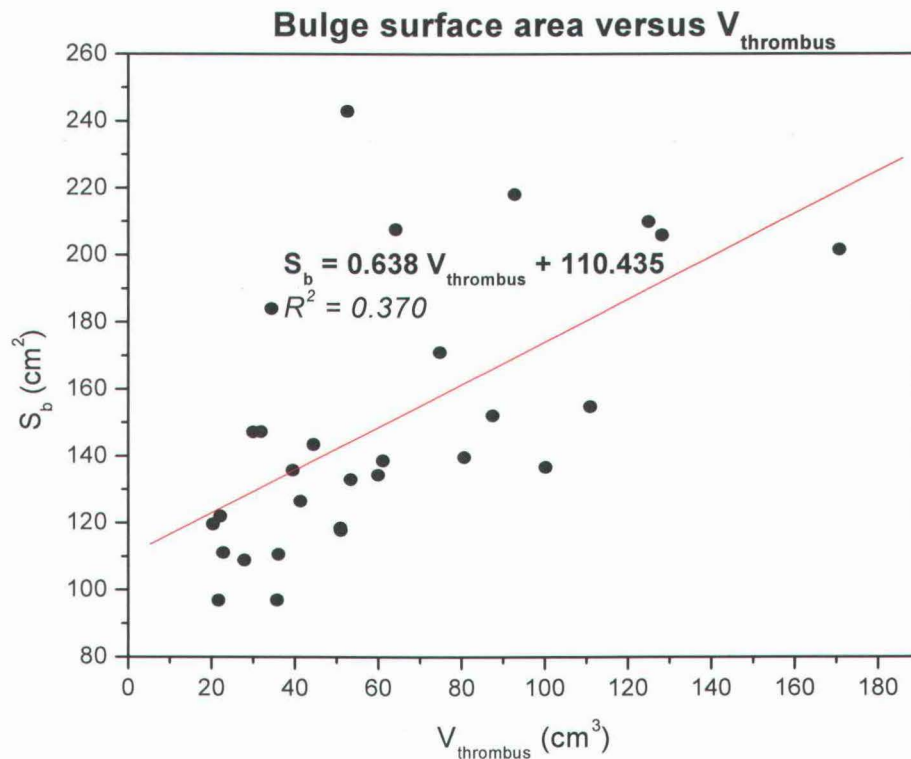


Figure 5.21 There is a significant dependency between bulge surface area and thrombus volume. Since the slope of the best-fit line is positive, bulges with bigger thrombus volume have also higher surface area.

Finally, the ratio of bulge surface to its corresponding cylinder and sphere were displayed in figure 5.22 and 5.23 respectively. The high regression value of figure 5.22 shows a functional dependency between these two parameters. According to this plot, the higher the thrombus volume the lower the similarity of a bulge to cylindrical shape. However, the low regression value of plot 23 shows that there is no significant correlation between these two parameters. Therefore, these two conclusions are consistent with result from figure 5.18.

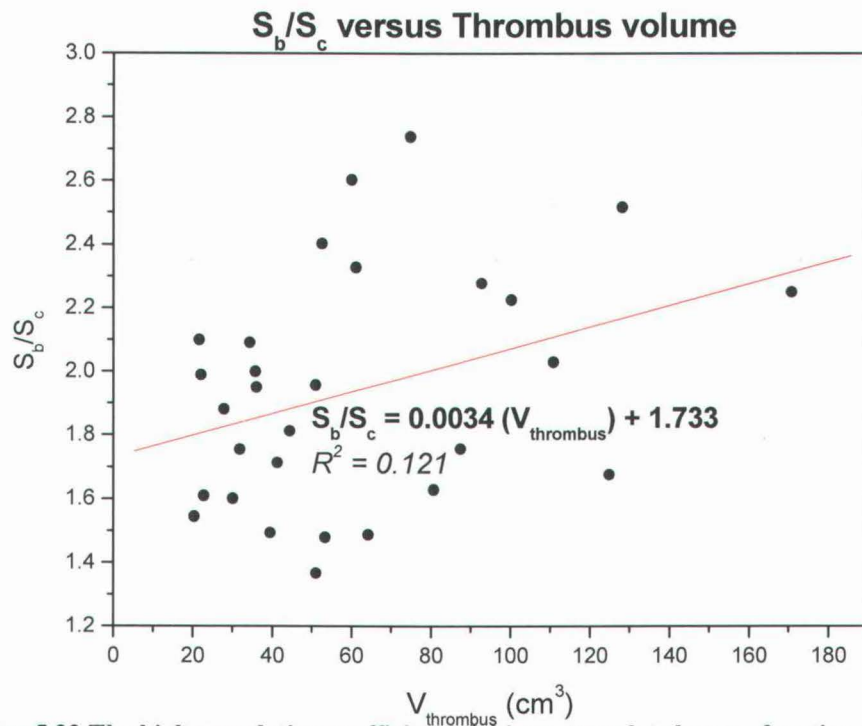


Figure 5.22 The high correlation coefficient of this scatter plot shows a functional dependency between S_b/S_c and thrombus volume. According to this plot the higher the thrombus volume the lower the similarity of a bulge to cylindrical shape.

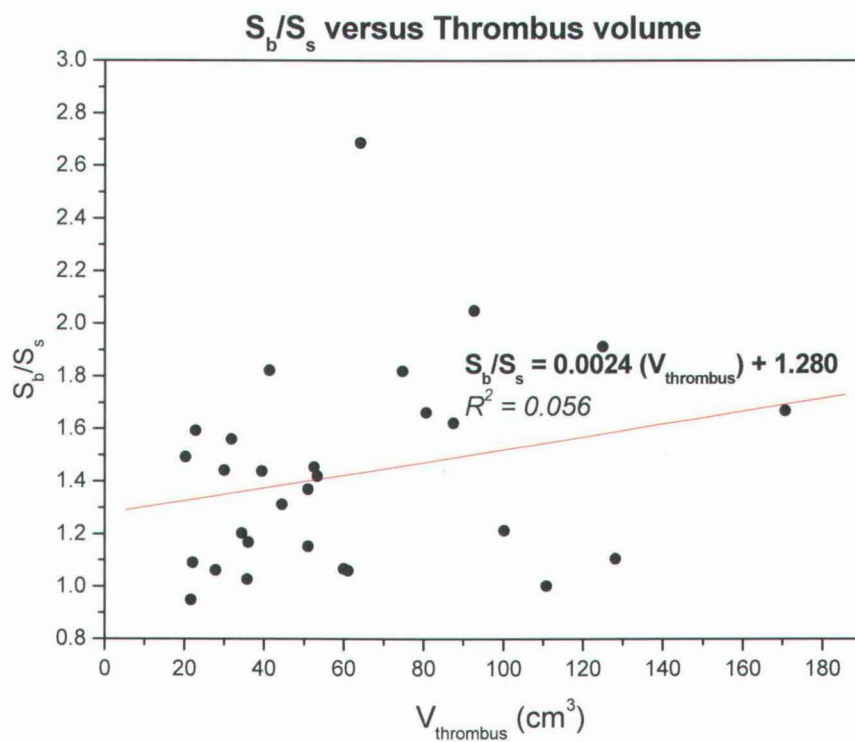


Figure 5.23 The correlation coefficient value of this plot shows no significant correlation between thrombus volume and S_b/S_s .

5.2 AGE SPECIFIC ANALYSIS

5.2.1 Age and Geometric Parameters

In this section, a method was developed to analyze AAA patients based on their ages and geometric parameters, since age is one of the main risk factors in aneurysm rupture [26].

Figure 5.24 shows diameter versus age of 28 patients (23 thrombosed patients, 5 non-thrombosed patients) is shown. (The population of patients in this section is only 28, since age data were available just for this group.). Since R^2 is equal to 0.1 it can be concluded that on average, older AAA patients have larger diameter than younger. The positive slope of the line shows that maximum outer diameter increases with the age of the AAA patients.

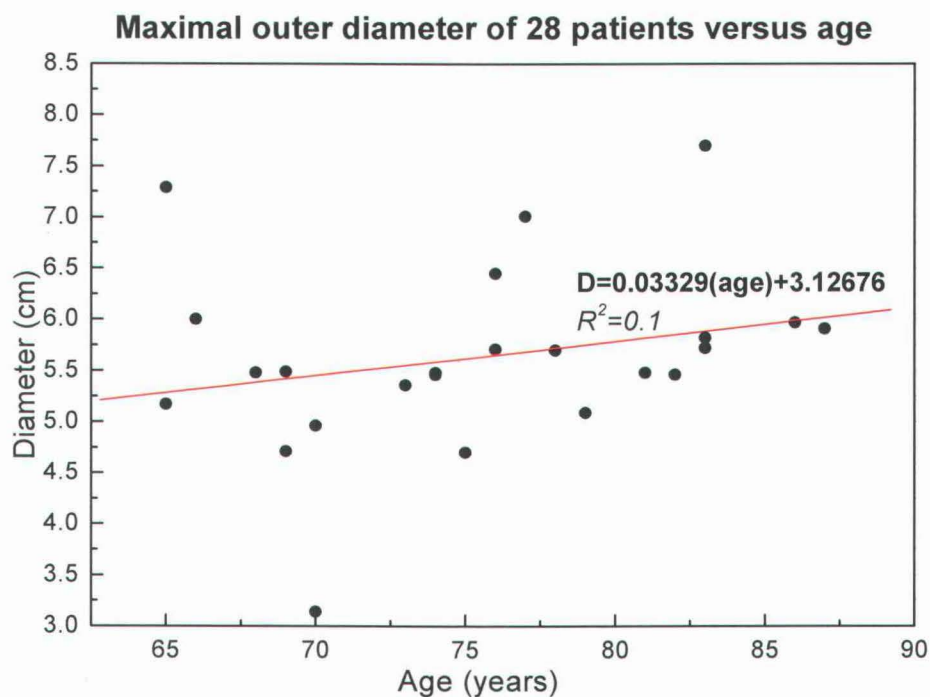


Figure 5.24 Scatter plot of diameter versus age of 28 patients (23 thrombosed patients, 5 non-thrombosed). Since R^2 is equal to 0.1 it can be concluded that on average, older AAA patients have larger diameter than younger. The positive slope of the line shows that maximum outer diameter increases with dependent to the age of the AAA patients.

The last two critical parameters which were evaluated in all groups of AAA patients were tortuosity and vertical curvature. As is shown in figure 5.25, there is no significant correlation between age and tortuosity of bulge ($R^2 = 0.02$).

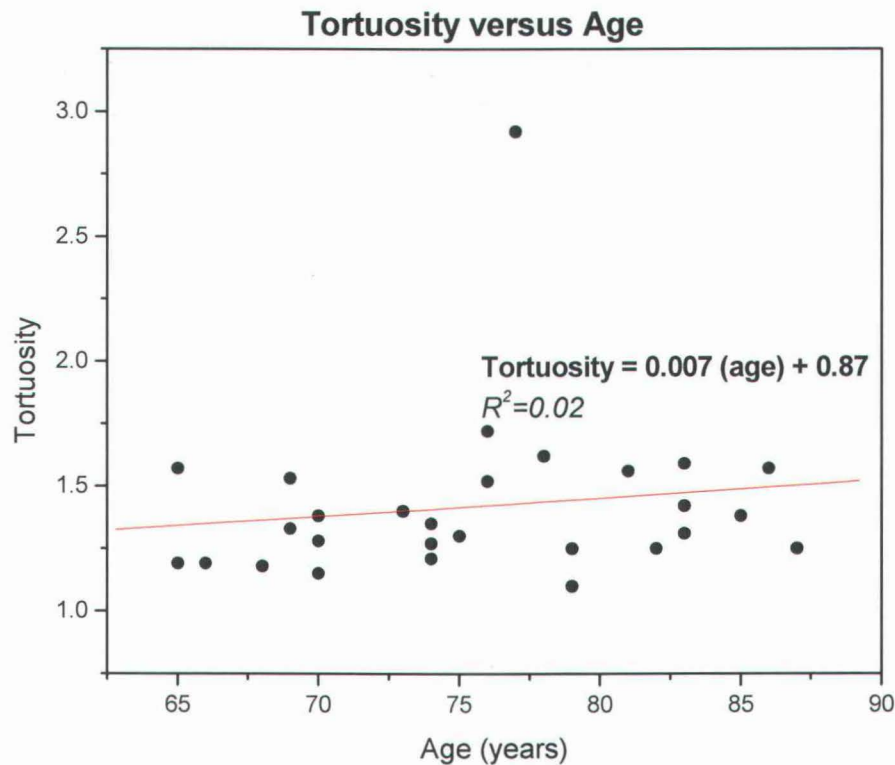


Figure 5.25 Plot of tortuosity versus age. There is no significant correlation between these two parameters of AAA patients ($R^2 < 0.1$).

A plot of vertical curvature versus age is displayed in figure 5.26. These two variables are substantially dependent, since R^2 is equal to 0.1. The positive slope of the best-fit line reveals the correlation between increase of the vertical curvature and age increasing of AAA patients.

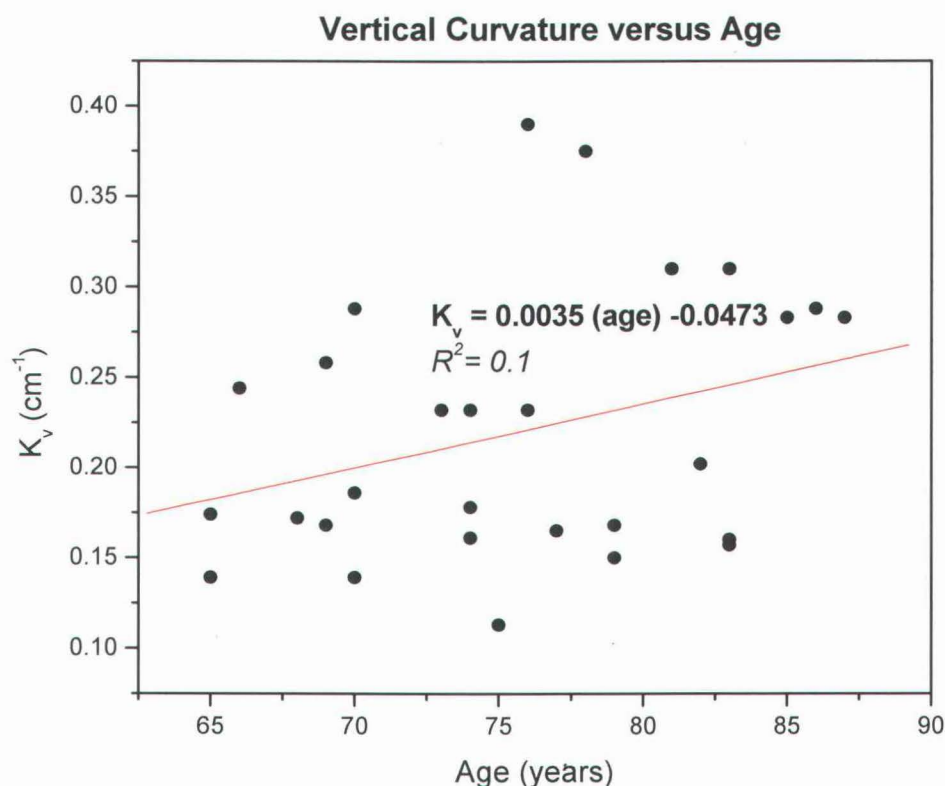


Figure 5.26 Vertical curvature versus age plot was displayed in this figure. These two variables statistically dependent, since R^2 is equal to 0.1. The positive slope of the best-fit line reveals the linear correlation between increase of the vertical curvature and increasing age of AAA patients.

The correlation between thrombus volume and age for 23 thrombosed patients is plotted (Fig. 5.27) along with the best-fit line computed by least squares regression. According to this graph, increasing of age and thrombus formation (volume) are correlated.

This result is completely in agreement with the data of table 4.6, the geometric parameters of the oldest AAA group. In this category, all patients over 80 years old (8 patients) have measurable thrombus deposits in their AAA sacs.

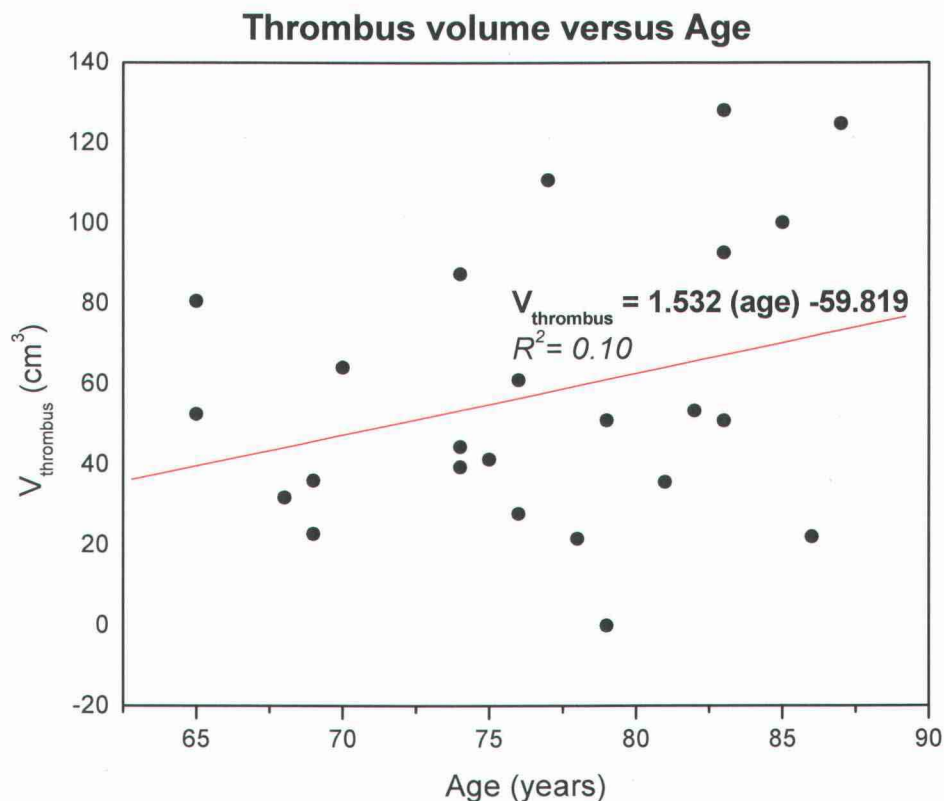


Figure 5.27 Correlation between thrombus volume and age for 23 patients was plotted as a scatter graph along with the best-fit line computed by least squares regression. According to this graph, increasing age and thrombus formation are linearly dependent.

5.2.2 Group Age Analysis

Geometric parameters were also evaluated and compared between different group ages. To find significant differences between each two group ages, the p -value of each two age groups followed by the overall p -value were also calculated through one way ANOVA and Fisher's PLSD tests. In addition to statistical calculation, for some critical geometric parameters bar graphs based on their mean value for each group age were plotted (Fig. 5.28 to 32). The results from these comparisons are as following:

- Maximal diameter (Fig. 5.28): although age group 4 has the maximum mean value of all age groups, there is no significant difference between any two age groups.
- Bulge Length (Fig. 5.29): groups 1 and 3 are significantly different in their AAA lengths ($p = 0.03$). According to this evaluation, patients with age between (65 to 70 years old) have significantly longer bulge length than patients of group 3 (75 to 80 years old).
- Ratio of thrombus volume to AAA volume (Fig. 5.30): groups 1 and 4 are significantly different in their volume ratio ($p = 0.02$). Patients of group age 4 (over 80 years old) have substantially larger $V_{Thrombus} / V_{AAA}$ than group age 1.
- Luminal index (Fig. 5.31): group 1 is significantly different from group 4, since p -value of luminal index between these two groups is less than 0.05 ($p = 0.008$).
- Tortuosity (Fig. 5.32): of all group ages, only groups 1 and 3 are significantly different in their tortuosity ($p = 0.04$).

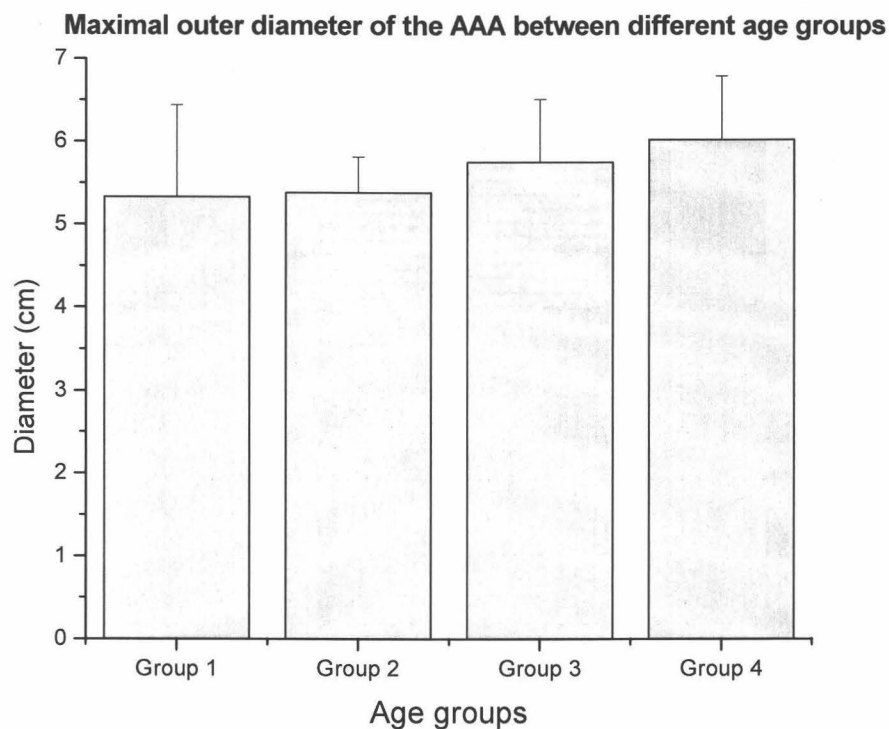


Figure 5.28 Maximal diameter evaluation: although age group 4 seems to have the maximum mean value between all age groups, but there is no significant difference between any two age groups.

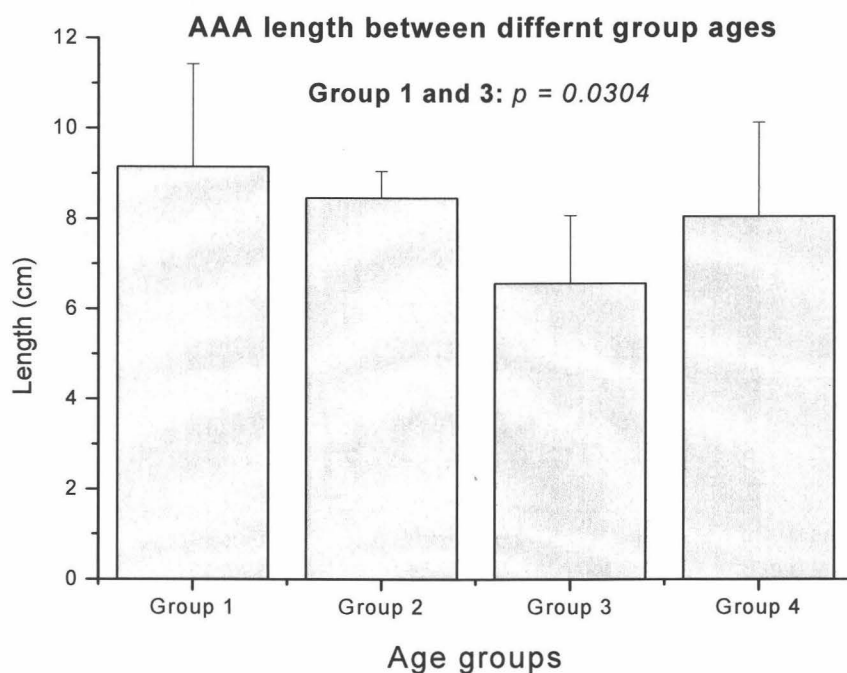


Figure 5.29 Bulge Length: group 1 and 3 are significantly different in their AAA lengths ($p < 0.05$). According to this statistical evaluation, patients with age between (65 to 70 years old) have significantly longer bulge length than patients of group 3 (75 to 80 years old).

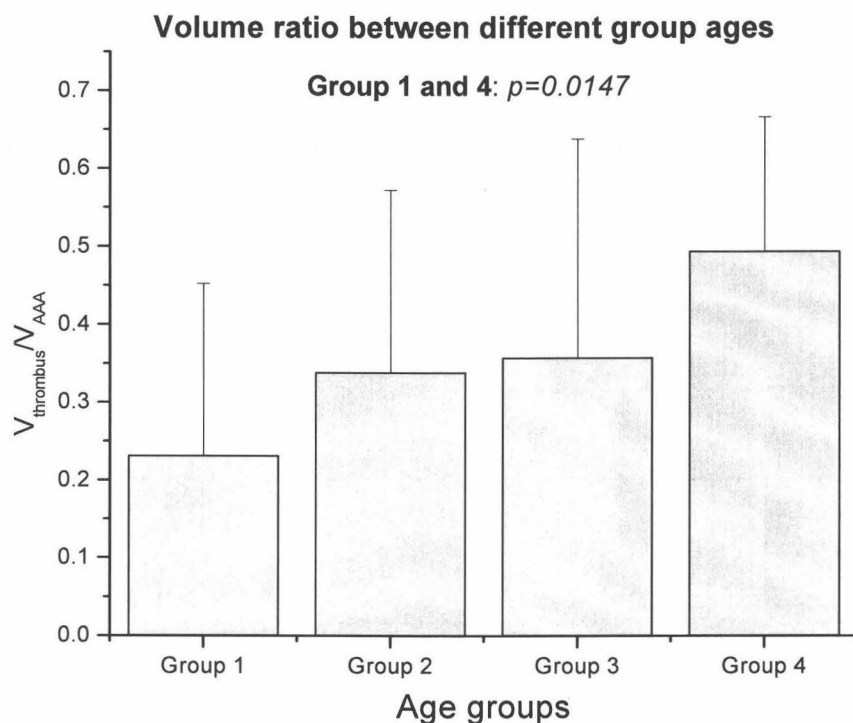


Figure 5.30 Ratio of thrombus volume to AAA volume: group 1 and 4 are significantly different in their volume ratio ($p < 0.05$). Patients of group age 4 (over 80 years old) have substantially larger $V_{\text{Thrombus}} / V_{\text{AAA}}$ than group age 1.

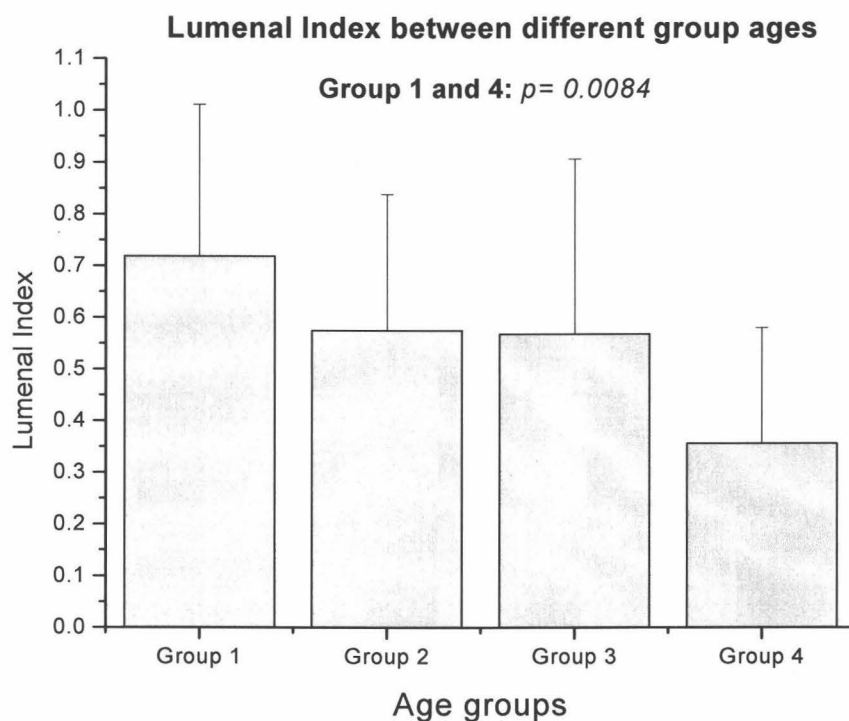


Figure 5.31 Luminal index: group 1 is significantly different from group 4, since p -value of luminal index between these two groups is less than 0.05.

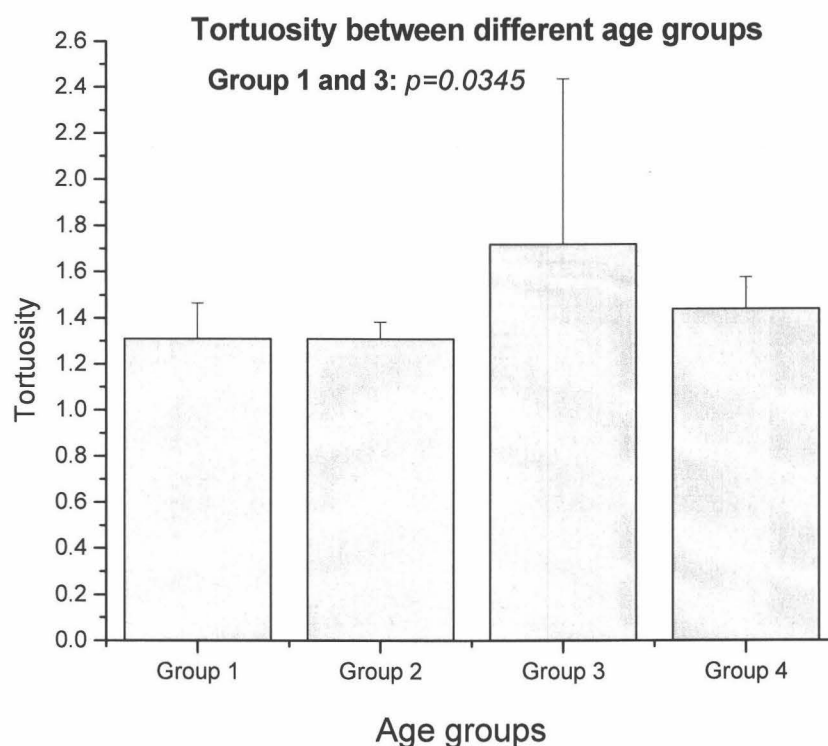


Figure 5.32 Tortuosity: between all group ages, just group 1 and 3 are significantly different in their tortuosity ($p < 0.05$).

5.3 PRESSURE MEASUREMENTS

5.3.1 Pressure Distributions

Wall pressure distributions in the three flow-through phantoms were evaluated at a series of flow rates producing Reynolds numbers of 500, 1000, 1500, 2000, 2500 and 3000.

As one example of the mechanical information provided by these measurements, figure 5.33 presents the pressure distribution in each model at $Re = 500$. In general, wall pressure was nearly constant or declined slightly along the length of the bulge. However, an important exception was observed for model 11, in which the pressure rose by 14 mmHg at the bulge exit from its level in the mid-bulge. In this model, exit pressure, P_5 , therefore exceeded entrance pressure, P_1 , by 13.32, 14.31 and 13.84 mmHg at $Re = 500, 1000, 1500$ respectively (Table 5.5 and appendix F).

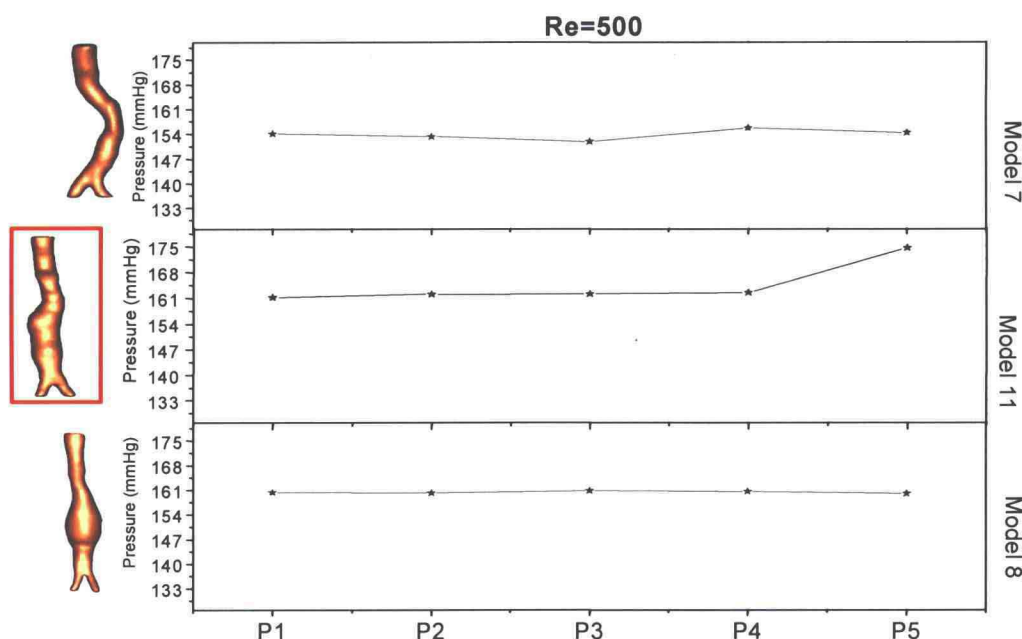


Figure 5.33 Pressure distribution in each model at $Re = 500$ was presented. In general, wall pressure was nearly constant or declined slightly along the length of the bulge. However, an important exception was observed for model 11, in which the pressure rose by nearly 14 mmHg at the bulge exit from its level in the mid-bulge.

Pressure Differences						
	Re = 500	Re =1000	Re =1500	Re = 2000	Re = 2500	Re = 3000
ΔP_{13} (model 8) (mmHg)	-0.430	-0.530	-0.616	-0.516	0.589	-0.027
ΔP_{15} (model 8) (mmHg)	0.465	0.022	0.290	0.269	0.461	-0.251
ΔP_{13} (model 11) (mmHg)	-0.825	-0.546	-0.670	-2.585	-2.615	-2.391
ΔP_{15} (model 11) (mmHg)	-13.32	-14.31	-13.84	-0.439	-0.476	-1.22
ΔP_{13} (model 7) (mmHg)	2.22	0.952	1.11	1.35	0.477	0.162
ΔP_{15} (model 7) (mmHg)	-0.210	0.124	2.20	0.568	-0.139	-0.266

Table 5.5 Pressure differences for three phantoms (models 8, 11 and 7) at various Reynolds numbers.

Since the wall pressure distribution is the physical source of wall stress, this rise can be expected to be of great importance, leading to elevated wall stress and ultimately significantly increased risk of rupture for this particular lesion. Tam, 1976 and Budwig, 1993 suggested that pressure on the aneurysm wall during steady flow is influenced by both geometry and vortex growth and movement within the dilation [32, 33]. However, there is no agreement among all investigators as to how exactly these influences affect pressure. Although according to some previous computational research results, pressure increased through the proximal region of the aneurysm [32, 33, 43], some recent studies and those *in vitro* experiments show pressure actually decreased upon entering an enlarged area [32, 44 and 45]. From the Tam observation, the bulge pressure was lower than pressures directly upstream or downstream of the bulge and the maximum pressure was found in the downstream converting region, not the region of greatest area.

Most of the recent studies focus more on diverging than converging geometries, while diverging flow always results in some flow separation and energy loss [34, 38, 43]. According to biofluid mechanics studies, for simple convergences, turbulence decreases, so energy degradation decreases. However for the aneurysm, this cannot be assumed, since the convergence is directly following a divergence. In Asbury's work, the aneurysm was seen to amplify vorticity as the vorticity lines were stretched by convergence distally [34]. It is unclear how flow in the diverging (proximal) region affects the resulting pressure in the converging (distal) end.

In addition to energy dissipation, Riehle's work suggested that there are other factors affecting pressure patterns: 1) Vortex shifts downstream during laminar flow: This factor is also noted by Asbury *et. al.* (1995) and Budwig *et. al.* (1993) [33, 34]. According to Riehle, this effect is the explanation of the pressure drop along the aneurysm bulge. 2) Vortex grows and moves upstream during turbulent flow: Since turbulence has the three-dimensional effect of expanding the disturbed flow radially [34], the recirculating region grows and moves toward the proximal end of the aneurysm. According to Riehle's study [51] this proximal

migration is one of the factors for explaining the overall model pressure drop (ΔP_{1-5}) and the aneurysm bulge pressure drop (ΔP_{2-4}). 3) Pressure varies radially: Tam's study showed that when there are varies velocities along radial direction, as in a vortex, radial pressure can not be constant [32]. Therefore, fluid equations can not be simplified by eliminating radial pressure elements [51].

However, none of these studies, considered the seemingly minor geometric differences between patient aneurysms which can have major effects on their pressure distribution and thereby on their risk of rupture.

5.4 b. Pressure and Geometric Parameters

In addition to the influence of flow rate, wall pressure is strongly affected by aneurysm size [33, 34], shape, curvature and tortuosity and other geometric parameters, since they can have an important effect in wall stresses generated by steady flow. Riehle's study showed a linear relationship between aneurysm size and pressure difference along the proximal half of the dilation [51]. According to her study the pressure in the AAA bulge is dependent on the divergence angle and overall size of the bulge. Alternatively, larger AAA sacs develop greater turbulence, more shear stress distally, and larger pressure differences while small aneurysms have higher bulge pressure [51].

In the present study, the seemingly minor geometric differences between patient aneurysms which can have major effects on their pressure distribution were considered. In particular, model 11 in which pressure rose by 14 mmHg at the bulge exit on average, had the longest bulge (10.7 cm), largest lesion volume (89.24 cm^3), largest *LI* (0.624), smallest angular deviation (1.70°) between these three phantoms (Fig. 5.34).

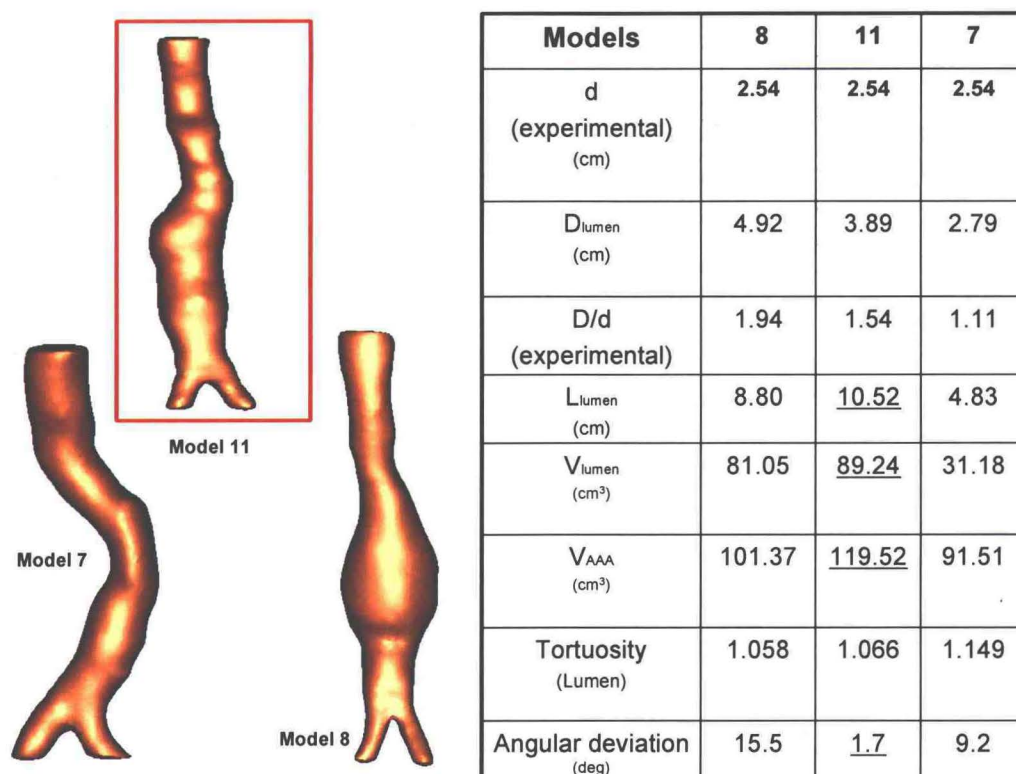


Figure 5.34 Computational models of three flow-through phantoms: In particular, model 11 had the longest bulge (10.7 cm), largest lesion volume (89.24 cm³), largest *LI* (0.624), smallest angular deviation (1.70°) between these three phantoms.

5.4 COMPARISON WITH PREVIOUS STUDIES

Elger *et al.* [12], attempted to study the influence of shape on the stresses in model abdominal aortic aneurysms. His results showed that [12]: 1) Maximum hoop stress typically exceeded maximum meridional stress by a factor of 2 to 3, 2) The shape of an AAA had a small effect on the meridional stresses and a rather dramatic effect on the hoop stresses, 3) Maximum stress typically occurred near the inflection point of a curve drawn coincident with the AAA wall, and 4) the maximum stress was a function--not of the bulge diameter--but of the curvatures (i.e. shape) of the AAA wall. This last result suggested that rupture probability

should be based on wall curvatures, not on AAA bulge diameter. Because curvatures are not much harder to measure than bulge diameter, this concept may be useful in a clinical setting in order to improve prediction of the likelihood of AAA rupture [12].

Fillinger 2004 *et. al.*, analyzed anatomic characteristics of patients with ruptured abdominal aortic aneurysms (AAAs), with conventional two-dimensional computed tomography (CT) [46]. According to this group's results, ruptured AAAs tend to be less tortuous, yet have greater cross-sectional diameter asymmetry. On conventional two-dimensional CT axial sections, it appears that when diameter asymmetry is associated with low aortic tortuosity, the larger diameter on axial sections more accurately reflects rupture risk, and when diameter asymmetry is associated with moderate or severe aortic tortuosity, the smaller diameter on axial sections more accurately reflects rupture risk.

Recently, Sacks *et. al.* presented results from *in vivo* three-dimensional surface geometry of abdominal aortic aneurysms, indicating that AAA surface geometry is highly complex and cannot be simulated by simple axisymmetric models. This suggests an equally complex wall stress distribution [47].

The role intraluminal thrombus (ILT) plays in rupture of AAA is controversial, with studies suggesting it may increase rupture risk, decrease wall stress, and thus, the risk of rupture or have no effect.

Studies suggesting that ILT is protective against rupture by reducing peak wall stress were reported by Mower *et. al.* using computer simulation and by Wang *et. al.* using reconstructed models for three-dimensional AAA geometrics [49,50]. Alternatively, Wolf *et. al.* 1994, concluded that an increased AAA thrombus load is associated with a higher likelihood of rapid expansion and should weigh in favor of early surgical repair [48].

Moreover wall stress, the proximate cause of aneurysm failure, is strongly influenced by the curvature and tortuosity of the aneurysmal bulge as well as by the volume and distribution of deposited thrombus. Hence an accurate knowledge of the magnitude of these differences can be expected to provide critical support for a biomechanical understanding of the process of rupture.

5.5 CLINICAL SIGNIFICANCE

Presently the only crucial criterion for most aneurysm management is the bulge diameter, since any abdominal aorta that exceeds at least 3.0 cm is considered as an aneurysm. We tested correlations between dilation volume and other geometric parameters. Finding these correlations is critical in an effort to improve on the limitations of the use of AAA diameter as the only factor in assessing risk of rupture.

In this study it was found that AAAs differ significantly in their geometric parameters. AAAs can be categorized based on having measurable thrombi and not having thrombi. Based on this distinction, AAAs with measurable thrombi have larger bulge diameters but less lumen diameters and horizontal curvatures than patients without thrombus.

According to our evaluations, aneurysm volume has significant correlations with D/d , length, bulge surface, thrombus volume if present and age. In addition to that, for thrombosed patients, thrombosed volume is significantly associated with luminal index, D/d , non-dilated diameter of lumen, bulge surface area, bulge shape and age. Therefore an aneurysm with larger values of these parameters may have a clinically poorer prognosis than one of similar bulge diameter with smaller mentioned parameters.

Our pressure measurements showed that net pressure rises with strong peaks are possible for aneurysms with particularly susceptible shapes. For model 11, pressure rose substantially from the bulge entrance to its exit. Since this model had the longest bulge between these three phantoms, one possible conclusion is that longer aneurysms are at a greater risk of rupture than shorter ones. This phenomenon also agreed with the hypothesis that, longer aneurysms may have increased rupture risk than shorter ones with similar D/d , due to more vortex formation and energy dissipation.

This rise may also explain why clinical studies disagree on a usual rupture point for aneurysms, some occurring in the distal region, while others at other points along the bulge [23, 19, 17].

CHAPTER 6: CONCLUSION

6.1 SUMMARY OF MOST IMPORTANT FINDINGS

The general goal of this study is to characterize a series of patient aneurysms based on their geometric parameters, wall pressure distributions and ages, since correlations between any of these parameters can affect wall stress and thereby alter rupture risk

In this study, the geometric properties of 35 AAAs were measured and compared. Computational models of a series of real patient AAAs were constructed and analyzed from abdominal CT series using specific software (*MIMICS*, Materialise Inc.; *CFD-GEOM*, CFD Research Corp.; *AutoCAD*, Autodesk Inc.). AAA geometric parameters were then directly measured from the models. Finally, once satisfactory computational AAA models had been created, wall pressure magnitude and distribution were evaluated under steady flow conditions in three sample phantoms constructed from the models. The following conclusions can be drawn from these measurements:

1. AAA patients can be categorized into two groups, those without thrombus and those presenting measurable thrombus deposits: AAAs with measurable thrombi have larger bulge diameters but less lumen diameters and horizontal curvatures than patients without thrombus.
2. To assess geometric characteristics of AAA patients, the correlation between some related parameters were also discussed:
 - a. Longer AAAs have also larger volume.
 - b. On average, bulges with larger diameter have higher tortuosity.
 - c. Generally, as the horizontal curvature of a bulge decreases, its tortuosity increases.
 - d. On average, bulges with higher LI have also higher $V_{thrombus} / V_{AAA}$.
 - e. There is a significant relationship between thrombus volume and D/d ratio.

- f. Any lumen with bigger non-dilated diameter generally has smaller thrombus volume within its AAA sac.
3. The bulge shape of patients with thrombus is significantly more similar to a sphere than a cylinder.
 4. Bulge surface similarity parameters were also evaluated based on finding their correlations with geometric parameters:
 - a. Generally, a lumen with higher D/d ratio has also bigger bulge surface area.
 - b. There is a significant dependency between bulge surface area and thrombus volume.
 5. Maximum outer diameter, vertical curvature and thrombus volume is linearly dependent to the age of the AAA patients.
 6. Geometric parameters were also evaluated and compared between different group ages: Patients of group age 4 (over 80 years old) have substantially larger $V_{thrombus} / V_{AAA}$ than age group 1.
 7. In general, wall pressure was nearly constant or declined slightly along the length of the bulge. However, an important exception was observed for model 11, in which the pressure rose by averagely 14 mmHg at the bulge exit from its level in the mid-bulge.
 8. In addition to the influence of flow rate, wall pressure is strongly affected by aneurysm size, shape and other geometric parameters such as length, angular deviation or lumenal index.

6.2 FUTURE DIRECTIONS

Since in this study patient population is one of the primary elements for evaluating and categorizing AAA models, having more patients might have substantial effect on the results. In this case, for instance higher patient population may change some insignificant correlations, to significant dependency. Also having follow up patients and evaluating geometric parameters between them can influence the results and their correlation to rupture risk.

Additionally, a more accurate system for measuring average vertical curvature (i.e. the arc function which can fit on the whole of the bulge surface) could influence the evaluation of this parameter and its correlation to rupture risk.

For experimental pressure study several areas can be targeted for future work since this study investigated in rigid AAA models without any iliac bifurcation and under steady state conditions: 1) Studies into pressure measurement can be conducted in elastic models, since *in vivo* blood vessels are naturally elastic. 2) A flow system that models the downstream iliac bifurcation should be used, since the bifurcation could affect the flow and pressure patterns. 3) A more physiologically matched exercise flow waveform and experimental configuration could be used to study the differences in pressure between resting condition and higher energy states (pulsatile flow). Finally, a computational fluid dynamic model of the present work would enable a comparison between *in vitro* and computational experiments.

BIBLIOGRAPHY

1. Szilagyi, D.E., Elliot, J.P. and Smith, R.F., "Clinical fate of the patient with asymptomatic abdominal aortic aneurysm and unfit for surgical treatment." *Arch. Surg.* 104, 600-6, 1972.
2. Cronenwett, J.L., Murphy, T.F., Zelenock, G.B., Whitehouse, W.M., Jr, Lindenauer, S.M., Graham, L.M., et al., "Actuarial analysis of variables associated with rupture of small abdominal aortic aneurysms." *Surgery* 98, 472-83, 1985.
3. Nicholls, S.C., Gardner, J.B., Meissner, M.H. and Johansen, H.K., "Rupture in small abdominal aortic aneurysm." *J. Vasc. Surg.* 28, 884-8, 1998.
4. Darling, R.C., Messina, C.R., Brewster, D.C. and Ottinger, L.W., "Autopsy study of unoperated abdominal aortic aneurysms. The case for early resection." *Circulation* 56 (3 Suppl) II, 161-4, 1977.
5. Fillinger, M.F., Raghavan, M.L., Marra, S.P., Cronenwett, J.L. and Kennedy, F.E., "In vivo analysis of mechanical wall stress and abdominal aortic aneurysm rupture risk." *J. Vasc. Surg.* 36, 589-97, 2002.
6. Fillinger, M.F., Marra, S.P., Raghavan, M.L. and Kennedy, F.E., "Prediction of rupture in abdominal aortic aneurysm during observation: wall stress versus diameter." *J. Vasc. Surg.* 37, 724-32, 2003.
7. Inzoli, F., Boschetti, F., Zappa, M., Longo T. and Fumero R., "Biomechanical factors in abdominal aortic aneurysm rupture." *Eur. J. Vasc. Surg.* 7, 667-74, 1993.
8. Mower, W.R., Quinones, W.J. and Gambhir, S.S., "Effect of intraluminal thrombus on abdominal aortic aneurysm wall stress." *J. Vasc. Surg.* 26, 602-8, 1997.
9. Vorp, D.A., Raghavan, M.L. and Webster, M.W., "Mechanical wall stress in abdominal aortic aneurysm. Influence of diameter and asymmetry." *J. Vasc. Surg.* 27, 632-9 1998.
10. DiMartino, E., Mantero, S., Inzoli, F., Melissano, G., Astore, D., Chiesa, R., "Biomechanics of abdominal aortic aneurysm in presence of endoluminal thrombus. Experimental characteristic and structural state constitutional analysis." *J. Vasc. Endovasc. Surg.* 15, 290-9, 1998.
11. Raghavan, M.L., Vorp, D.A., Federle, M.P., Makaroun, M.S. and Webster, M.W., "Wall stress distribution on three-dimensionally reconstructed models of human abdominal aortic aneurysm." *J. Vasc. Surg.* 31, 760-9, 2000.

12. Elger, D. F., Blacketter, D.M., Budwig, R.S. and Johansen K.H., "The influence of shape on the stress in model abdominal aortic aneurysms," *J. Biomed. Eng.* 118, 326-332, 1996.
13. Stringfellow, M.M., Lawrence, P.F. and stringfellow, R.G., "The influence of aorta aneurysm geometry upon stress in the aneurysm wall," *J. Surg. Res.* 42, 425-433, 1987.
14. Silver, M.D., *Cardiovascular Pathology.*, Churchill Livingstone, New York, 1983.
15. Kaiser, F.E., Morley, J.E., Coe, R.M., *Cardiovascular Disease in Older People.*, Springer Publishing Company, New York, 1997.
16. Liddington, M.I. and Heather, B.M., "The relationship between aortic diameter and body habitus," *European Journal of Vascular Surgery*, 6, 619-642, 1992.
17. Fine, L.G., "Abdominal aortic aneurysm. Report of a meeting of physicians and scientists," University College London Medical School [Clinical Conference], *Lancet*, 341, 215-220, 1993.
18. Van De Graaff, K.M., *Human Anatomy.*, McGraw-Hill. 6th Ed., New York, 2002.
19. Estes, J.E., "Abdominal aortic aneurysm: A study of one hundred and tow cases," *Circulation*, 2, 258, 1950.
20. Repot of U. S. Preventive Services Task Force, *Guide to clinical preventive services.* 2nd Ed., Wiliams & Wikins, Baltimore, 1996.
21. Junqueira, L.C. and Carneiro, J., *Human Anatomy.*, McGraw-Hill. 10th Ed., New York, 2003.
22. Cooley, D.A., *Surgical Treatment of aortic aneurysms.*, W.B. Saunders Company, Philadelphia, 1986.
23. Darling, R.C., Messina, C.R., Brewster, D.C. and Ottinger, L.W., "Autopsy study of unoperated abdominal aortic aneurysms. The case for early resection." *Circulation* 56 (3 Suppl) II, 161-4, 1977.

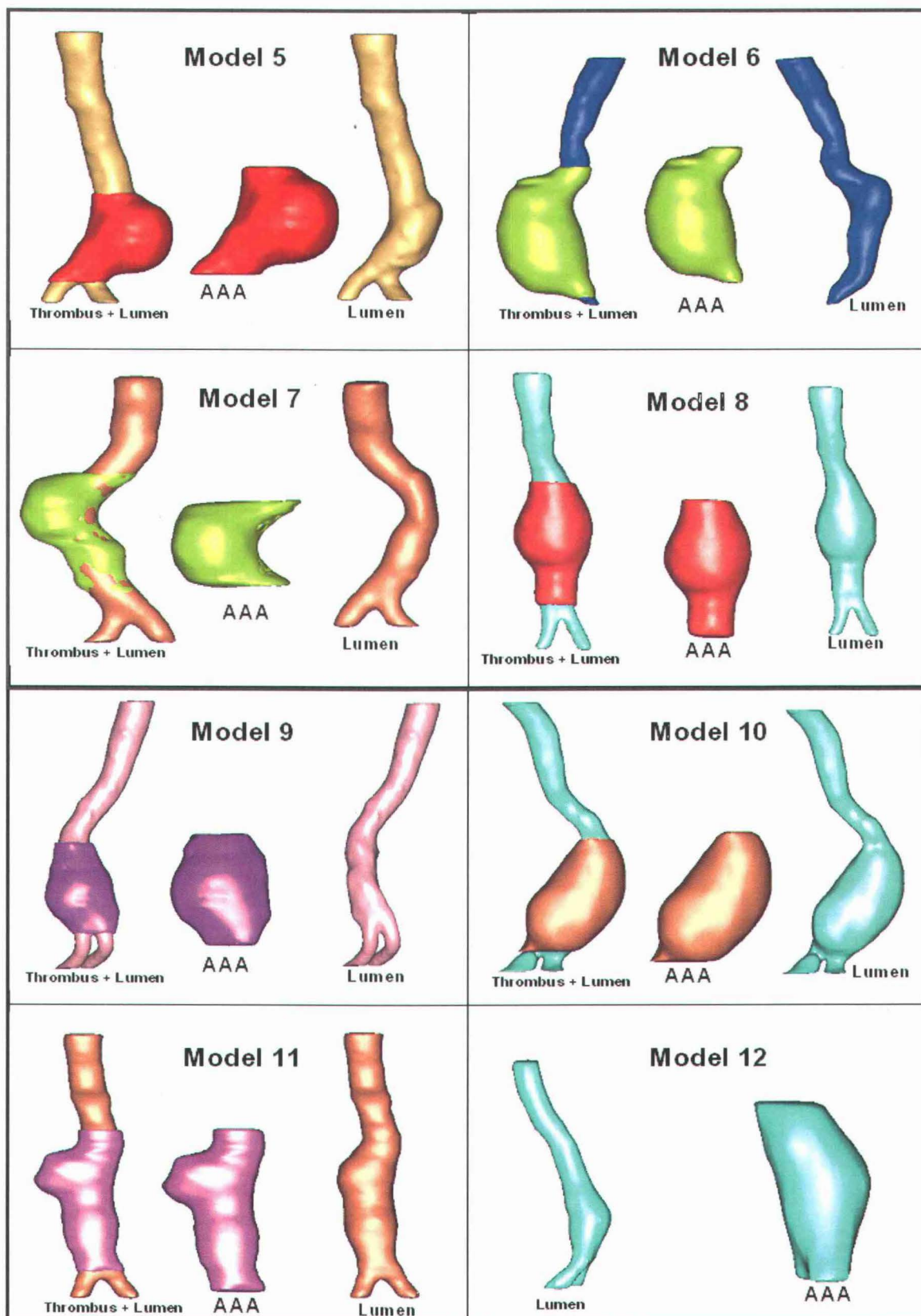
24. Bernstein, E.F., Dilley, R.B., Goldberger, L.E., et. al., "Growth rate of small abdominal aortic aneurysms," *Surgery* 80, 765-773, 1976.
25. MacSweeney, S.T., Ellis, M., Worrell, P.C., Greenhalgh, R.M., & Powell, J.T., "Smoking and growth rate of small abdominal aortic aneurysms." *Lancet* 344, 651- 652, 1994.
26. Yao, J.S.T., Pearce, W.H., *Aneurysms: New Findings and Treatments.*, Appleton & Lange, Norwalk, Connecticut 1994.
27. Johansen, K., "Aneurysms," *J. Scientific American*, 247, 110-122, 1982.
28. Bluth, E.I., Murphy, S.M., Hollier, L.H., Sullivan, M.A., "Color Flow Doppler in the Evaluation of Aortic Aneurysms," *International Angiology*, 9, 9-10, 1990.
29. Fung, Y.-C., *Biomechanics: Mechanical Properties of Living Tissues*. 2nd Ed., Springer-Verlag, New York, 1981.
30. Clingan, P.A., Friedman, M.H., "The Effect of Celiac and Renal Artery Outflows on Near-Wall Velocities in the Porcine Iliac Arteries," *J Biomedical Engineering Society* 28, 302-308, 2000.
31. Scherer P.W., "Flow in Axisymmetrical Glass Model Aneurysms," *J Biomech.* 6, 995-700, 1973.
32. Tam, M.K., Melbin, J., and Knight, D.H., "Hemodynamic Phenomena in Fusiform Aneurysms—I: Steady Flow Conditions," *IEEE Transaction of Biomedical Engineering*, BMES, 23(6), 453-459, 1976.
33. Budwig, R., Elger, D., Hooper, H. and Slippey, J., "Steady flow in abdominal aortic aneurysm models", *J. Biomech.* 115, 1319-1329, 1999.
34. Asbury, C. L., Ruberti, J. W., Bluth, E.I. and Peattie, R. A., "Experimental investigation of steady flow in rigid models of abdominal aortic aneurysms", *J. Ann. Biomed. Eng.* 23, 29-39, 1995.
35. Peattie, R. A., Asbury, C. L., Bluth, E. I. and Ruberti, J. W., "Steady flow in models of abdominal aortic aneurysms. PartI: Investigation of the velocity patterns," *J. Ultrasound. Med.* 15, 679-688, 1996.

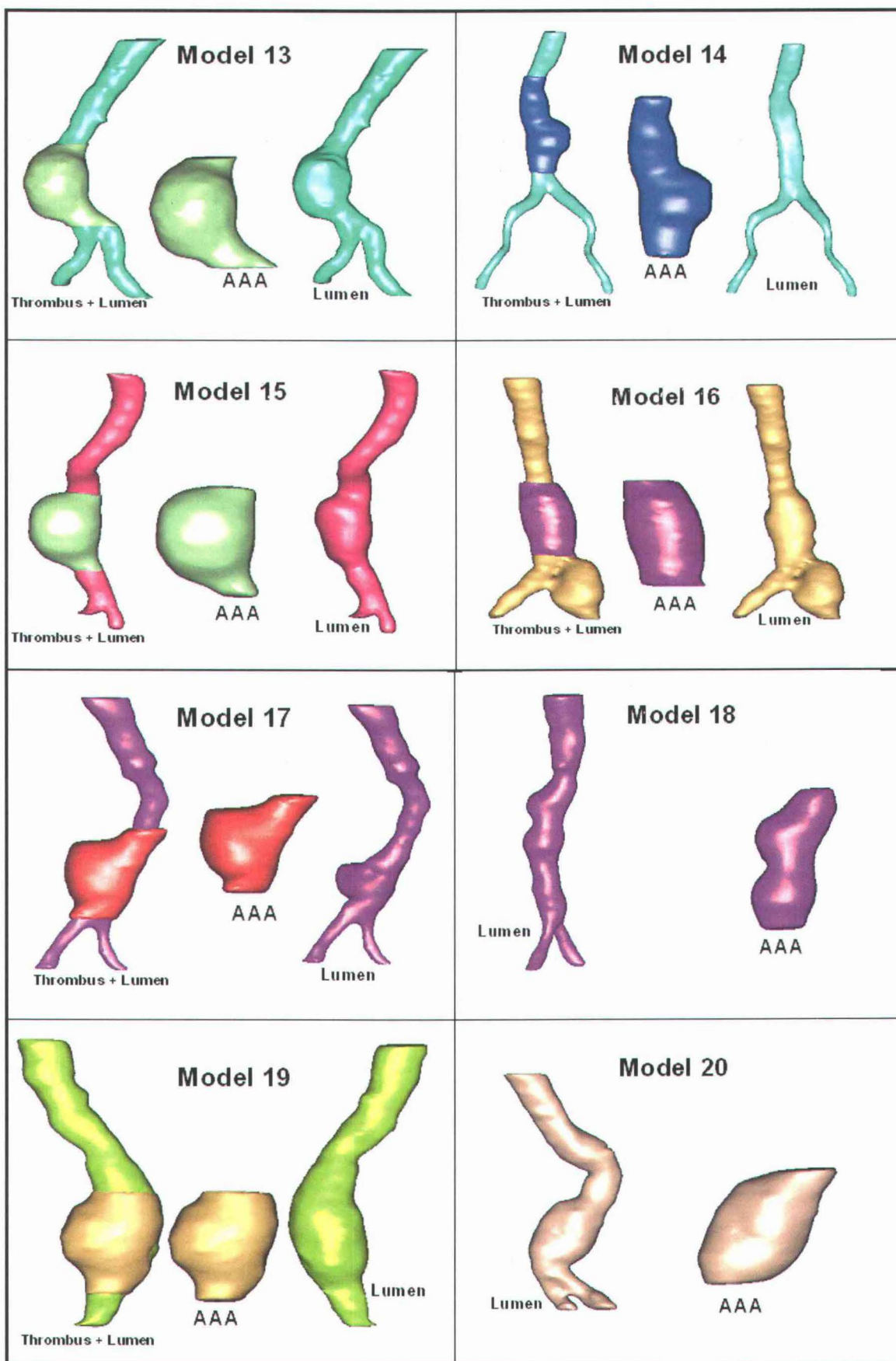
36. Peattie, R. A., Asbury, C. L., Bluth, E. I. and Ruberti, J. W., "Steady flow in model of abdominal aortic aneurysms. PartII: Wall stresses and their implication for in vivo thrombosis and rupture," *J. Ultrasound. Med.* 15, 689-696, 1996.
37. Peattie, R.A., Riehle, T.J. and Bluth, E.L., "Pulsatile flow in fusiform models of abdominal aortic aneurysms: Flow fields, velocity patterns and flow-induced wall stresses," *J. Biomech. Eng.* 126, 438-446, 2004.
38. Budwig, R., Elger, D., Hooper, H. and Slippery, J., "Steady flow in abdominal aortic aneurysm models", *J. Biomech.* 116, 418-423, 1993.
39. Egelhoff, C.J., Budwig, R.S., Elger, D.F., Khraishi, T.A., Johansen, K.H., "Model studies of the flow in abdominal aortic aneurysms during resting and exercise conditions," *J. Biomech. Eng.* 32, 1319-1329, 1999.
40. Bluestein, D., Niu, L., Schoephoerster, R.T. and Dewanjee, M. K., "Steady flow in an aneurysm model: Correlation between fluid dynamics and blood platelet deposition", *J. Biomech. Eng.* 118, 280-286, 1996.
41. Atkinson, S.J., Feller, K.J., Peattie, R.A., "Measurement of fluid flow patterns and wall shear-stresses in patient-based models of abdominal aortic aneurysms," *ASME. Bioengineering conference* 50, 2001.
42. Fung, Y.-C., *Biomechanics: Circulation*. 2nd Ed., Springer-Verlag, New York, 1981.
43. Taylor, T.W. and Yamaguchi, T., "Three-dimensional simulation of blood flow in an abdominal aortic aneurysm-steady and unsteady flow cases," *J. Biomech. Eng.* 116, 89-98, 1993.
44. Forrester, J.H., D.F. Young, "Flow through a Converging-Diverging tube and its implications in occlusive vascular disease-II: Theoretical and Experimental Results and Their Implications," *J. Biomech.* 3, 307-316, 1970.
45. Robicsek, F., W. Tam, H.K. Daugherty, D.C. Mullen, "The applicability of Bernoulli's Law in the process of enlargement and rupture of aortic aneurysms," *J. of Thoracic Cardiovascular Surgery*, 61, 472-475, 1971.

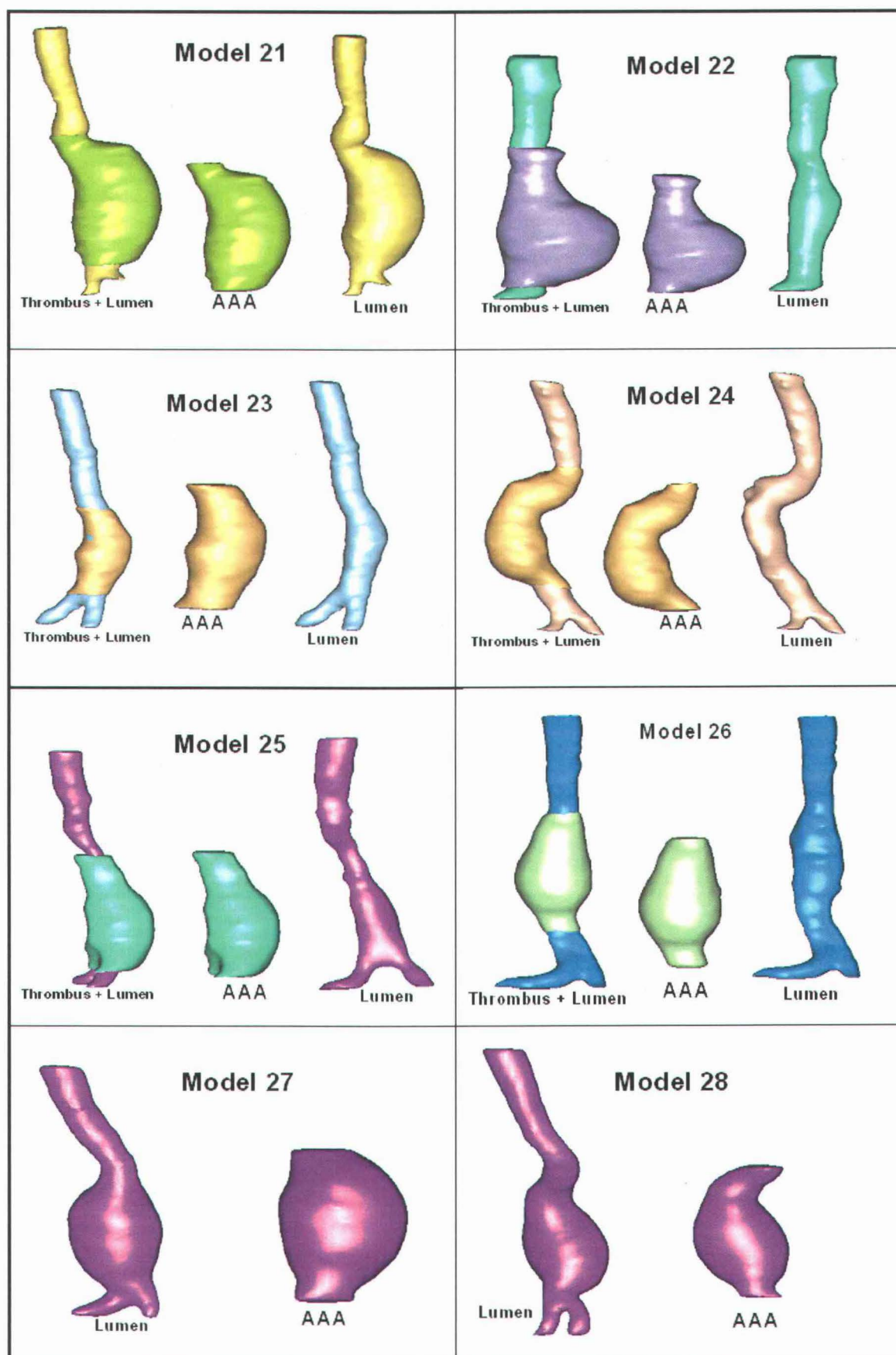
46. Fillinger, M.F., Racusin, J., Baker R.K., Cronenwett, J.L., Teuterlink, A., Schermerhorn, M.L., Zwolak, R.M., Powell, R.J., Walsh, D.B., Rzucidlo, E.M., "Anatomic characteristic of ruptured abdominal aortic aneurysm on conventional CT scans: Implications for rupture risk" *J. Vasc. Surg.* 39, 1243-52, 2004.
47. Sacks, M.S., Vorp, D.A., Raghavan, M.L., Federle, M.P. and Webster M.W. "In vivo three-dimensional surface geometry of abdominal aortic aneurysms." *J. Ann. Biomed. Eng.* 27, 469-479 1999.
48. Wolf Y.G., Thomas, W.S., Brennan F.J., Goff, W.G., Sise, M.J. and Bernstein E.F. "Computed tomography scanning findings associated with rapid expansion of abdominal aortic aneurysms" *J. Vasc. Surg.* 20, 529-38, 1994.
49. Mower, W.R., Quinones W.J., Gambhir, S.S., "Effect of intraluminal thrombus on abdominal aortic aneurysm wall stress." *J. Vasc. Surg.* 26, 602-8, 1997.
50. Wang D.H.J., Makaroun M.S., Webster M.W. and Vorp, D.A., "Effect of Intraluminal thrombus on wall stress in patient-specific models of abdominal aortic aneurysm." *J. Vasc. Surg.* 36, 598-604, 2002.
51. Riehle T. J., "Experimental investigation of wall pressure in rigid models of abdominal aortic aneurysms," M.S.E. Thesis, Dept. of Biomedical Engineering, Tulane University, New Orleans, 1997.

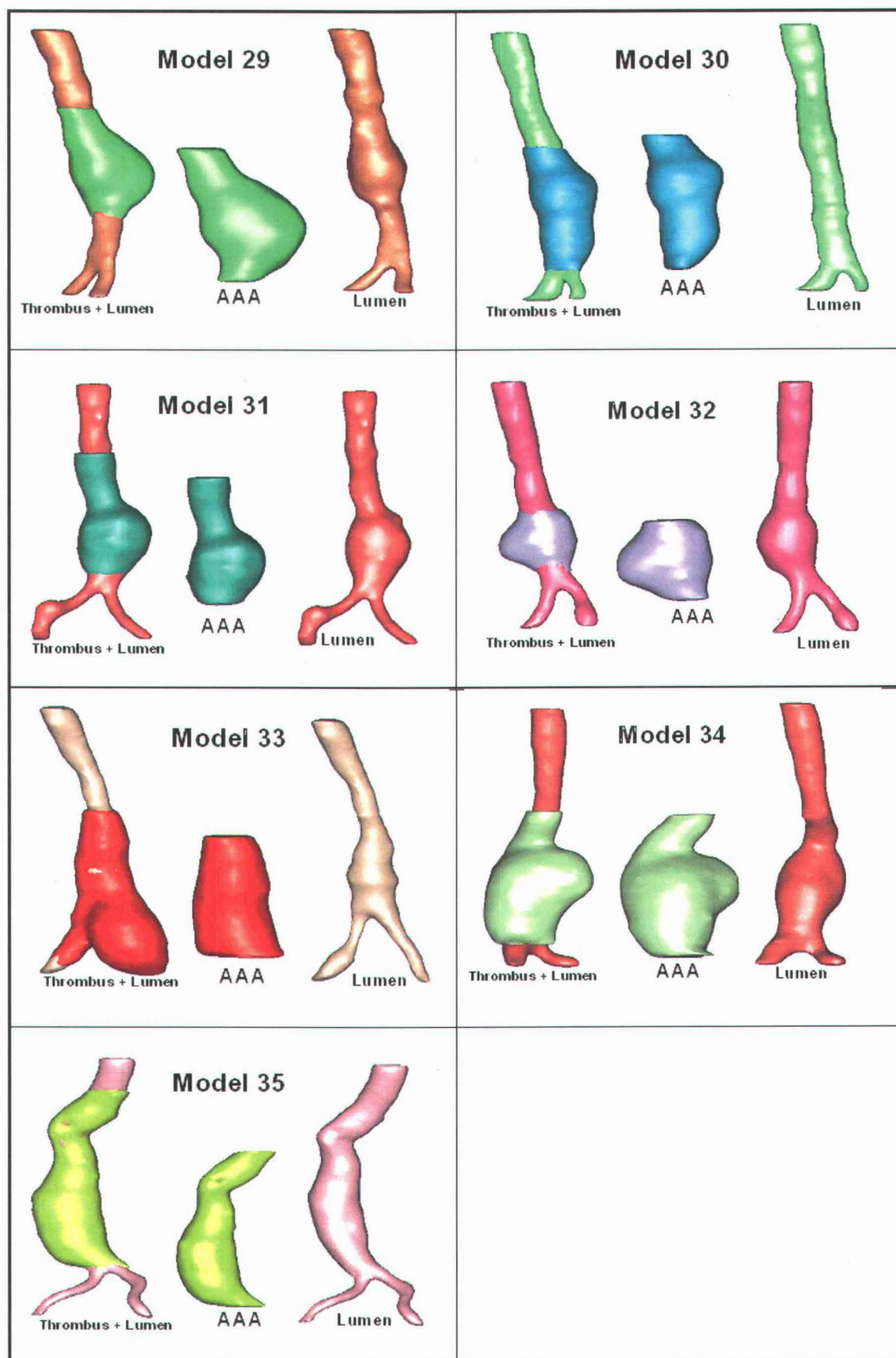
APPENDIX A: 3D REPRESENTATION OF 35 AAA PATIENTS

3D representations of 35 AAA patients



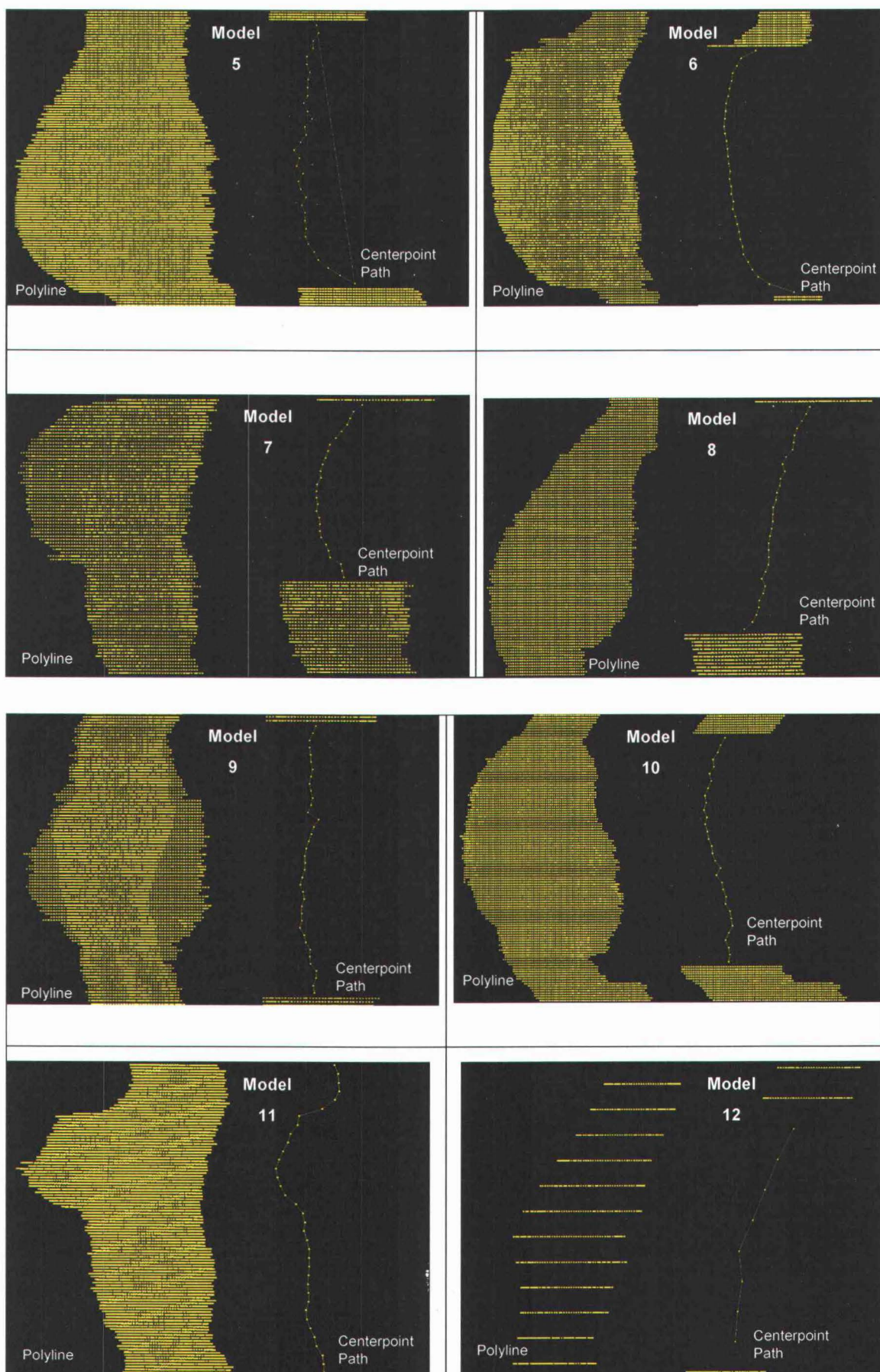


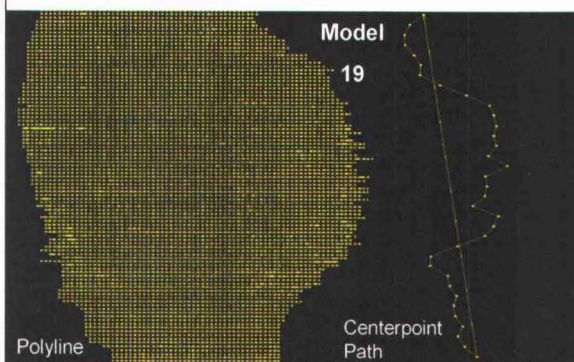
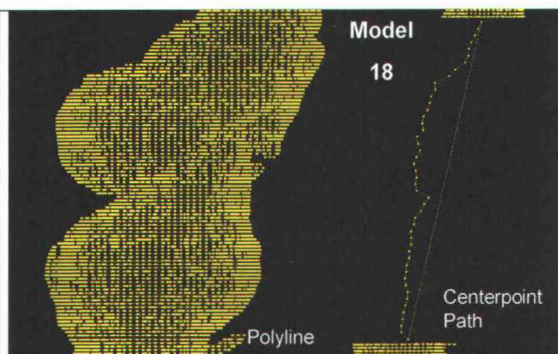
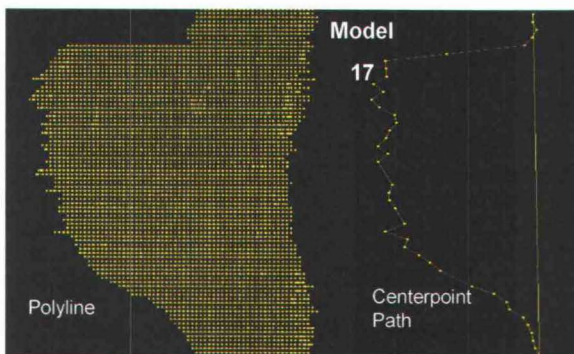
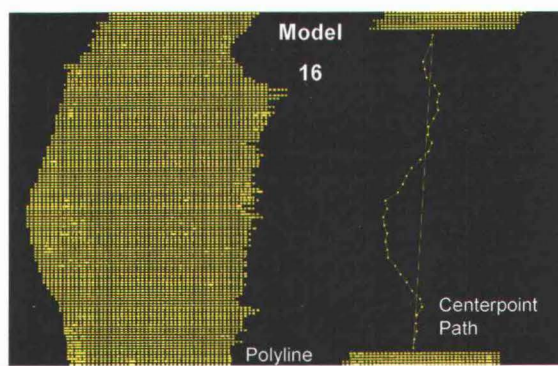
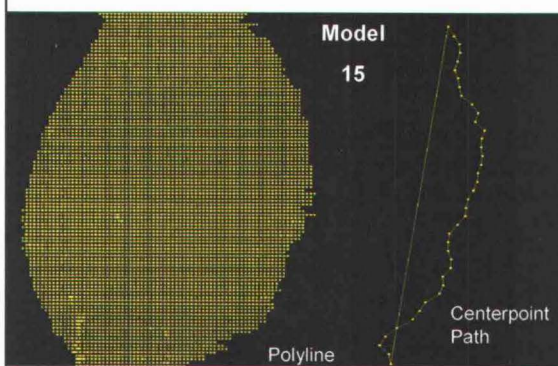
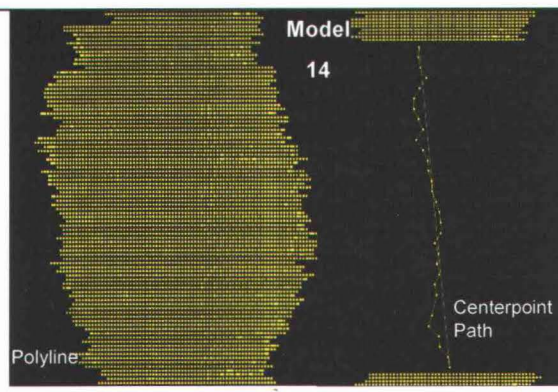
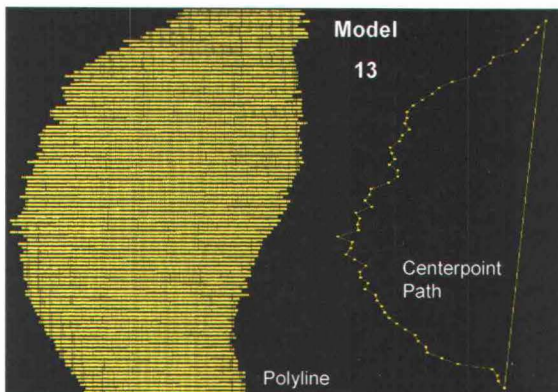


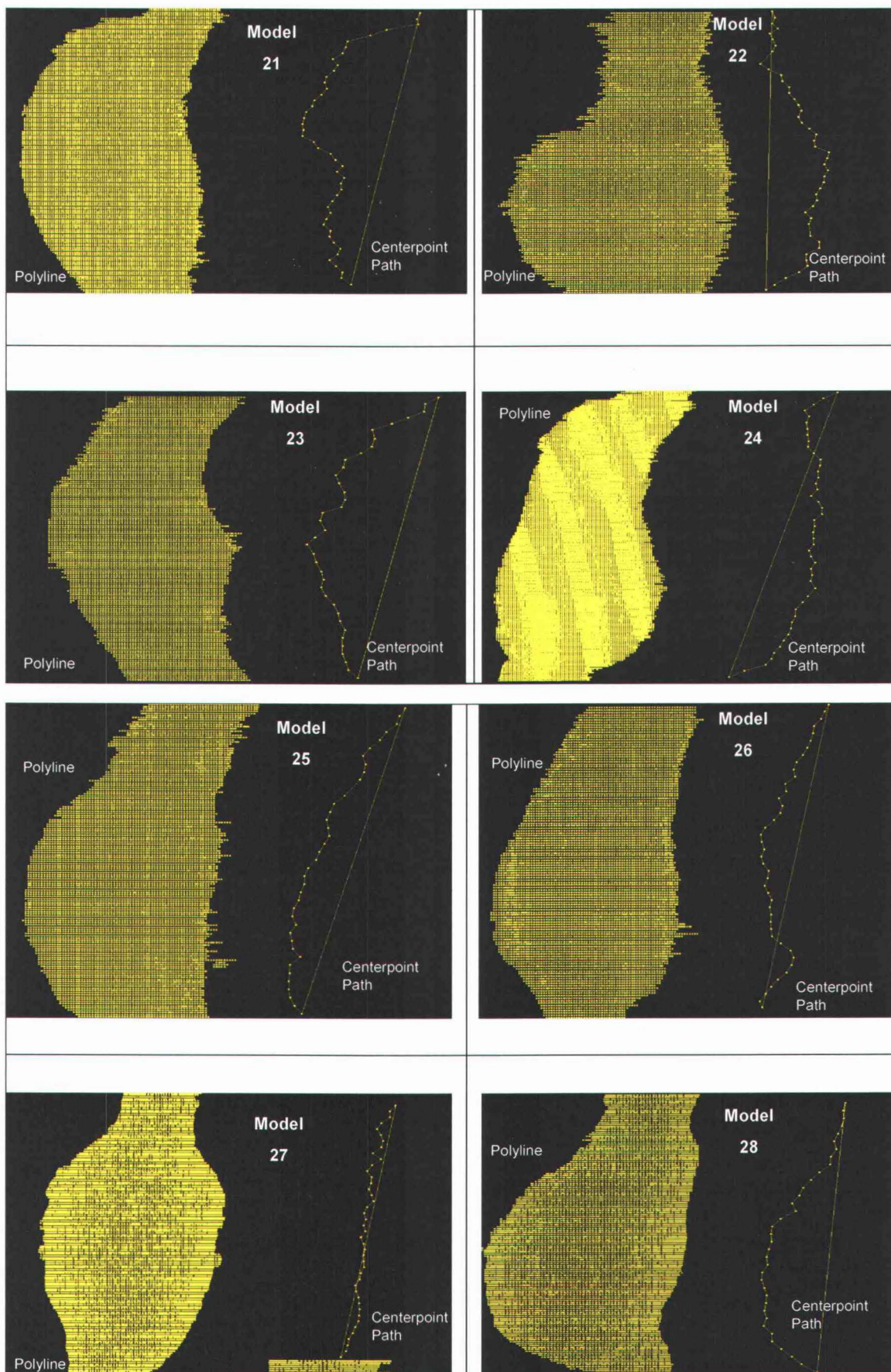


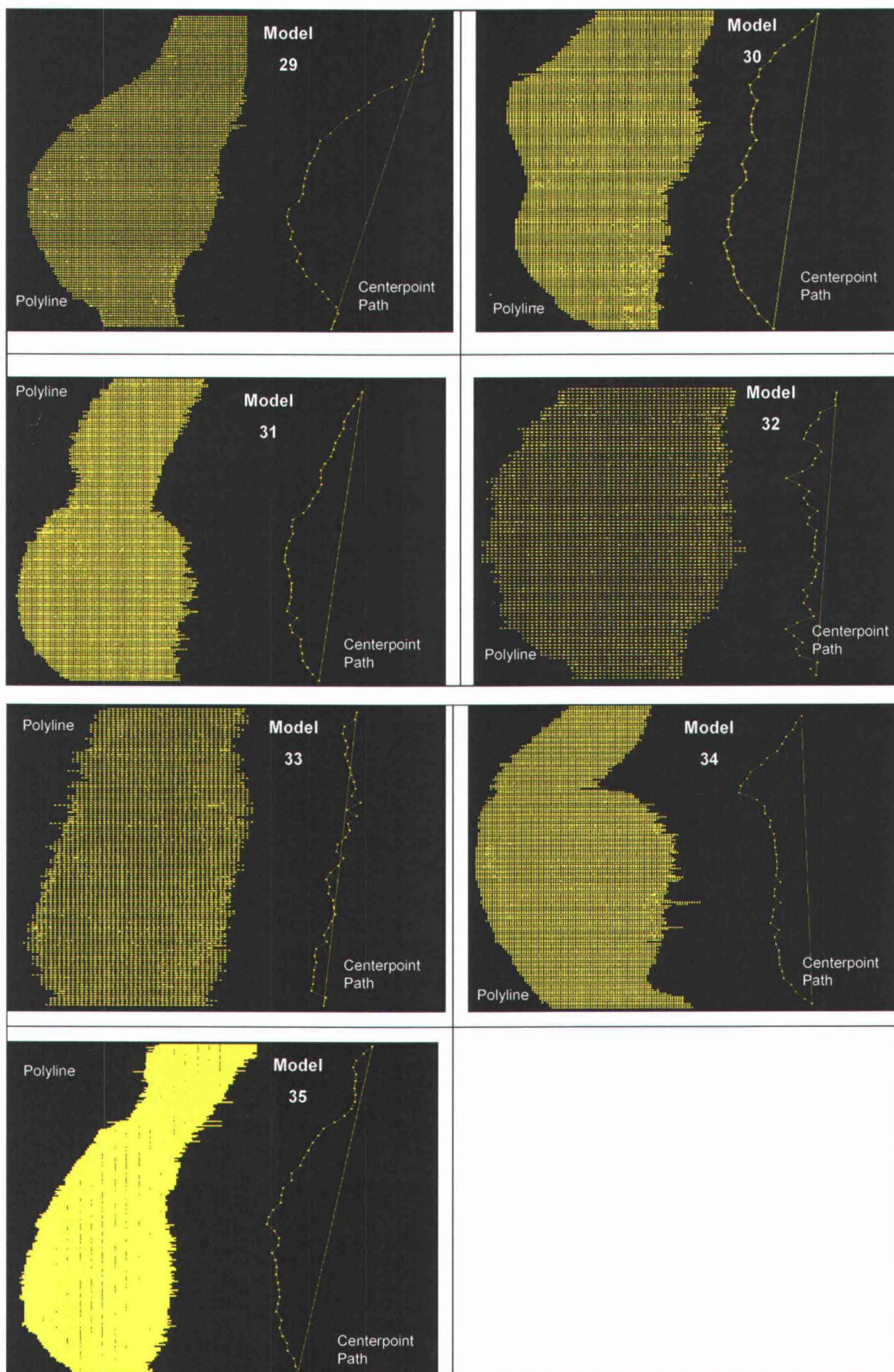
**APPENDIX B: POLYLINE AND CENTERPOINT PATH OF 35
AAA PATIENTS**

Polyline and Centerpoint path of 35 AAA patients



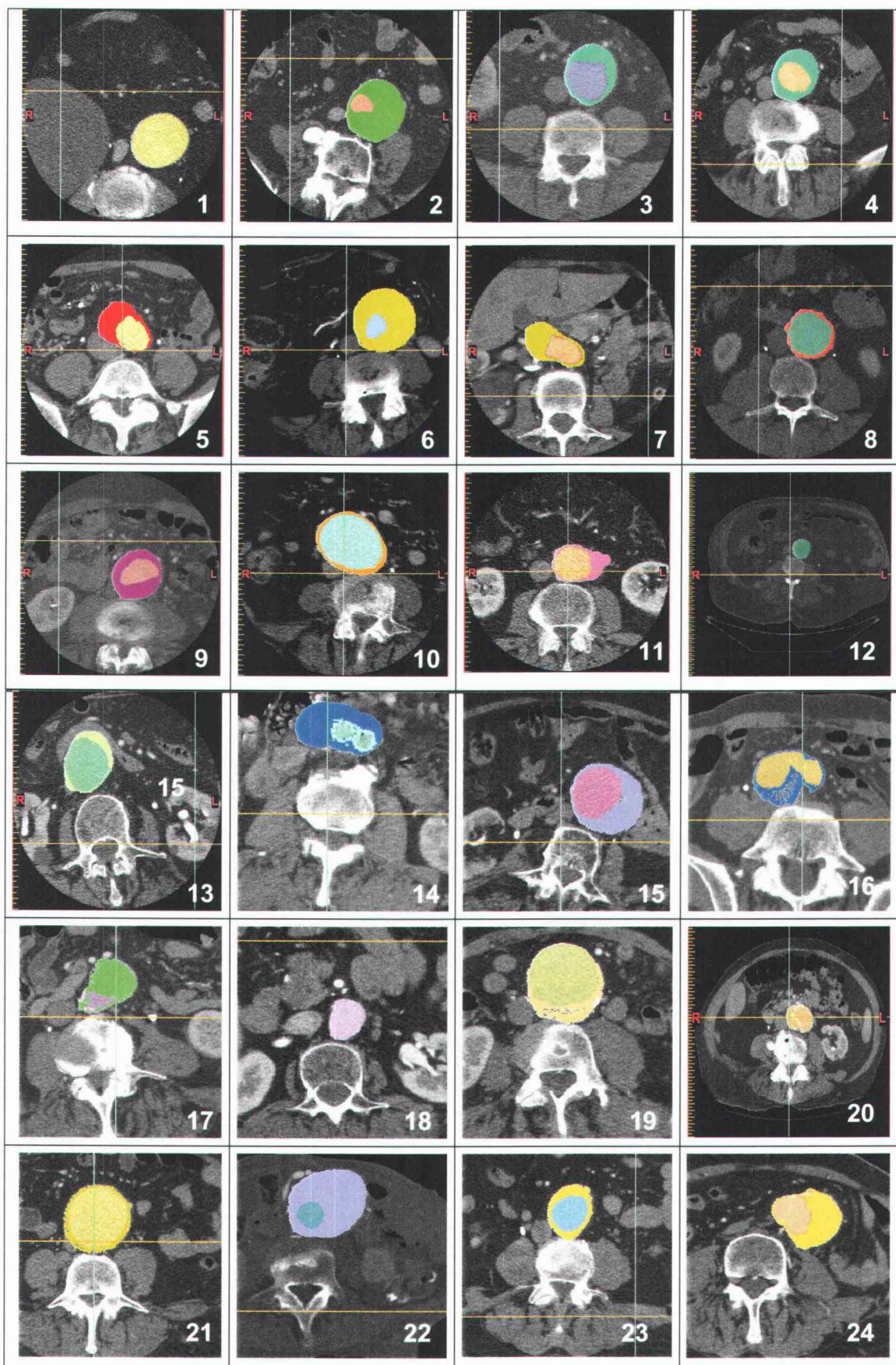


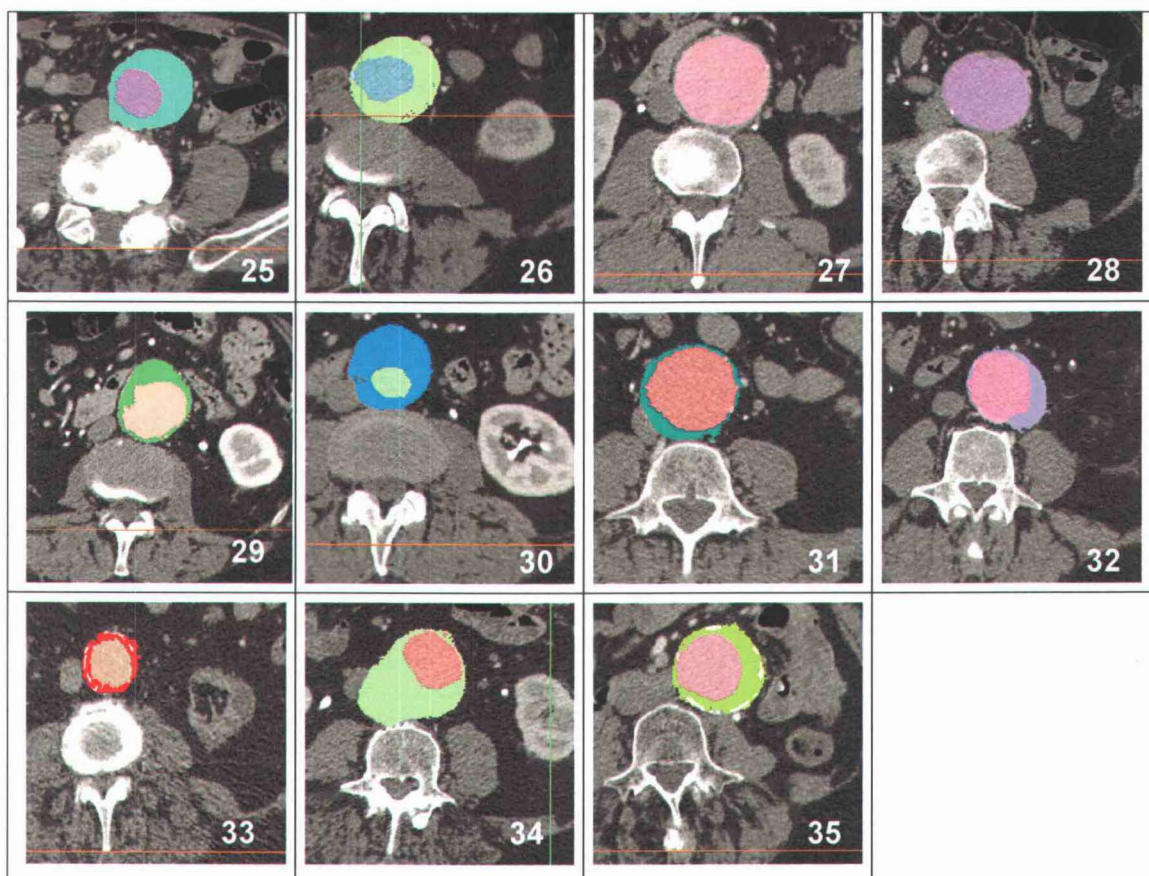




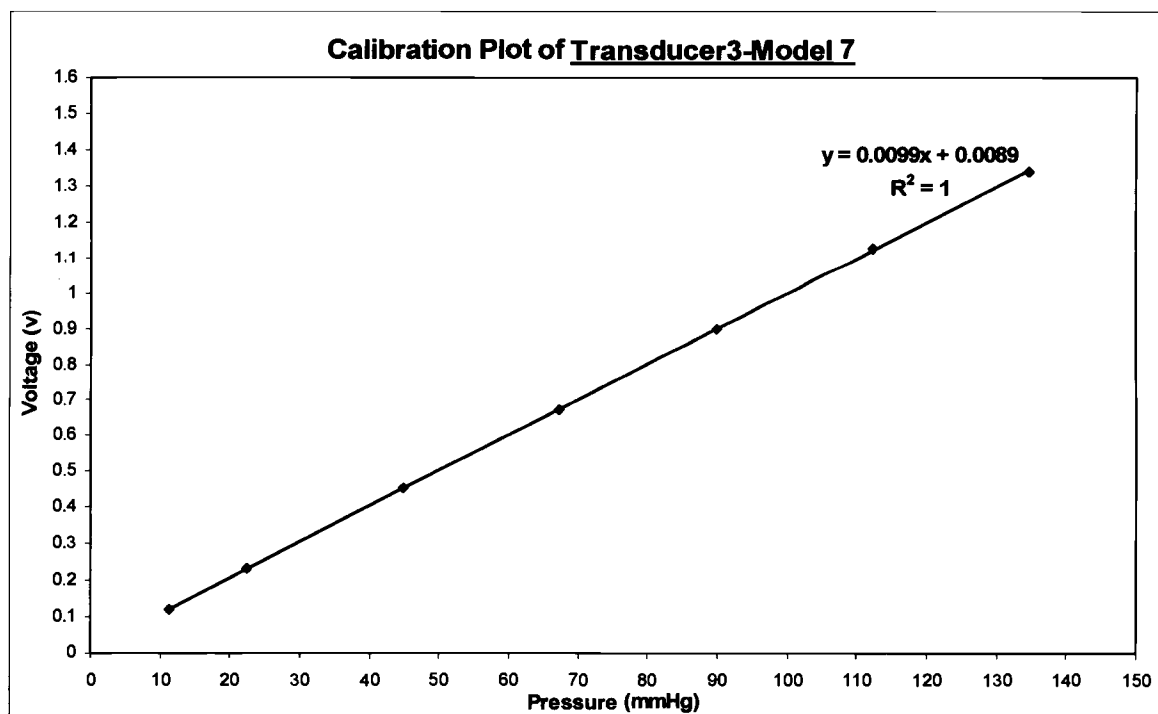
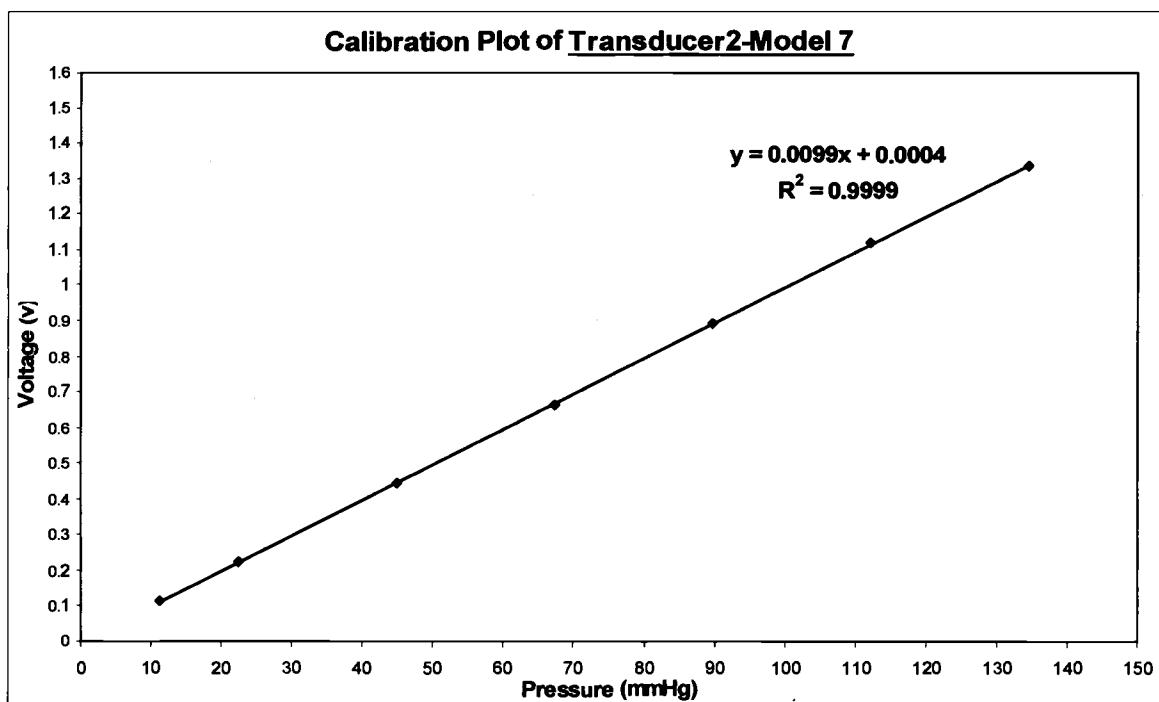
**APPENDIX C: AXIAL CROSS-SECTIONS OF AAA BULGES AT
THEIR MAXIMUM DIAMETER LEVELS**

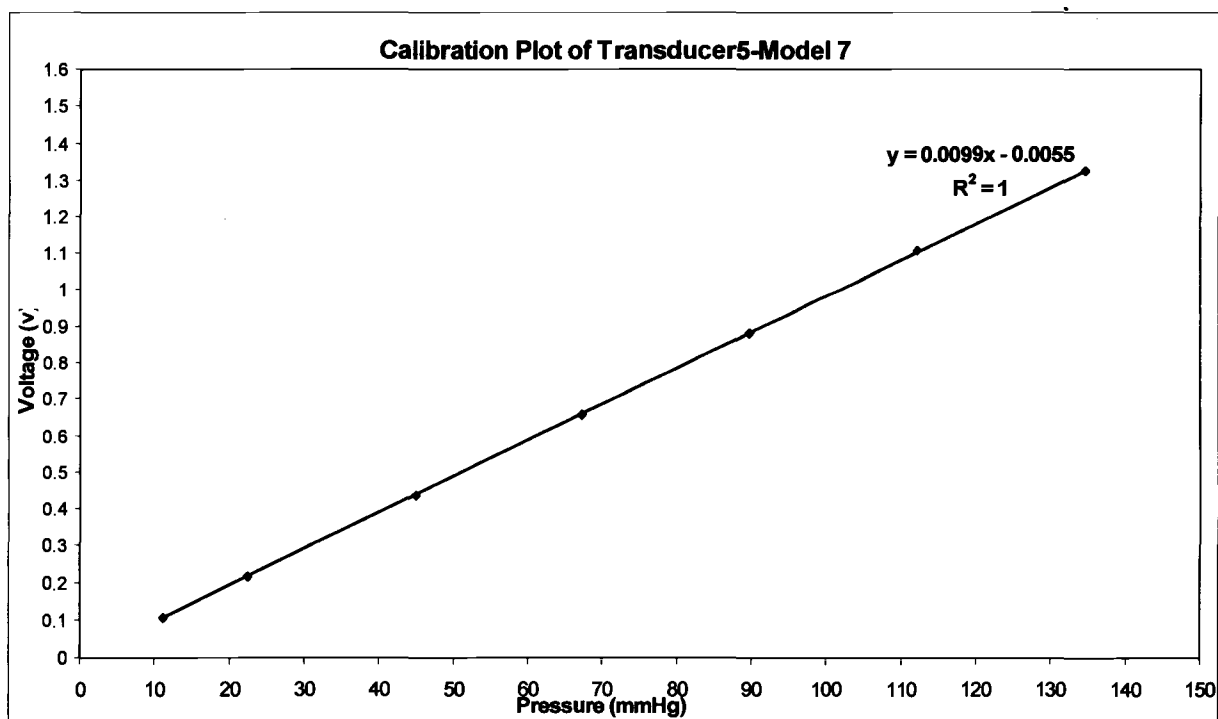
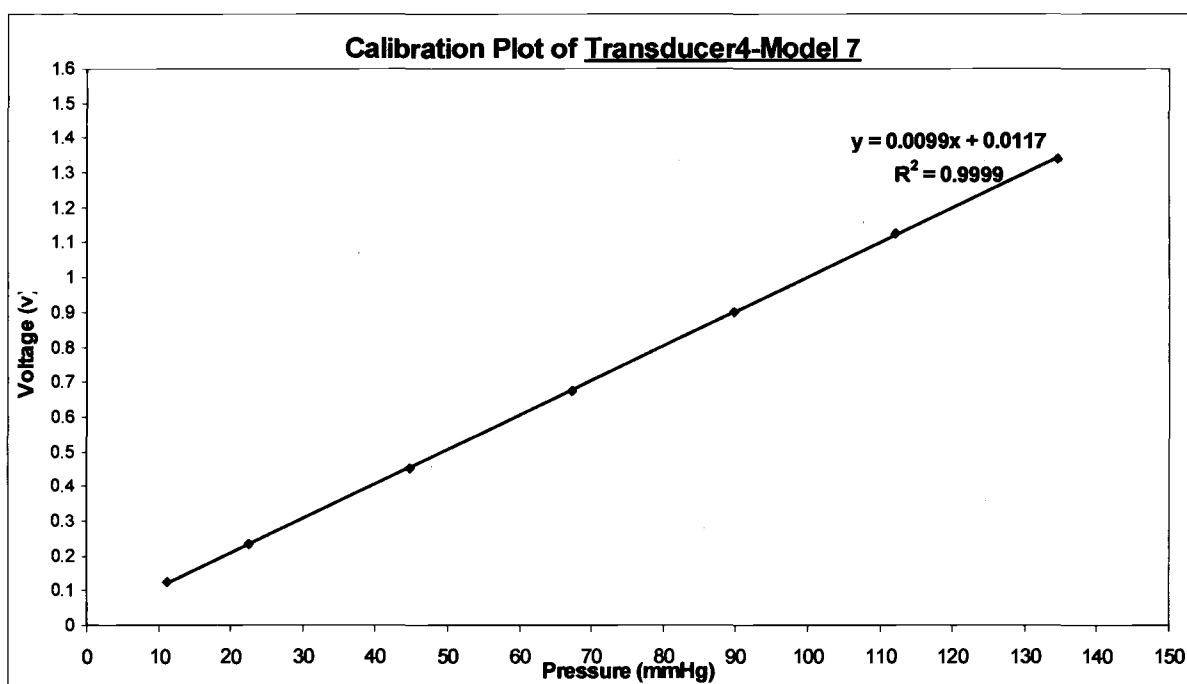
Axial cross-sections of AAA bulges at their maximum diameter levels

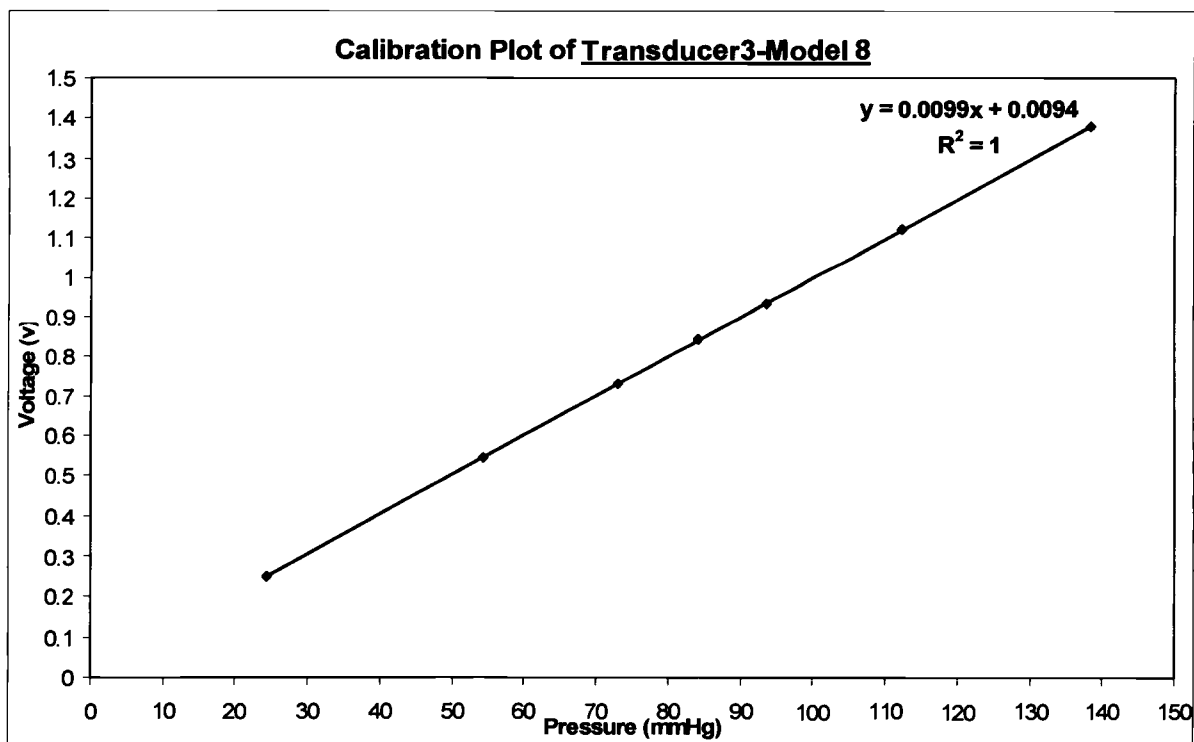
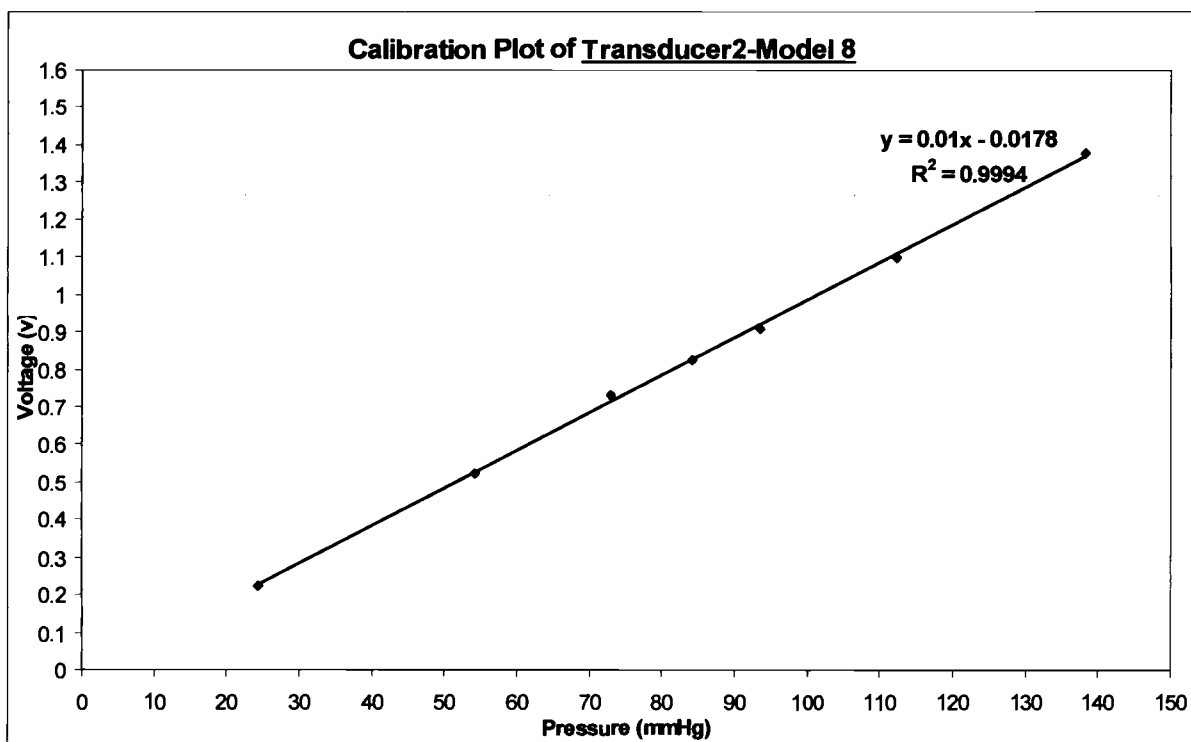


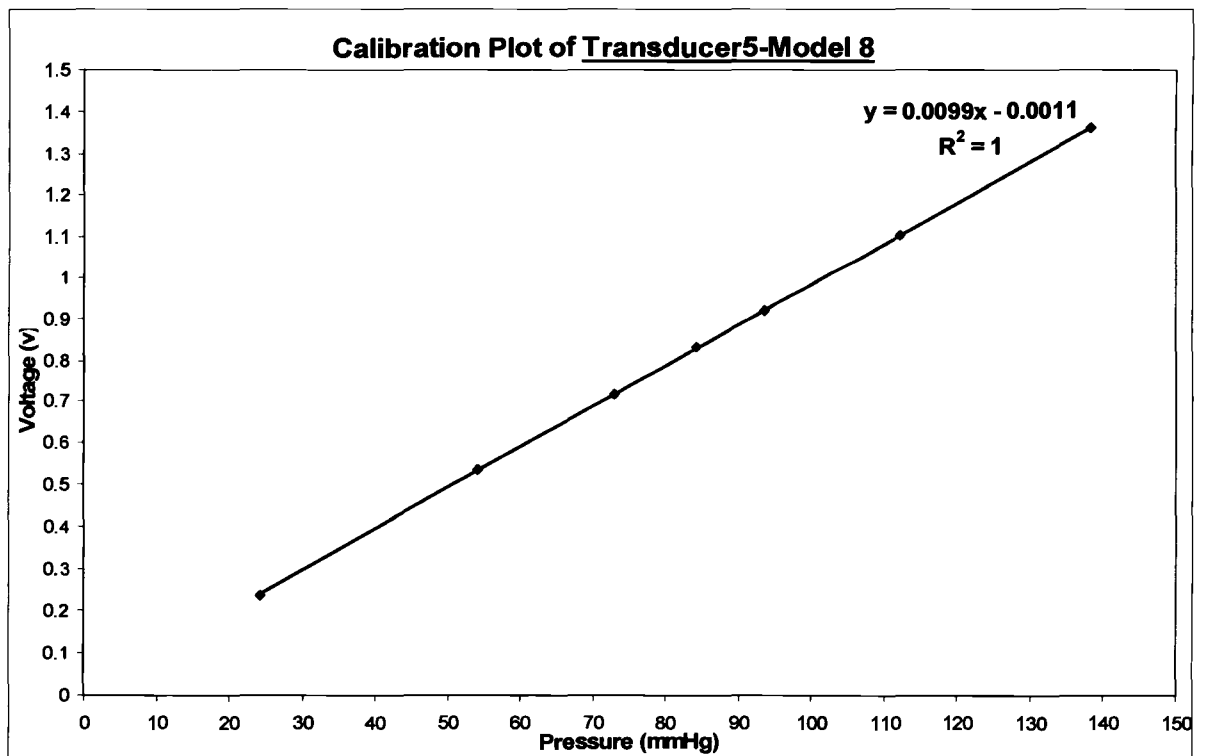
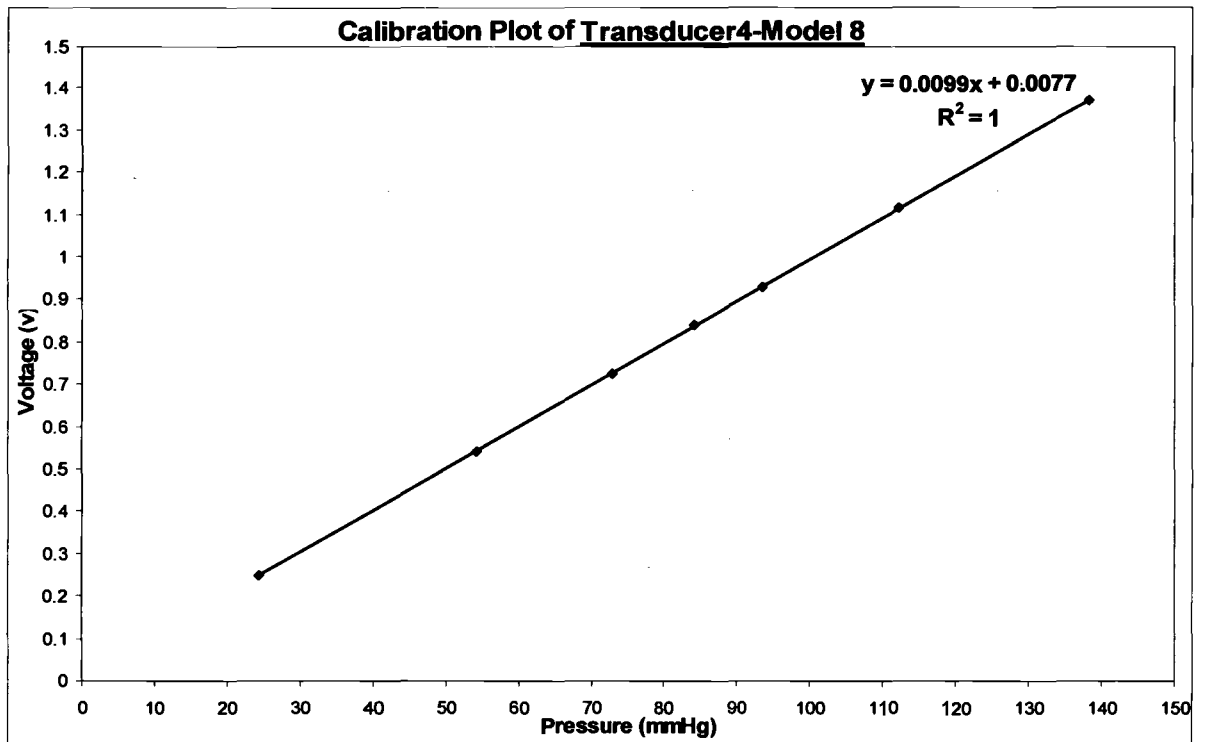


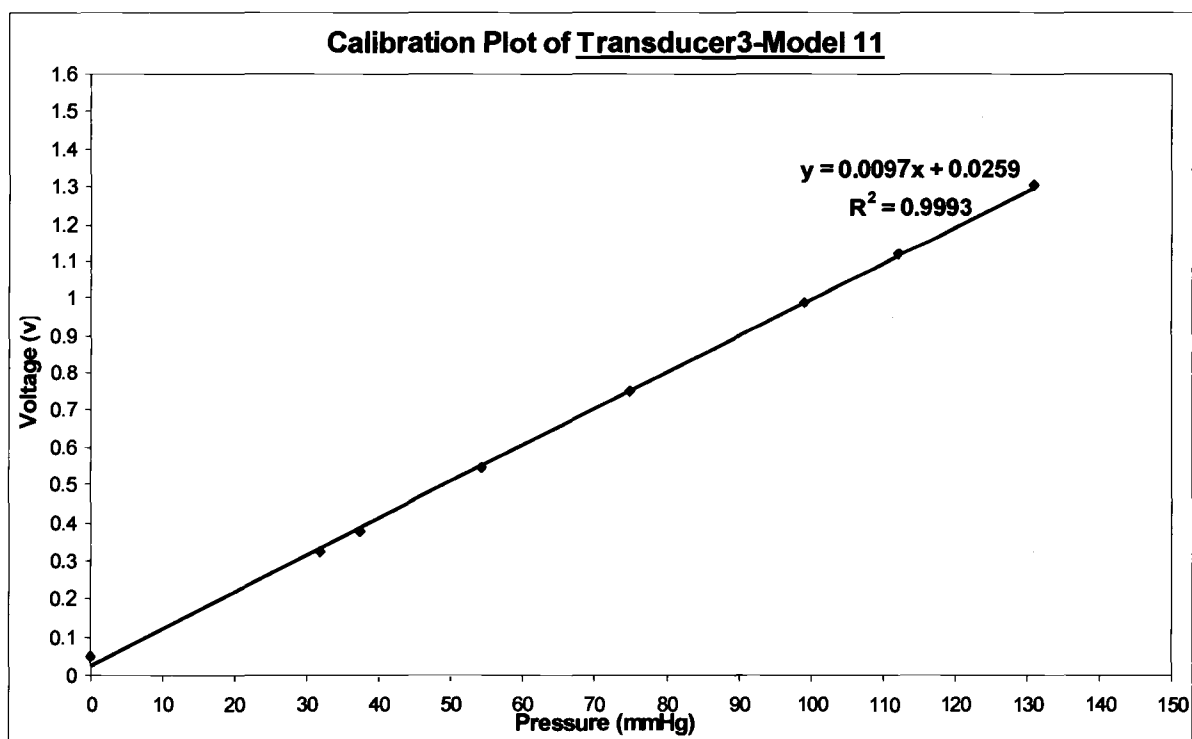
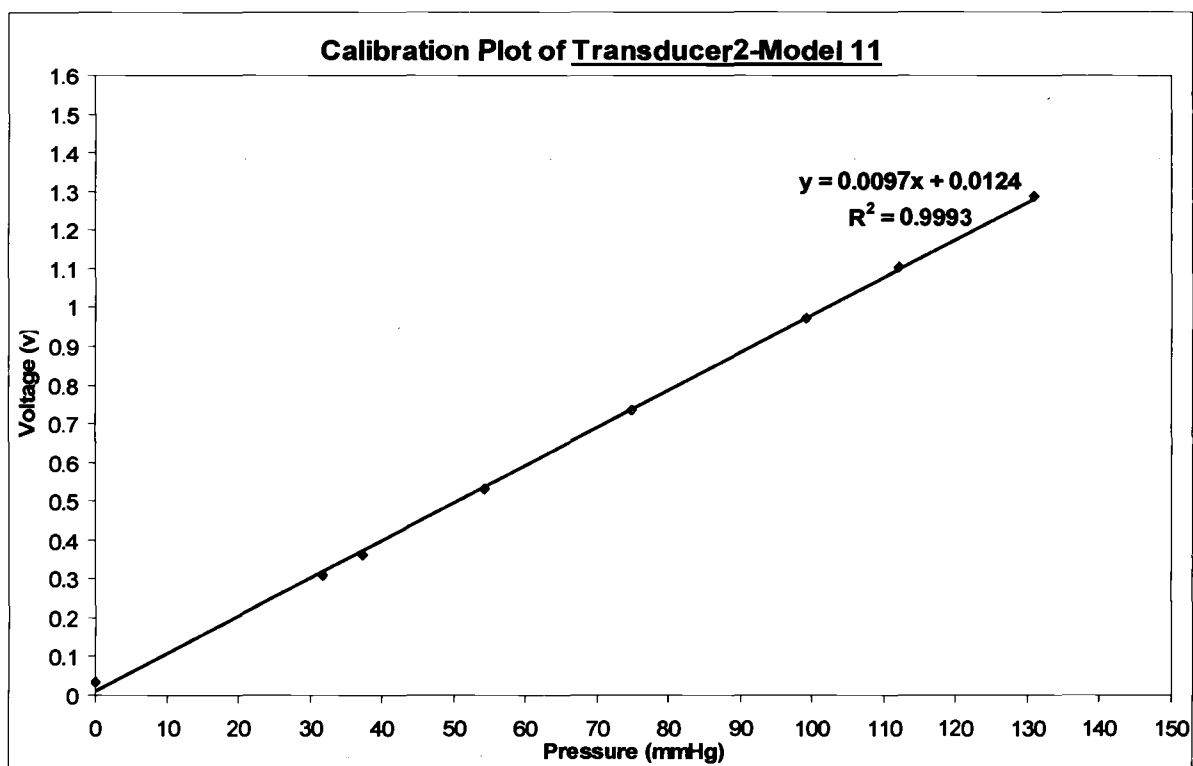
APPENDIX D: CALIBRATION PLOTS

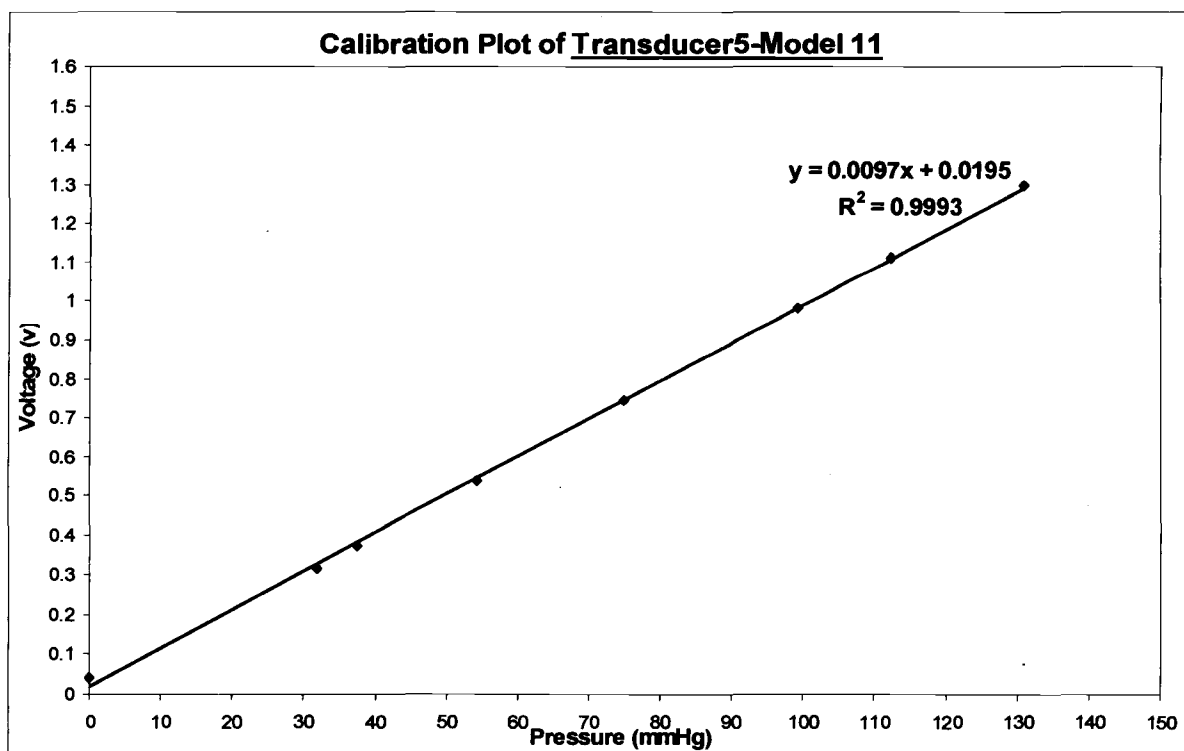
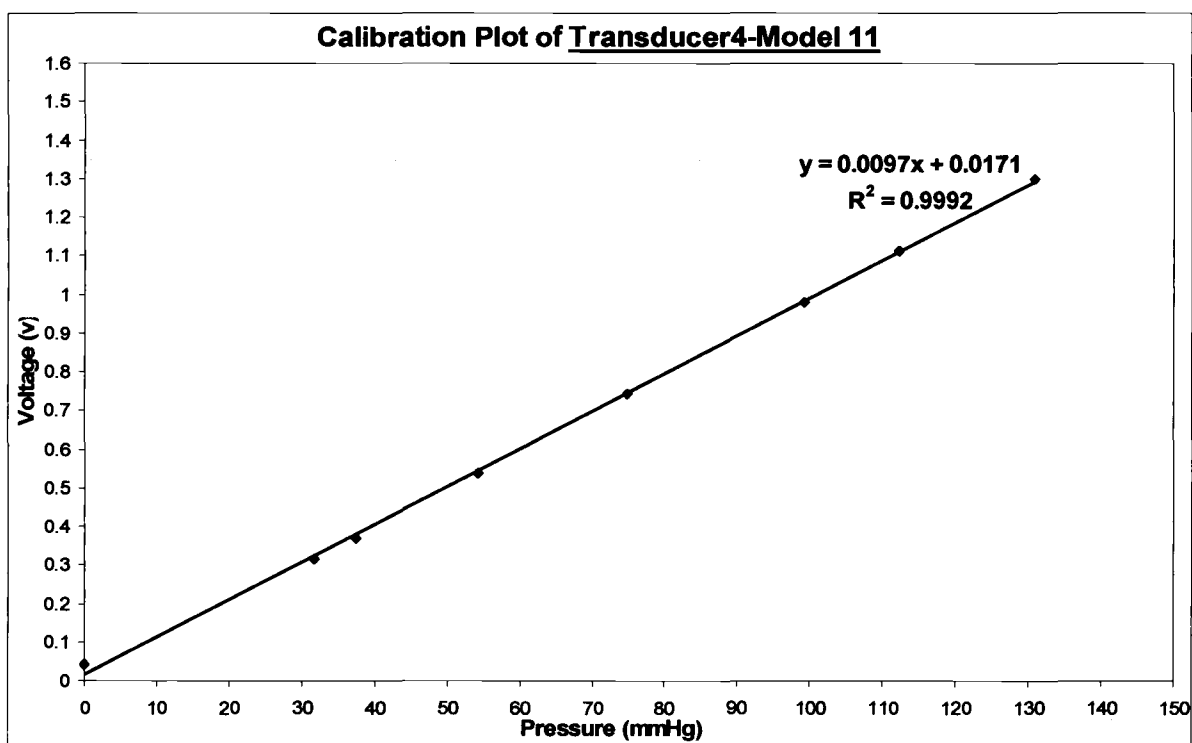












APPENDIX E: TABLES OF INITIAL PRESSURES

Initial Pressures of Model 7

Q (ml/min)	568	1160	1682	2306	2872	3480
<i>Re</i>	<i>500</i>	<i>1000</i>	<i>1500</i>	<i>2000</i>	<i>2500</i>	<i>3000</i>
$P_{1\text{exp}}$ (mmHg)	146.495	146.636	151.788	144.121	136.849	123.369
$P_{2\text{exp}}$ (mmHg)	146.131	146.142	151.455	143.677	136.647	123.879
$P_{3\text{exp}}$ (mmHg)	144.828	146.232	151.222	143.323	136.919	123.755
$P_{4\text{exp}}$ (mmHg)	148.404	146.081	149.445	143.192	136.636	123.228
$P_{5\text{exp}}$ (mmHg)	146.495	146.303	149.384	143.344	136.778	123.425

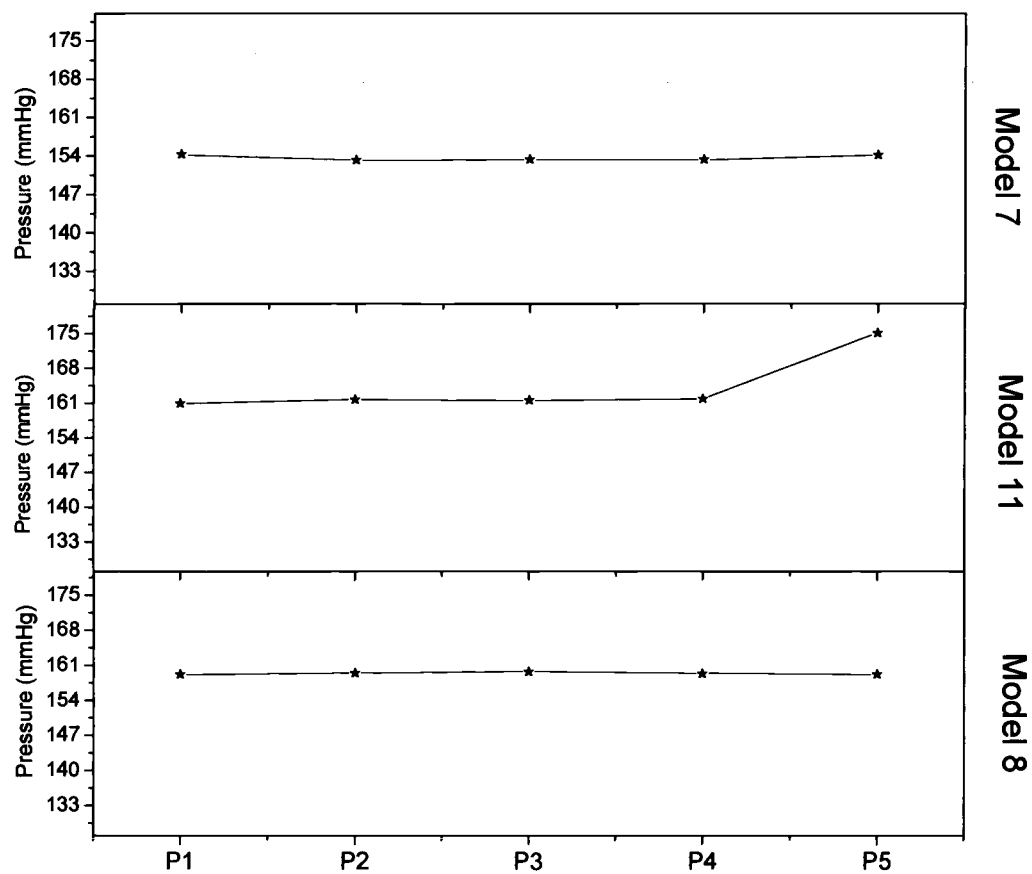
Initial Pressures of Model 8

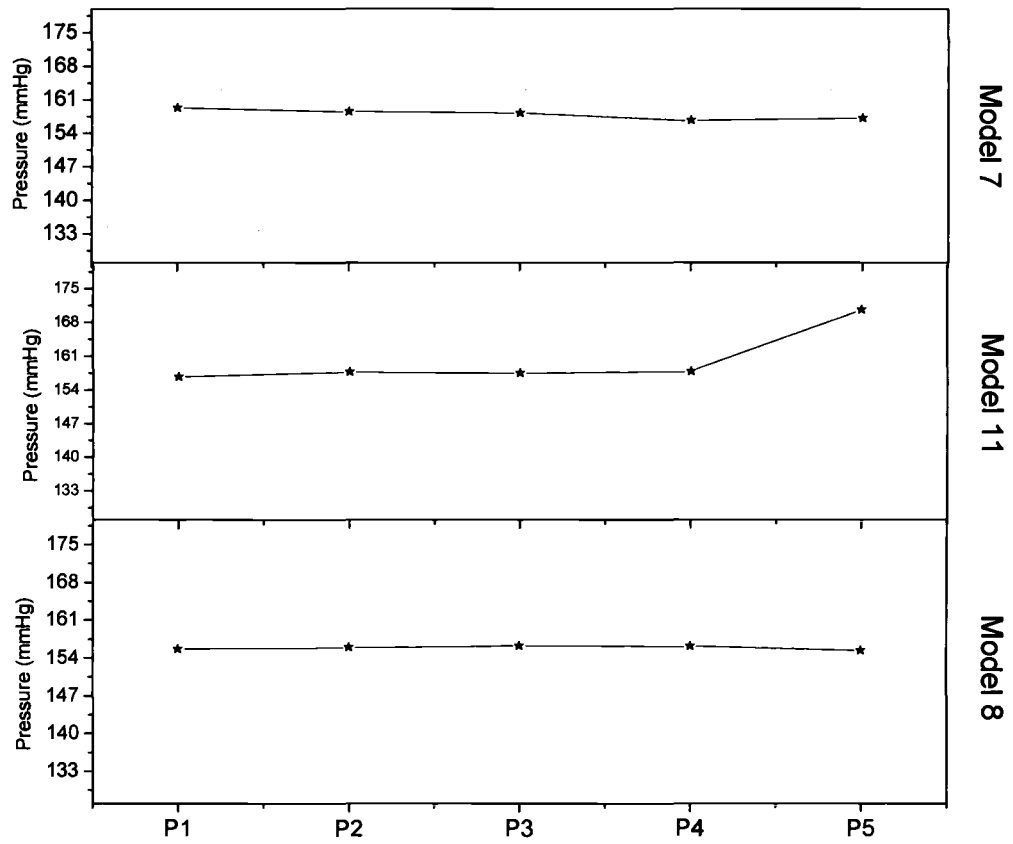
Q (ml/min)	588	1156	1745	2450	2900	3480
<i>Re</i>	<i>500</i>	<i>1000</i>	<i>1500</i>	<i>2000</i>	<i>2500</i>	<i>3000</i>
$P_{1\text{exp}}$ (mmHg)	152.39	151.30	147.76	143.88	136.13	129.65
$P_{2\text{exp}}$ (mmHg)	152.24	151.55	147.96	144.12	136.23	130.053
$P_{3\text{exp}}$ (mmHg)	153.23	152.24	148.79	144.81	135.96	130.09
$P_{4\text{exp}}$ (mmHg)	152.44	151.41	148.07	144.26	136.13	130.15
$P_{5\text{exp}}$ (mmHg)	152.35	151.71	147.90	144.04	136.10	130.33

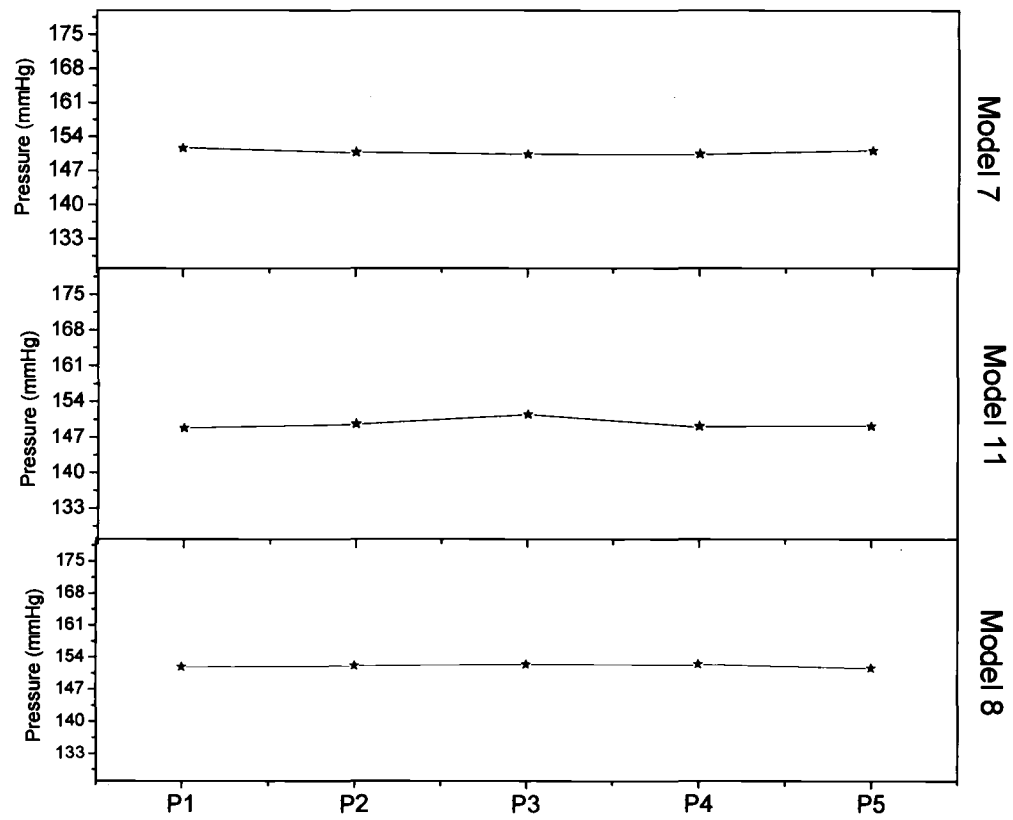
Initial Pressures of Model 11

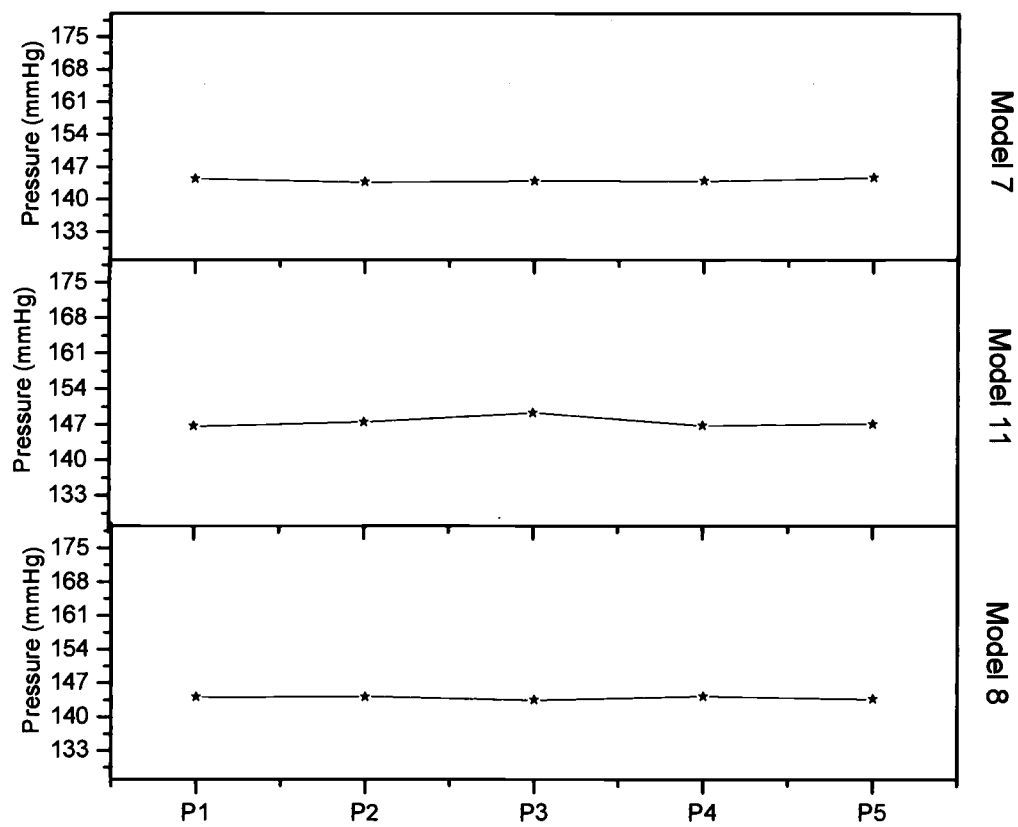
Q (ml/min)	570	1230	1750	2320	2900	3480
<i>Re</i>	<i>500</i>	<i>1000</i>	<i>1500</i>	<i>2000</i>	<i>2500</i>	<i>3000</i>
$P_{1\text{exp}}$ (mmHg)	152.72	152.44	148.35	140.37	138.22	129.68
$P_{2\text{exp}}$ (mmHg)	152.84	152.44	148.47	140.33	138.26	129.61
$P_{3\text{exp}}$ (mmHg)	153.64	153.08	149.11	143.05	140.93	132.16
$P_{4\text{exp}}$ (mmHg)	153.75	153.26	149.24	140.49	138.28	130.20
$P_{5\text{exp}}$ (mmHg)	165.55	166.26	161.69	140.32	138.20	130.41

APPENDIX F: STEADY FLOW ABSOLUTE PRESSURES

Re=1000

Re=1500

Re=2000

Re=2500

Re= 3000